HAL
open science

Précipitations de carbure de vanadium (fibre, interphase) dans des aciers

Meng-Yang Chen

To cite this version:

Meng-Yang Chen. Précipitations de carbure de vanadium (fibre, interphase) dans des aciers. Autre. Université de Grenoble, 2013. Français. NNT : 2013GRENI016 . tel-00956583

HAL Id: tel-00956583

https://theses.hal.science/tel-00956583v1

Submitted on 6 Mar 2014

HAL is a multi-disciplinary open access archive for the deposit and dissemination of scientific research documents, whether they are published or not. The documents may come from teaching and research institutions in France or abroad, or from public or private research centers.

L'archive ouverte pluridisciplinaire **HAL**, est destinée au dépôt et à la diffusion de documents scientifiques de niveau recherche, publiés ou non, émanant des établissements d'enseignement et de recherche français ou étrangers, des laboratoires publics ou privés.

UNIVERSITÉ DE GRENOBLE

THÈSE

Pour obtenir le grade de

DOCTEUR DE L'UNIVERSITÉ DE GRENOBLE

Spécialité : *Matériaux, Mécanique, Génie Civil, Electrochimie*

Arrêté ministériel : 7 août 2006

Et de

L'UNIVERSITÉ NATIONALE DE TAIWAN

Spécialité : Matériaux Sciences et Matériaux Ingénieries

Présentée par

« Meng-Yang / CHEN »

Thèse dirigée par **« Yves/Bréchet »** et
codirigée par **« Mohamed/Gouné »** et **« Jer-Ren/Yang »**

préparée au sein du **Laboratoire Sciences et Ingénierie des Matériaux et Procédés**
dans **l'École Doctorale Ingénierie-Matériaux, Mécanique, Environnement, Energétique, Procédés, Production**
et de **L'UNIVERSITÉ NATIONALE DE TAIWAN**

Etude de la Précipitation Interphase dans le système Fe-V-C : La Microstructure et La Modélisation

Thèse soutenue publiquement le **« 30 Juillet 2013 »**,
devant le jury composé de :

Mr, Alexis, Deschamps
Professur Grenoble-INP, Président
Mr, Yannick, Champion
Directeur de Recherche CNRS, Paris, Rapporteur
Mr, Thierry, Epicier
Directeur de Recherche CNRS, INSA-Lyon, Rapporteur
Mme, Elisabeth, Gautier
Directrice de Recherche CNRS, Nancy, Examinatrice
Mr, Yves, Bréchet
Professeur Grenoble-INP, Directeur de thése
Mr, Jer-Ren, Yang
Professeur NTU-MSE Taiwan, Co-directeur de thése
Mr, Mohamed, Gouné
Professeur ICMCB, invité

Acknowledgement

In 28 August 2011, it was my first time to come to Europe and to start over an unexpected academic life in France. Before that day, studying abroad was an unexpected event in my life. Now, these dreams finally come true and I am about to have my first PhD defense in the end of July 2013. Before leaving the campus, I would like to thank the following people who kindly give me a hand to accomplish the present thesis:

I would like to thank the France Institute in Taipei and the National Taiwan University to provide the scholarship, enabling me to concentrate on my studies in France. Meanwhile, I would like to thank the staff in office of international affairs to help me about the Dual-degree diploma application. I would also thank Professor Yang and his group members to encourage me to make me dream to come true. You guide me to enter the research field of materials science, provide research instruments, and share your research knowledge. These all delight me interests in metallurgy of steel.

I would like to thank the whole members of SIMaP for their assistances to help me to start my European life and for their fruitful discussions. I want to express my appreciations to Marc Verdier in helping me to carry out the experiments of nanoindentation, and Joelle Calabro, Frederic Charlot, and Florence Robaut in CMTC to help me on the SEM and EBSD analysis, respectively. I specially thank Professor Yves Bréchet to kindly welcome me to joint his research group. The model came up with you and Professor Militzer is the core of the present thesis. Finally, I would like to thank Professor Mohamed Gouné for his collaborations and efforts in the present

thesis. The modeling of interphase precipitation becomes valuable with your helps and supervisions.

I would like to thank my friends in France and in Taiwan. With your supports and accompanies, I do not feel along in my Ph.D. career. Finally, I would like to devote the whole thesis to my families. You give me everything and thank you to let me have the chance to explore this world.

Contents

Acknowledgement I

Contents III

List of Figures VIII

List of Tables XVII

Chaptier 0 1

Résumé 1

0.1 Introduction 1

0.2 Etude expérimentale de l'évolution morphologique des carbures lors de la transformation austénite/ferrite : précipitation interphase et fibreuse 3

0.3 Modélisation de la précipitation interphase 5

0.4 Lien entre la microstructure et les propriétés mécanique 7

Abstract 10

Chapter 1 12

General Introduction 12

Chapter 2 16

Literature Review 16

2.1 Precipitation in ferritic matrix 16

2.2 Precipitation in pearlitic ferrite 28

2.3 Models for interphase precipitation in vanadium alloyed steels 30

2.3.1 The models for interphase precipitation 33

2.3.2 The Superledge on the ferrite/austenite interface 59

2.3.3 The models for fibrous carbide 61

2.4 The mechanical properties of microalloyed steels 64

2.4.1 The strength of ferrite 64

2.4.2 Precipitation hardening in alloyed steels 66

2.4.3 The Orowan and Ashby-Orowan equations 68

2.5 Summary of the chapter 72

Chapter 3 73

Experimental investigations of the as-received materials 73

3.1 Introduction 73

3.2 Experimental Procedures 74

3.3 The Microstructure 75

a. Optical Microscopy 75

b. Mechanical properties 75

c. Transmission Electron Microscopy (TEM) 77

3.4 Quantitative estimations of the strengthening contributions 80

3.5 The occurrence of fibrous carbide in Steel-C 83

3.6 Conclusions 83

Chapter 4 85

The TEM investigations of the features of the interphase-precipitated carbide and the fibrous carbide 85

4.1 Introduction 85

4.2 Experimental Procedure 85

4.3 Results and discussions 86

a. Macrostructure and Vickers Microhardness 86

b. Precipitation in ferrite 87

c. Precipitation in pearlitic ferrite 91

4.4 The conditions for the development of fibrous carbide 94

a. Effects of the transformation temperature 94

b. The effect of interface coherency.....95

c. The alloying elements 96

4.5 Conclusion 98

Chapter 5 99

The superledge model for interphase precipitation.....99

5.1 Introduction.....99

5.2 The derivations.....100

a. Assumptions 100

b. The classical ledge mechanism of austenite-to-ferrite transformation ..102

c. The interaction of carbide with the growing ferrite phase 104

5.3 Parameters used for calculations.....114

5.3.1 The ferrite and carbide nucleation rates.....114

5.3.2 The diffusion mechanism of solute atom.....115

5.3.3 The interface mobility, *M*.....116

5.4 Applications of the model and discussions 117

5.4.1 Prediction of the sheet spacing 118

5.4.2 Prediction of the particle spacing and the interface velocity 119

5.4.3 The effects of C and V contents on sheet spacing of IP.....121

5.5 Conclusion 122

Chapter 6 127

The Feature evolutions of interphase precipitation with the progression of austenite-to-ferrite transformation 127

6.1 Introduction.....127

6.2 Experiments 128

6.3 Modeling.....129

a. Summary of the superledge model for interphase precipitation 129

b. The mass balance of carbon and solute 131
6.4 Results 135
a. Microstructures of the interphase-precipitated carbide and the fibrous carbide 135
b. Modeling results 137
6.6 Discussions 138
a. The effect of carbide precipitation on the overall interface velocity 138
b. The minimum sheet spacing of interphase precipitation at a given transformation temperature 144
6.7 Conclusions 145
Chapter 7 147
The effect of the interphase-precipitated carbide on the strengthening contribution to ferrite 147
7.1 Introduction and context of the study 147
7.2 The conversion of the depth-penetrating curve into mechanical properties 151
7.2.1 Bucaille's approach 151
7.2.2 The reliability of the processed data 155
7.3 Methodology: Measurement of the Orowan contribution of interphase precipitation 156
7.3.1. Orowan contribution 156
7.3.2. Determination of $\Delta\sigma_y$ and main results 159
7.4 Prediction of the Orowan contribution of ferrite strengthened by the interphase-precipitated carbides for different heating paths 162
7.4.1 Calculation of the Orowan contribution 163
7.4.2 Comparison between the calculated Orowan contribution and the measured one by nanoindentation 166

7.5 Discussion 168
7.5.1 The complex influence of heat treatment temperatures 168
7.5.2 The optimization of arrangement of the interphase-precipitated carbides under a fixed carbide volume fraction condition 170
7.5.3 Effects of Carbide distribution on Orowan strengthening: Comparison of the contribution of the random array carbides with the interphase-precipitated carbides 172
7.6 Conclusions 176
Chapter 8 178
General Conclusions and Perspectives 178
References 182

List of Figures

Figure 0-1 microstructure typique de précipitation interphase. On peut voir l'alignement typique des carbures 1

Figure 0-2 Précipitation de carbures fibreux obtenue lors d'un refroidissement lent.... 3

Figure 0-3 Séquences de précipitation lors de l'avancée de l'interface austénite/ferrite 4

Figure 0-4 Une micrographie MET pris sur la région contenant la transition de précipitation interphase à la fibre de carbure, avec l'analyse de l'orientation crystallograhie 5

Figure 0-5 Shema des différentes étapes du modéle superledge 6

Figure 0-6 Evolution en fonction de la température des paramètres de la précipitation interphase. Comparaison entre les résultats du modèle. 7

Figure 0-7 Les comportements élasto-plastique de ferrite calculé par les résultats de nanoindentation, et l'effet de taille de grain grain de ferrite est pris en compte 8

Figure 0-8 Les compositions de la thése 9

Figure 2-1 The variations of carbide morphology with transformation temperatures [28] 17

Figure 2-2 Schematic diagram showing the interphase-precipitated carbides with planar spacing 17

Figure 2-3 The carbon concentration profile ahead of ferrite/austenite interface during interphase precipitation process [29] 18

Figure 2-4. Schematic illustration showing a unit ledge accompanying with features of interests. The meanings of each term are referred to the text. 19

Figure 2-5 The bowing mechanism for the curved interphase-precipitated carbides

with irregular spacing [34] 20

Figure 2-6 Schematic illustration of quasi-ledge mechanism of curved interphase precipitated carbides with regular spacing [34] 20

Figure 2-7 Fe-5Cr-0.2C (wt%) isothermal transformation at 650 ^{o}C for 30 min showing the interfaces associated with interphase precipitation (Right-hand side) and alloy fibers (Lef-hand side) [45] 25

Figure 2-8 Mo_2C carbides with different morphologies in Fe-3.5Mo-0.22C (wt%) steels after isothermal transformation at 750 ^{o}C for 30 min. (a) interphase precipitation, (b) Widmanstätten arrays, and (c) Mo_2C fibers [46] 27

Figure 2-9 Fe-4Mo-0.2C (wt%) steels showing the spacing and fineness of fibers changed as transformation temperature was varied from 850 ^{o}C (left-hand side) to 750 ^{o}C (right-hand side) [43] 28

Figure 2-10 Proposed ledge mechanism illustrating interphase precipitation in pearlitic ferrite [52] 29

Figure 2-11 The observed fibrous carbides in pearlitic ferrite, a dark-filed image [5] 29

Figure 2-12 The observed growth ledge on the pearlite/austenite interface [48] 30

Figure 2-13 Schematic illustration showing the sequences of interphase precipitation in the L-T model. (a) the first row of precipitates nucleate with a size of y_p and generates the pseudo-phase boundary simultaneously; (b) the pseudo-phase boundary advances to the position where has sufficient solutes for further precipitation; the growth of the carbides in the first row is taken into considerations as well; and (c) carbides continue to grow, from the size $y_p^{'}$ to $y_p^{''}$ [12] 34

Figure 2-14 Schematic illustration showing the Rios' model. The pseudo-phase is indicated as a shaded area. In the vanadium diffusion region, the pseudo-phase boundary changes linearly from the previous ledge riser to the latter one, with a final

thickness, s_f. 38

Figure 2-15 Schematic illustration showing the model proposed by Liu. The important time parameters are indicated in this figure. In his model, the process of interphase precipitation is a repeated force balance between the driving force, F_d, and the pinning force, F_p [57] 44

Figure 2-16 Interphase precipitation on a semi-coherent interface in L-Z model. (a) a ledge developed on the interface; (b) the ledge expands laterally and gradually increases its height; and (c) another precipitation process occurs on the interface again as the ledge reaching a critical height. The corresponding concentration profile is presented. [13].....55

Figure 2-17 The developments of interphase precipitation on an incoherent interface in L-Z model, the front of interface is curved for this case. (a, b) a ledge developed on the interface then grows laterally and increases its height, generating the flow of solutes from the top to the previous row of precipitation (c) primary precipitation occurs on the top of ledge (the superledge); (d) the superledge continues to expand laterally, leading additional precipitation to form at the middle of superledge boundary; and (e) the diffusion of solute atoms along incoherent interphase boundary leads to further precipitation (secondary precipitation). [13].....58

Figure 2-18 Schematic illustrations showing (a) the developing of a unit ledge on allotriomorphic ferrite by diffusional transformation, and (b) geometric analysis of superledge development. [56].....60

Figure 2-19 Model illustrating the Mo2C carbides formed in spiky noduls. Fe-4.10Mo-0.23C (wt%) isothermal transformation at 650 oC for 2 hours [46] 62

Figure 2-20 A comparison (a) interphase precipitation, and (b) fiber growth. [3].....62

Figure 2-21 A model describing the fiber precipitation in association with migrating austenite/ferrite interface [12].....63

Figure 2-22 Another model concerning the crystallographic basis. The carbide morphologies are controlled by θ_1 and θ_2, where θ_1 is the angle between slowest moving austenite/ferrite interface and grain boundary, and θ_2 is the angle between slowest moving austenite/ferrite and austenite/carbide interfaces [61] 63
Figure 2-23 Schematic illustration showing Orowan bypass mechanism of dislocation through carbide. (a) a dislocation is going to pass by a particle in matrix; (b) the dislocation is bowed because of the resistance force exerting from the particle, and (c) the dislocation passed by the particle and left a dislocation loop around the particle .67
Figure 2- 24 Schematically illustration showing the regular square array of particles and their interaction with a dislocation proposed in Orowan model. 70

Figure 3-1 The optical metallography of (a) CB, and (b) UHSB showing that both of them are consisted of ferrite and pearlite but the microstructure of UHSB is greatly refined [75]. The white phase is ferrite and the dark phase is pearlite. 74
Figure 3-2 Optical micrographs of UHSSBs revealing microstructures composed of ferrite and pearlite: (a)Steel-A; (b) Steel-B. 75
Figure 3-3 (a) Stress-Strain Curves of Steel-A and Steel-B, demonstrating apparent yield point and yield plateaus, and (b) local magnification at yield point. 76
Figure 3-4 The TEM micrographs showing typical inter-phase precipitated carbides in ferrite: (a) Steel-A; (b) Steel-B. Fig. 2(a) clearly showing that dislocations were pinned by these carbides. 77
Figure 3-5 Bright-field and dark-field images and corresponding diffraction patterns of carbides. (a) Bright-field image; (b) Dark-field image illuminated by 002 carbide reflection; (c) Corresponding diffraction; (d) Identified orientation relationship of carbides and ferritic matrix. 78
Figure 3-6 EDX analysis on nano-sized carbides demonstrating that were composed

of niobium and vanadium. 79

Figure 3-7 The fine inter-lamellar spacing of pearlite in UHSSBs: (a) Steel-A; (b) Steel-B. It shows that the spacing is about 100 nm. 79

Figure 3-8 Representative TEM micrographs for the dislocation structures in ferrite matrix and corresponding two-beam conditions: (a) Steel-A; (b) Steel-B. 81

Figure 3-9 The VC fibers in Steel-C 83

Figure 4-1 The optical micrograph of the microstructure of the sample austenitized at 1200 ^{o}C subsequently isothermally transformed at 650 ^{o}C for 1h.....86

Figure 4-2 TEM analysis on the area containing two carbide aggregates in ferritic matrix. (a) a bright-field image. (b) the SADP, (c) the indexed SADP of the interphase-precipitated carbide, (d) the indexed SADP of the carbide fiber, (e) and (f) the dark-field image illuminated by carbide 002 reflection for the interphase-precipitated carbide and carbide fiber, respectively. 88

Figure 4-3 Transition of carbide aggregates (interphase precipitation, carbide fiber, and pearlite) during the austenite-to-ferrite transformation.....91

Figure 4-4 The observed interphase-precipitated carbide and carbide fiber in pearlitic ferrite. (a-c) the bright-field, dark-field images and associated SADP of the interphase-precipitaed carbide; (d-f) that for carbide fiber. 92

Figure 4-5 The HRTEM image of the carbide fiber in ferrite. (a) the lattice image, (b) the FFT diffractogram, and (c) the EDS analysis of carbide fiber. 94

Figure 4-6 (a) The selected area for EBSD analysis showing ferrite allotriomorphs, idiomorphs, and martensite; (b) Orientation map of the selected area; (c) a stereographic projection showing the martensite variants transformed from this prior austenite grain, and (d) coupling with measured martensite (M1) and ferrite (a1) orientations.....97

Figure 4-7 (a) A micrograph showing the calculated deviation angle of ferrite grains; the ferrite with carbide fiber is labeled, (b) a SEM image of the labeled ferrite grain, and (c) a larger magnification of (b). 97

Figure 5-1 The characteristic features of interphase precipitation focused in the present superledge model.....101

Figure 5-2 The proposed sequence of the development of a superledge originated from the ferrite/austenite interface. (a) a unit ledge forms on an interface with carbides; (b) the first ledge moves laterally and is pinned by carbides, and then another unit ledge nucleates on the top of it; (c-d) the ledge continues to increase its height to unpin from carbides; (e) the superledge is able to move laterally again and then merge the neighboring superledges, and (f) the overall interface advances until carbides precipitate on the interface again, completing a cycle of interphase precipitation. ...103

Figure 5-3 Coupling with experimental data to the calculated sheet spacing showing that good agreements with the sheet spacing measured at lower transformation temperatures (< 700 ^{o}C). The experimental data is cited from Wilyman [92], Parson [52], and Miyamoto [74].....118

Figure 5-4 The calculated particle spacing. The composition studied by Parsons and Edmonds [52] has been used (0.5 wt%C, 0.82wt%Mn, 0.3wt%V, 0.026wt%) 120

Figure 5-5 The calculated interface velocity from superledge model and ledge velocity; The composition studied by Parsons and Edmonds [52] has been used (0.5 wt%C, 0.82wt%Mn, 0.3wt%V, 0.026wt%).....120

Figure 5-6 The calculated sheet spacing changing with C and V contents.....122

Figure 6-1 The optical micrographs taken from samples isothermally transformed at (a) 670 ^{o}C; (b) 650 ^{o}C, and (c) 630 ^{o}C for 1h. 128

Figure 6-2 Schematically illustrations showing the decreasing in (a) α nucleation energy, and (b) transformation driving force for transformation with the progressive of γ→α transformation 131

Figure 6-3 Schematic illustrations showing the proposed sequence of interphase precipitation accompanied with composition changes. (a) initial structure consisted of austenite only; (b) ferrite grows into austenite without carbide precipitation; (c) the first row of carbides forms on the ferrite/austenite interface; (d) ferrite advances again in a distance of sheet spacing of interphase precipitation; (e) The second row of carbides forms, and (f) continuously ferrite and carbide alternatively grows and precipitates, respectively. 134

Figure 6-4 The flow chart of iteration procedures 135

Figure 6-5 TEM micrographs of interphase precipitation and corresponding HRTEM lattice images taken on the samples transformed isothermally at: (a, d) 630 ^{o}C, (b, e) 650 ^{o}C, and (c, f) 670 ^{o}C. 136

Figure 6-6 The TEM micrographs of typical carbide fiber microstructure isothermally transformed at (a) 630 ^{o}C, (b) 650 ^{o}C, and (c) 670 ^{o}C 136

Figure 6-7 The calculated evolutions of (a) particle spacing and (b) sheet spacing with time at different transformation temperatures, showing that the sheet spacing becomes finer but particle spacing exhibit an opposite tendency as transformation proceeds. 138

Figure 6-8 (a) the calculated evolutions of overall interface velocity with time, and (b) the calculated evolution of ferrite thickening isothermally at 650 ^{o}C showing a good agreement with experimental data. 139

Figure 6-9 The ratio of $\upsilon_{\alpha\gamma}/\upsilon_{\circ}$ at different transformation temperatures with the progressive of austenite-to-ferrite transformation of the steel studied 139

Figure 6-10 The proposed model for the formation of carbide fiber. (a) a unit ledge is

pinned by carbides; (b) the growth of carbide exceeds that of ferrite, growing along the side of ledge, and (c) the ledge never unpins from pinning carbides, resulting in carbide fibers. 142

Figure 6-11 A comparison of measured particle spacing of different carbide aggregates measured at the samples isothermally transformed at 650 ^{o}C for 1h. The particle spacing of interphase precipitation and carbide fiber show distinctive two groups, indicating that the carbide fiber develops at the later stage of austenite-to-ferrite transformation. 143

Figure 6-12 TEM micrograph showing the transition of interphase precipitation to fibrous carbide; the previous ledged interface can be well-illustrated. 143

Figure 6-13 The boundary of the predicted sheet spacing coupled with experimental data (the solid points) measured at different transformation temperatures 145

Figure 7-1 A schematically illustration showing the main quantities presented in the depth-penetrating curve 149

Figure 7-2 The ideal condition of the deformation and recovery of specimen during the indentation test. 150

Figure 7-3 The illustration of sink-in and pile-up phenomena showing on the surface of specimen during indentation. 156

Figure 7-4 The microstructure of the as-received hot-drawn steel bar and the representative stress obtained by nano-indentation by using two different indenters. 160

Figure 7-5 The heat treatments of the specimens 163

Figure 7-6 The obtained typical depth-penetrating curves of the steel studied by using (a) Berkovich indenter, and (b) Cubic-Corner indenter. 163

Figure 7-7 Schematic illustration of the geometric orientation of the sheet plane,

carbide platelet, and the slip plane. 165

Figure 7-8 The calculated stress-strain curve for ferrite transformed at (a) 630 ^{o}C, (b) 650 ^{o}C, and (c) 670 ^{o}C; the strengthening contributions to the global strength of ferrite are indicated 167

Figure 7-9 The temperature-dependence of (a) sheet spacing, (b) carbide radius, (c) carbide volume fraction, and (d) theoretical Orowan strengthening with transformation temperatures. 169

Figure 7-10 The evolution of Orowan strengthening with the sheet spacing and carbide radius. The carbide volume fraction is given as 0.0067. 172

Figure 7-11 The variation of the ratio of Orowan strengthening for interphase-precipitated carbide to that for random array carbide with carbide radius. (a-c) the particle spacing is fixed, and (d-f) the sheet spacing is fixed. 175

Figure 7-12 The ratio varying with the carbide volume fraction, f_v and a normalized precipitate state parameter, λ/R. (a-c) the particle spacing is fixed, and (e-f) the sheet spacing is fixed. 176

List of Tables

Tableau 0-1 Composition d'étude 2

Table 1-1 Chemical composition of steel studied 13

Table 2-1 The observed features and proposed mechanisms for the development of fibrous carbide 24

Table 2-2 A summary of the existing models for interphase precipitation in vanadium alloyed steels 32

Table 2-3 The equations for chemical or cutting strengthening mechanisms 68

Table 2-4 The used particle spacing in different approaches. 71

Table 3-1 Chemical compositions of Steel-A and Steel-B (wt%) 74

Table 3-2 The microstructural features of UHSBs 75

Table 3-3 The mechanical properties of UHSBs 76

Table 3-4 The parameters of dislocation density calculations obtained via TEM 81

Table 3-5 The summary of strengths contributed from different mechanisms 82

Table 5-1 The experimental data used for supporting the proposed numerical models 100

Table 5-2 A summary of the equations used in the calculations 113

Table 5-3 The parameters used in the calculations 117

Table 6-1 The features of interphase precipitation measured by TEM 135

Table 7-1 List of c^* given in Dao's study [108].....152

Table 7-2 The representative strains associated with different included angle [104] 153

Table 7-3 Mechanical properties of ferrite from nano-indentation of the as-received materials.....160

Table 7-4 The strengthening contribution to the global strength of ferrite in the steel studied.....166

Table 7-5 The estimated strain hardening exponent at different transformation temperature 167

Chaptier 0

Résumé

0.1 Introduction

La précipitation interphase conduit généralement à des durcissements très importants. Ce phénomène qui a reçu une attention particulière ces dernières années permettrait de développer de nouvelles nuances d'aciers à très haute résistance mécanique destinées au secteur de l'automobile et/ou de la construction. Il se caractérise par la précipitation de carbures de manière concomitante à l'avancée de l'interface austénite/ferrite. Il en résulte, généralement, un arrangement particulier des carbures. Une microstructure typique de ces phénomènes est présentée à la Figure 0-1.

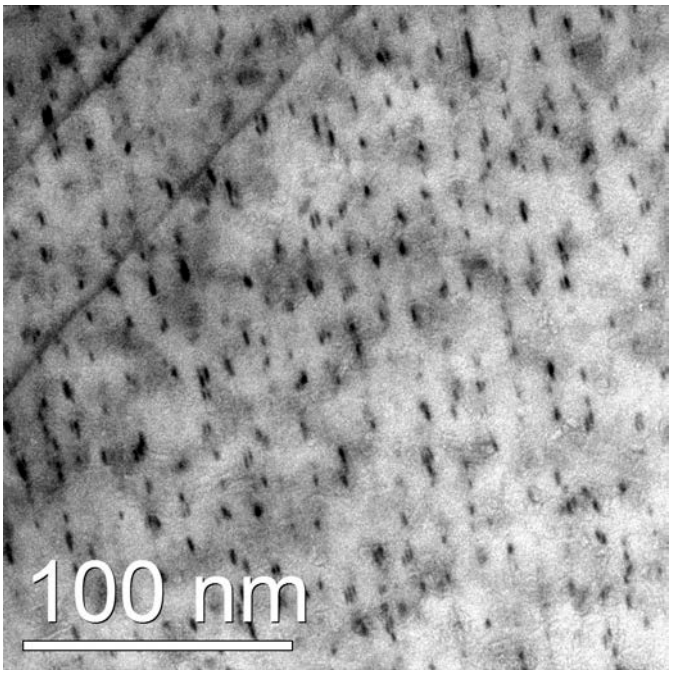

Figure 0-1 microstructure typique de précipitation interphase. On peut voir l'alignement typique des carbures

Généralement, on peut retenir que :

(1) la transformation de l'austénite en ferrite doit procéder par le mécanisme de migration de marches

(2) la réaction de précipitation se produit à l'interface en même temps que la transformation ferritique.

Les materiaux analysés dans cette thèse ont été fournis par Taiwan Tunghe Steel Corporation. Ils sont fournis sous forme de barreaux dont la composition est donnée dans le Tableau 0-1.

Tableau 0-1 Composition d'étude

	Composition chimique (%pds)					
	Diameter	C	Si	Mn	V	Nb
Steel-A	16 mm	0.37	0.26	1.10	0.26	0.04
Steel-B	36 mm	0.34	0.34	1.37	0.27	0.05
Steel-C	43 mm	0.36	0.33	1.35	0.33	-

Les analyses menées en Microscopie Electronique en Transmission (MET) ont permis d'étudier l'effet de l'état de précipitation (taille des particules, espacement des particules sur une ligne et entre les lignes) sur les propriétés mécaniques résultantes. A partir d'une double démarche de modélisation et expérimentale, nous montrons que l'arrangement des précipités résulte de l'interaction entre la transformation ferritique et la réation de précipitation.

Par ailleurs, nous avons aussi observé un changement topologique des carbures (carbures fibraire) lors d'un refroidissement lent (Figure 0-2). A partir du modèle

développé, nous proposons une analyse et une explication originale à ce phénomène.

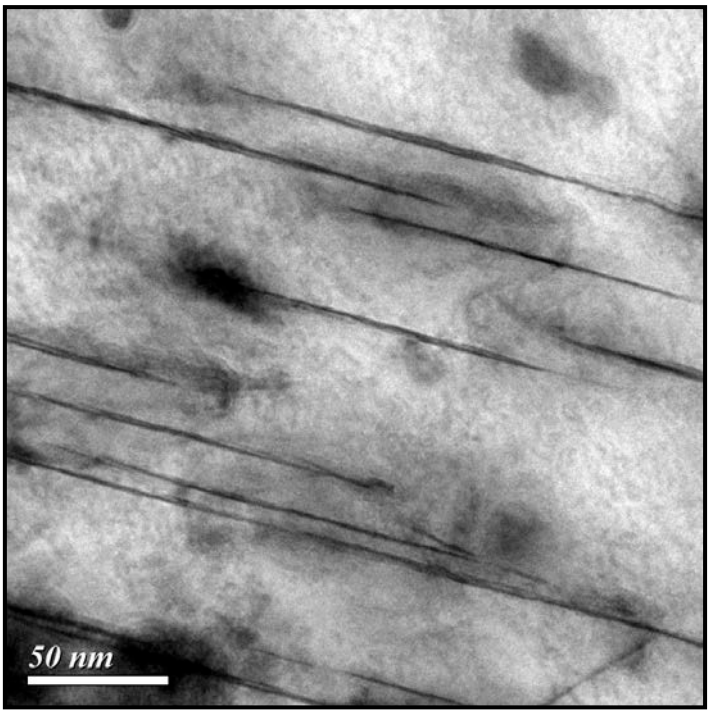

Figure 0-2 Précipitation de carbures fibreux obtenue lors d'un refroidissement lent.

0.2 Etude expérimentale de l'évolution morphologique des carbures lors de la transformation austénite/ferrite : précipitation interphase et fibreuse

Des traitements thermiques spécifiques ont été proposés afin d'étudier le type de carbures qui se formaient. Les traitements effectués à 650 ^{o}C montrent la présence d'une précipitation interphase caractérisée par l'alignement des carbures mais également la présence d'une précipiation de carbures fibreux comme en témoigne la Figure 0-3. En outre, le montage d'image MET (Figure 0-4) montre les séquences de précipitation durant l'avancée de l'interface austénite/ferrite. Cette séquence est caractérisée par la précipitation successive de carbures interphase, de carbures fibreux et de perlite. L'étude en MET (Figure 0-4) a permis d'étudier plus finement la transition entre précipitation interphase et précipitation carbures fibreux. Il est intéressant de remarquer que cette transition peut avoir lieu sans qu'il soit nécessaire de changer l'orientation de la matrice ferritque. L'analyse des relations d'orientation

entre la ferrite et les carbures suggère que les mécanisme de germination des carbures interphases et fibreux sont différentes. Le travail expérimental mené en MET est un pré-requis pour mieux comprendre les transitions topologiques observés. Le travail théorique couplés à ces analyses nous ont permis de proposer un mécanisme de formation de ces carbures fibreux.

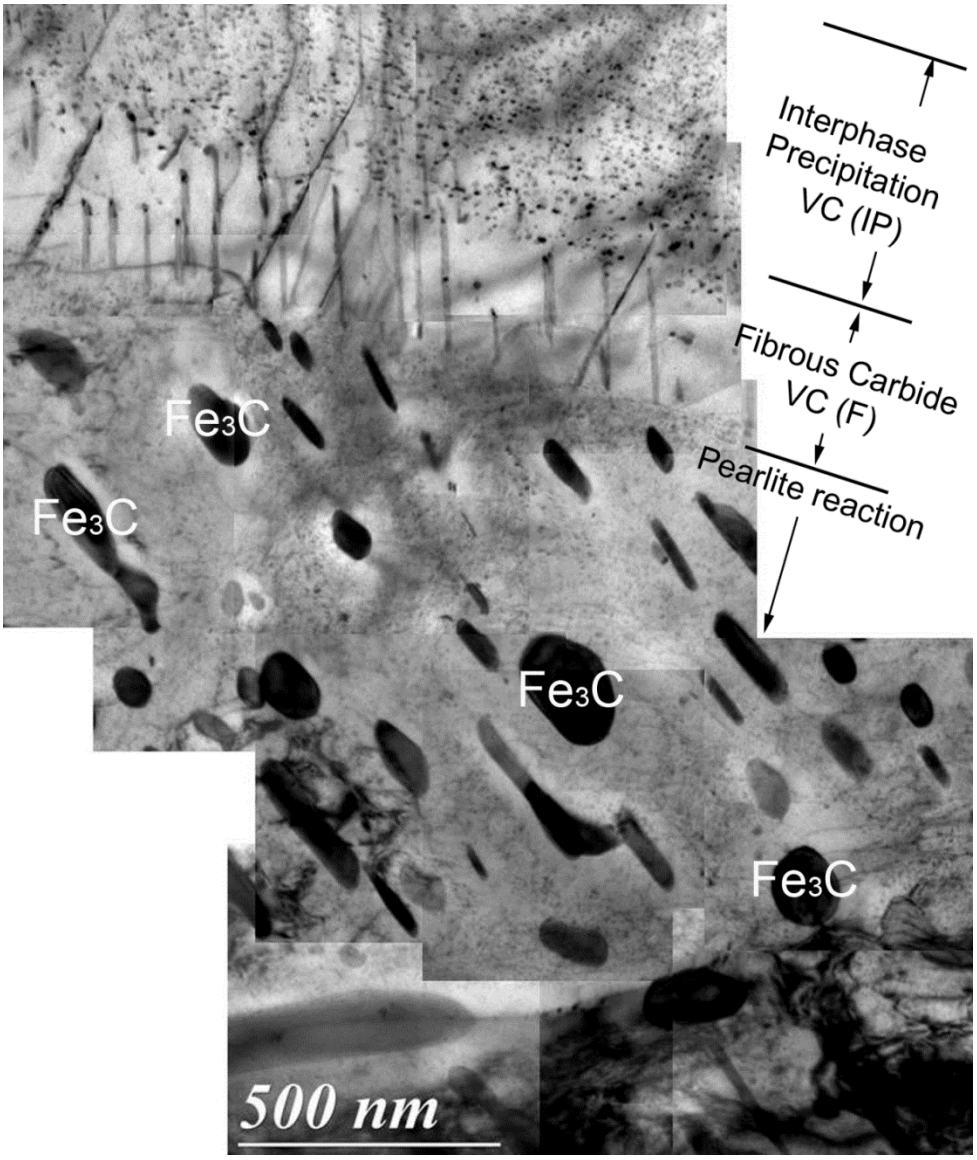

Figure 0-3 Séquences de précipitation lors de l'avancée de l'interface austénite/ferrite

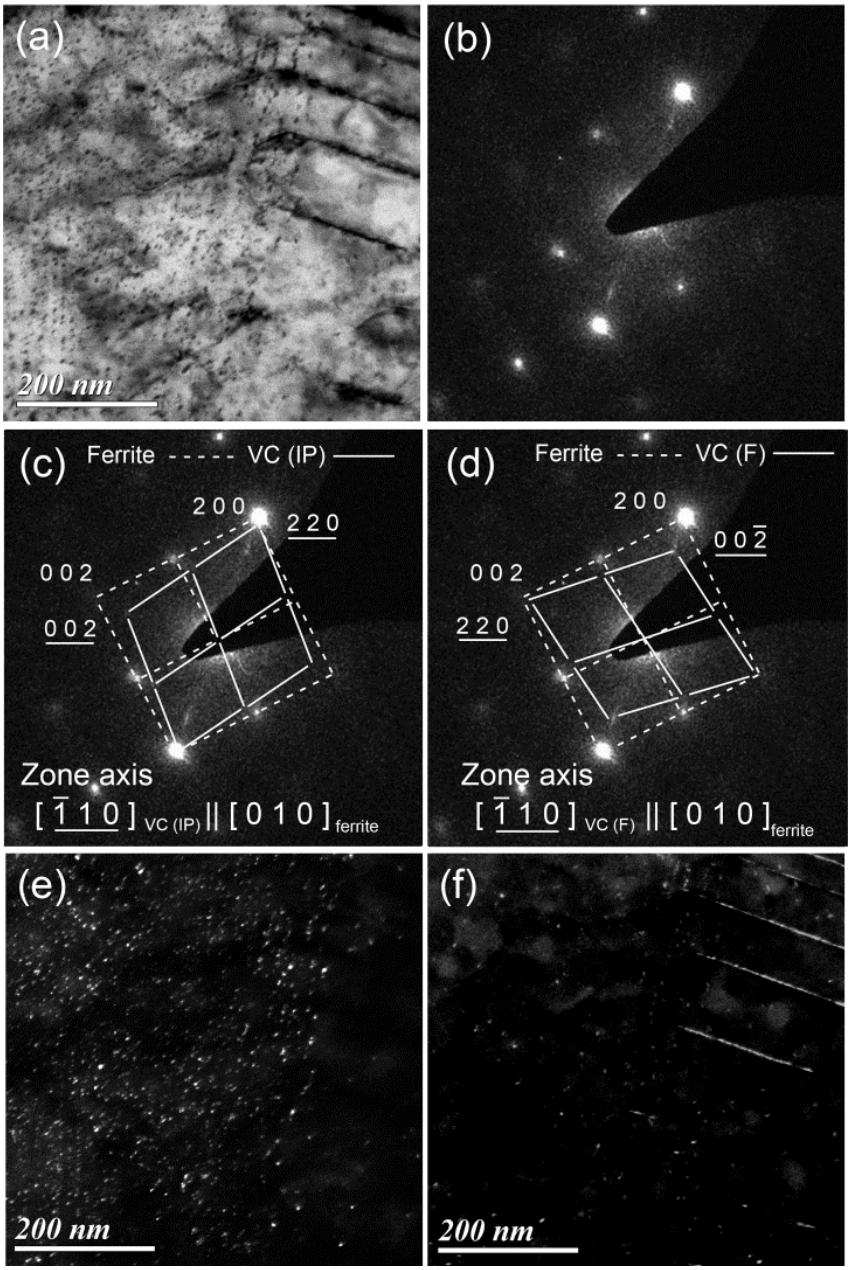

Figure 0-4 Une micrographie MET pris sur la région contenant la transition de précipitation interphase à la fibre de carbure, avec l'analyse de l'orientation crystallograhie

0.3 Modélisation de la précipitation interphase

Afin de comprendre la dépendance en température des caractéristiques de la précipitation interphase, un modèle a été proposé sur la base des deux considérations suivantes:

(1) la transformation austénite ferrite est contrôlée par le mécanisme de migration de marches

(2) La précipitation de carbures se produit à interface et simultanément

Le mécanisme proposé est résumé sur la Figure 0-5. Nous avons développé un modèle original appelé “superledge”, qui peut être utilisé pour prévoir l’espacement entre feuillets , l’espacement des carbures dans un feuillet, et la vitesse globale de l’interface. Les résultats expérimentaux obtenus sont alors comparés avec succès avec les résultats calculés par le modéle “superledge”.

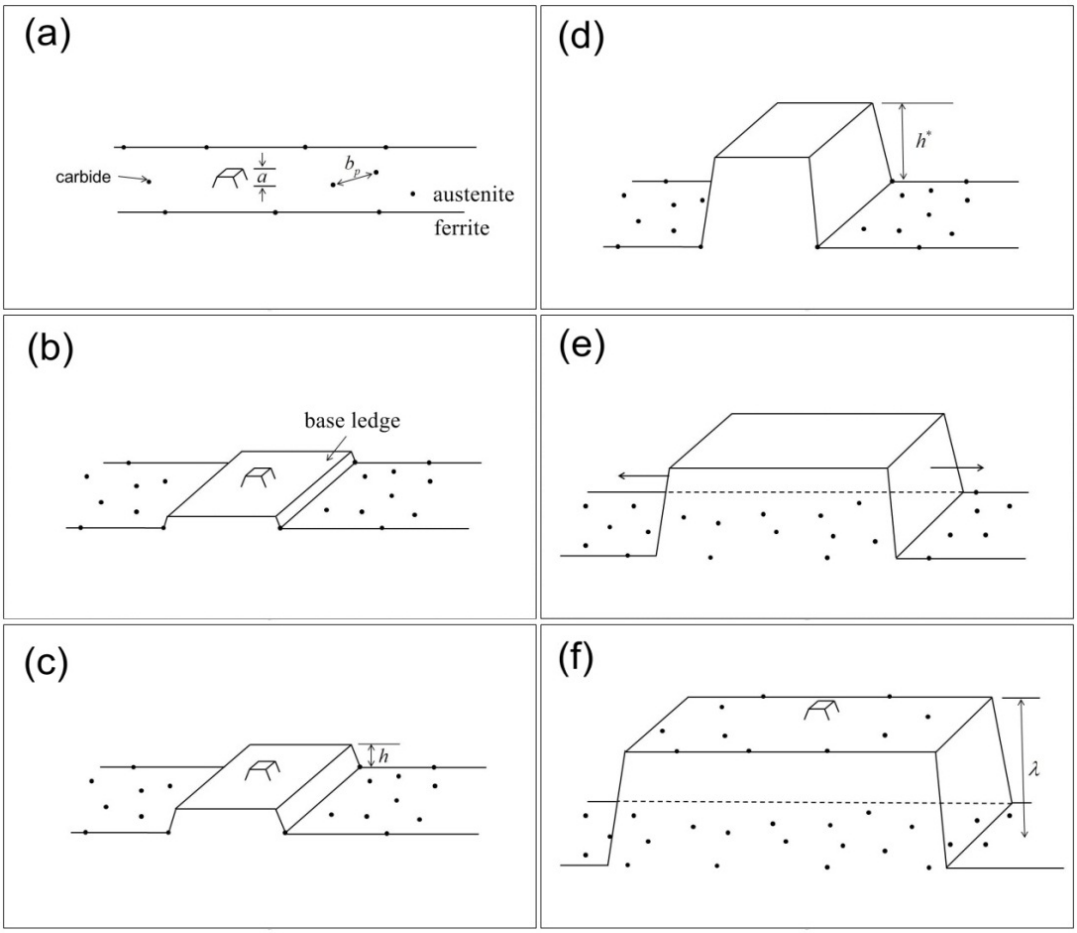

Figure 0-5 Shema des différentes étapes du modéle superledge

Nous avons également étendu le modéle « superledge » afin de décrire les évolutions des caractéristiques de précipitation interphase en cours de transormation ferritique. L'approche originale que nous avons développée permet d'interpréter les évolutions des états de précipitation. Cette approche met en exergue le couplage fort qui existe entre les forces motrices de transformation de la ferrite et les forces motrices de précipitation. Les deux phénomènes devant être pris en compte, de manière dynamique, afin de décrire l'evolution de la précipitation interphase. A ce titre, la Figure 0-6 met en exergue le bon accord qui existe entre les résultats du modèle et ceux expérimentaux.

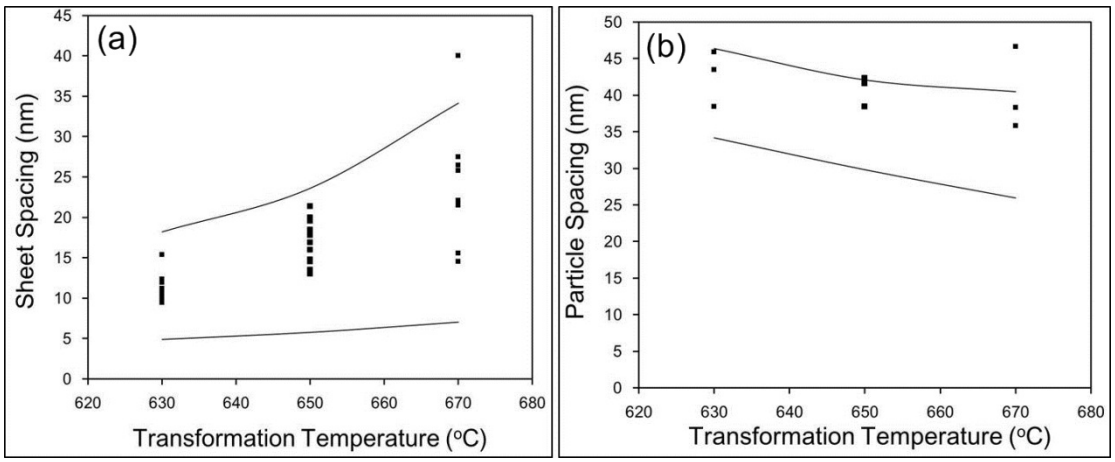

Figure 0-6 Evolution en fonction de la température des paramètres de la précipitation interphase. Comparaison entre les résultats du modèle.

0.4 Lien entre la microstructure et les propriétés mécanique

La dernière partie de cette thèse est consacrée à l'étude des propriétés mécaniques résultantes de la précipitation interphase. Dans cette étude, le durcissement a été étudié par nano-indentation car :

(1) les informations obtenues sont locales

(2) Le comportement élasto-plastique global de ferrite peut être obtenu par une analyse détaillée de la courbe de charge

L'idée sous-jacente est d'extraire, à partir d'essais de nano-indentation, la contribution au durcissement de la précipitation interphase : pour ce faire, les approches de Daoet Bucaille ont été utilisés. Les différentes contributions au durcissement peuvent alors être obtenues (Figure 0-7).

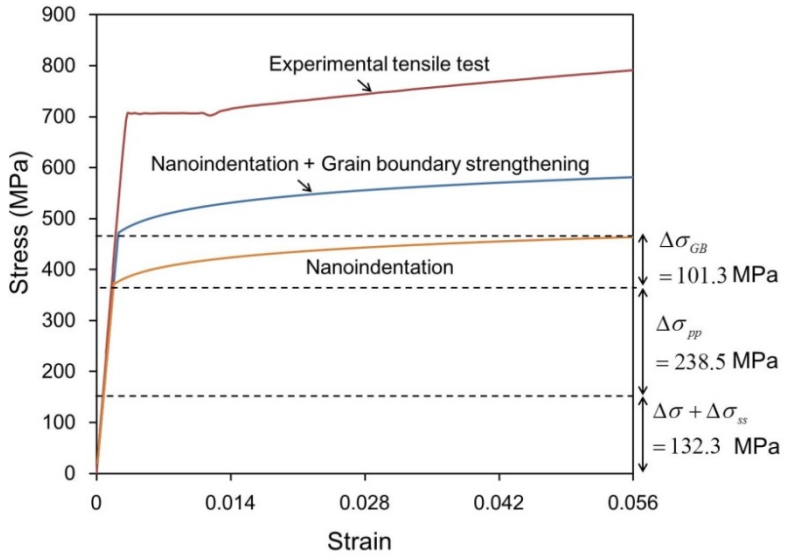

Figure 0-7 Les comportements élasto-plastique de ferrite calculé par les résultats de nanoindentation, et l'effet de taille de grain grain de ferrite est pris en compte

Les pricipaux résultats peuvent se résumer de la façon suivante :

(1) le coefficient d'écrouissage n'est pas sensible aux températures de transformation,

(2) le durcissement résultant est quant à lui dépendant de cette température de transformation,

(3) la limite d'élasticité est principalement contrôlée par l'espacement entre les feuillets et la taille des carbures alors que le taux d'écrouissage dépend de l'espacement entre particules.

Par ailleurs, nous montrons sans ambiguïté, que l'arrangement des précipités joue un rôle précondérant dans les propriétés résultantes. D'ailleurs, toute chose étant égal par ailleurs, il existe des situations où la contribution au durcissement dans le cas de la précipitation interphase est plus faible que celui obtenu dans le cas de particules réparties de manière aléatoire.

En résumé, la présente thèse est consacrée à la précipitation interface en les aciers alliés au vanadium. Elle est divisée en trois parties : l'étude de la microstructure, la modélisation et l'étude des propriétés mécaniques. Un organigramme de la thèse est présenté dans la Figure 0-8.

.

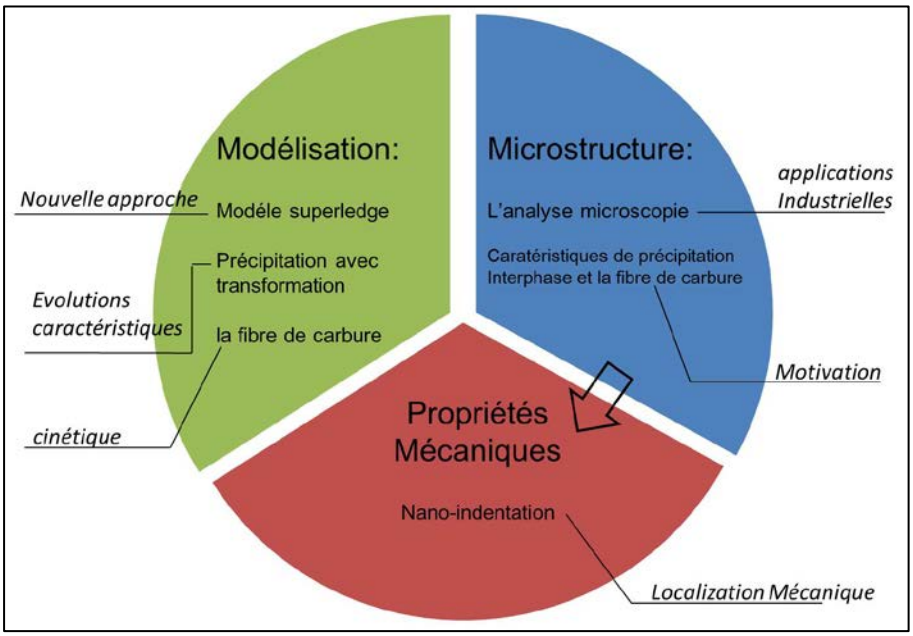

Figure 0-8 Les compositions de la thése

Abstract

The present thesis aims to examine the features of interphase precipitation and carbide fibers in a medium-carbon vanadium alloyed steel. It covers microstructure, modeling, and mechanical properties aspects of interphase precipitation and carbide fiber. The different features of interphase precipitation and carbide fiber are initially examined by TEM. The transition of the interphase-precipitated carbides to the fibrous carbides is discussed. It shows that the fibrous carbide would form at the later stage of the austenite-to-ferrite transformation, indicating that the occurrence of the fibrous carbide depends on the interface velocity. The conditions for the developments of the interphase precipitation and fibrous carbide are then clarified.

The obtained TEM results are then analyze to validate to a new model to elucidate the carbide precipitation with the growing ferrite phase. This new model is based on superledge mechanism of austenite-to-ferrite transformation. It deals with the ferrite and carbide nucleation rates and the driving force for austenite-to-ferrite transformation at the same time. The model gives good results at low transformation temperatures (< 700 ^{o}C) and reveals the evolutions of characteristic features of interphase precipitation with the progressive of austenite-to-ferrite transformation. The proposed superledge model is then extended to develop a model for carbide fiber growth and to understand the effect of carbon and solute contents on interphase precipitation in alloyed steels. .

Finally, local mechanical properties were characterized by the use of nanoindentation after the samples were isothermally transformed at different temperatures. It gives the elasto-plastic mechanical behaviors of the ferrite strengthened by interphase-precipitated carbides. The characteristic features of interphase-precipitated carbide predicted by the model are used to be incorporated

with tested mechanical properties. For the steel strengthened by the interphase-precipitated carbides, the contributed yield strength by these carbides is measured and the link between precipitation state and resulting mechanical properties are discussed. Finally, from a theoretical analysis, we show that precipitation state topology plays a key role in mechanical properties. The results presented in this thesis are expected to provide some original information related to the interphase precipitation in medium carbon alloyed steels.

Therefore, the results presented in this thesis are expected to provide further information of the interphase-precipitated carbides in medium carbon alloyed steels. The following research results have been and are going to be published in the international journals:

Advanced materials research (EI)

Scripta Materialia (SCI)

Institute of Iron and Steel of Japan (ISIJ)

Acta Materialia (SCI)

Keywords: *ultra-high strength steels, carbide, interphase precipitation, modeling, superledge, ferrite, transformation, nano-indentation*

Chapter 1

General Introduction

Owing to increase the strength of steel without modifying the main microstructure, precipitation hardening has been known to be an efficient way to reach this goal. The basic idea is to form high density of carbides dispersed in matrix by introducing certain strong carbide-forming elements, for example, Ti, Nb, Cr, V …etc. Then, precipitation hardening can be used to develop advanced ultra-high strength low-alloyed steels in automobile and construction applications. The mechanical properties of these products are associated with the size, distribution, density, and morphology of the carbides. In additional to pearlitic cementite (Fe_3C) and supersaturated precipitation, there are two special carbide aggregates have been received great attentions in these years: the interphase-precipitated carbide and the fibrous carbide.

For the case of interphase precipitation, the precipitation process is related to the ledge migration of ferrite/austenite interface. The precipitation of carbide mainly occurs on the relative immobile terrace plane of ferrite matrix. However, the mobile steps are carbides free because of their high mobility. Comparing to the interphase-precipitated carbides, the number of studies dedicated on fibrous carbides is very limited and there is still a lock of data and analysis that rest on both experimental and theoretical data. Edmonds firstly discussed the different growth mechanisms of interphase precipitation and carbide fiber, and concluded that the higher Mn addition, the higher volume fraction of fibrous carbide in ferritic matrix. In certain circumstances, the platelet interphase-precipitated carbide would transit into a fibrous morphology. However, the competition in the growth mechanisms of these

two carbide aggregates is still unclear.

The as-received materials are medium-carbon steels bars micro-alloyed with V and V-Nb provided by Taiwan Tunghe Steel Enterprise. The detailed chemical composition is summarized as follows:

Table 1-1 Chemical composition of steel studied

	Diameter	C	Si	Mn	V	Nb
Steel-A	16 mm	0.37	0.26	1.10	0.26	0.04
Steel-B	36 mm	0.34	0.34	1.37	0.27	0.05
Steel-C	43 mm	0.36	0.33	1.35	0.33	-

The steel bars with different diameters were manufactured in order to meet specific requirements of construction [1]. In steel-C, the interphase-precipitated carbides and the fibrous carbides are both observed in ferritic matrix by TEM. It could be resulted from (1) sufficient Mn addition, and (2) the larger specimen leads to a slower cooling rate. Therefore, steel-C could be very suitable for investigating the morphological features of the interphase-precipitated carbide and the fibrous carbide and for understanding the competition of these two carbide aggregates. The microscopic information is then useful either for developing the models to describe the formation mechanisms of interphase precipitation and fibrous carbide or for interpreting the effect of carbide distribution on the strengthened ferritic matrix.

In the present thesis, Chapter 2 firstly provides a review of the precipitation of carbide in alloyed steels. The review concerns with microstructure, modeling, and mechanical properties. It gives the aspects of the precipitation of carbide in alloyed steels. Chapter 3 then shows the detailed investigations of these steel bars. The strengthening contribution of the interphase-precipitated carbide has been

quantitatively estimated, and the motivation of the present dissertation is subsequently pointed out by the observations of the two carbide aggregates in steel-C. Steel-C is used in the following chapters and is machined into dilatometric samples for further heat treatments. Chapter 4 discusses the competition between the interphase-precipitated carbide and the fibrous carbide based on TEM investigations. The formation of interphase precipitation and carbide fiber have been clarified and compared. The results show that the change in carbide morphology is controlled by the velocity of interface, related to the thermodynamic and kinetic of austenite-to-ferrite transformation. A model is then proposed to describe the sequence and to predict the features of interphase precipitation. The modeling works are based on an international program in collaboration with Professors Bréchet, Gouné and Militzer. The developments of model and its relevant applications are presented in Chapter 5 and Chapter 6. The model now is successfully developed and called as the superledge model. By giving the transformation temperature and the associated chemical composition, it predicts the features of interphase precipitation by considering the interaction of the carbide and mobile steps on a ledged ferrite/austenite interface. Besides, this model is also extended to understand the feature evolutions of interphase precipitation with the progressive of austenite-to-ferrite transformation, and then a mechanism is proposed for the carbide fiber formation. Finally, the ferrite strengthened by interphase precipitation is examined by nanoindentation. By this approach, the work hardening behavior and the yield strength of ferrite at different transformation temperature can be presented, and the corresponding elasto-plastic behavior can be simulated as well. Furthermore, a method for measuring the Orowan contribution of interphase precipitation in ferrite is proposed. The obtained results are in good agreement with those calculated. Finally, the effect of the arrangement of interphase-precipitated carbides on resulting

strengthening is discussed.

The present thesis entitled as "*A study of interphase precipitation in Fe-V-C alloyed steels: the Microstructure and the Modeling*" attempts to give a comprehensive study of the features of interphase precipitation and carbide fiber and to inter-connect their relations of microstructures, modeling, and mechanical properties.

Chapter 2

Literature Review

The interphase-precipitated carbides and the fibrous carbides have been studied in the ferrite matrix. It has been shown to improve the strength of steel efficiently. It is worth understanding the formation mechanisms of the two carbides and their characteristic features. In the past decades, the precipitation of the interphase-precipitated carbide and of the fibrous carbide had been observed either in proeutectoid ferrite [2-4] or in pearlitic ferrite [5-8]. The relevant models were then proposed to illustrate the developments of interphase precipitation [9-13] and carbide fiber [3]. Besides, the relations of the mechanical properties with the observed microstructures have been proposed as well [14-20]. In this chapter, the microstructures, the models, and the mechanical properties of interphase precipitation in micro-alloyed steels are reviewed. This literature survey is essential to clarify the unsolved issues for the further investigations.

2.1 Precipitation in ferritic matrix

a. The interphase precipitation

The interface is known to be a topic of interest in the field of solid transformation [21-26]. The term “interphase precipitation” represents the carbide nucleation process repeats periodically during the austenite-to-ferrite transformation, resulting in a sheeted structure[2, 27]. Such carbide dispersion and morphology have been reported to depend on the transformation temperature. One of the proposed classifications is shown in Figure 2-1.

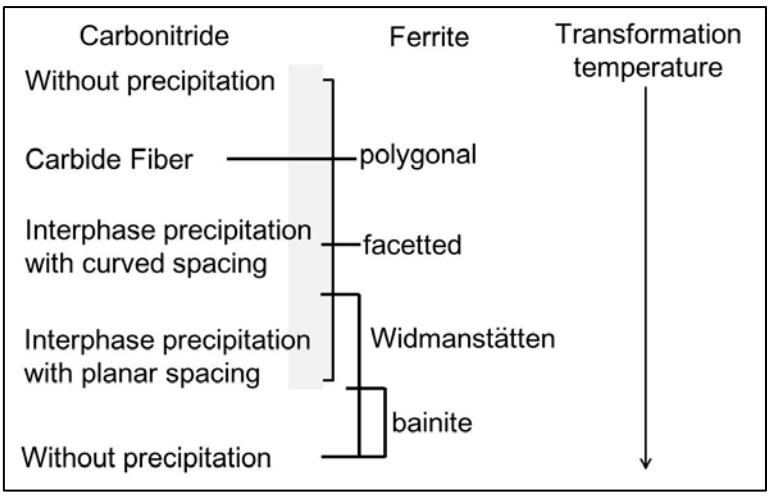

Figure 2-1 The variations of carbide morphology with transformation temperatures [28]

The microstructure of the interphase-precipitated carbide was studied by Honeycombe *et al.* via TEM in different alloyed steels. The interphase-precipitated carbide obeys one variant of Baker-Nutting orientation relationships, $\{001\}_{carbide} \parallel \{001\}_{\alpha}$ and $<110>_{carbide} \parallel <100>_{\alpha}$. The single variant selection of IP carbides is explained to minimize the interfacial energy and to maximize the diffusion efficiency of solute atoms.

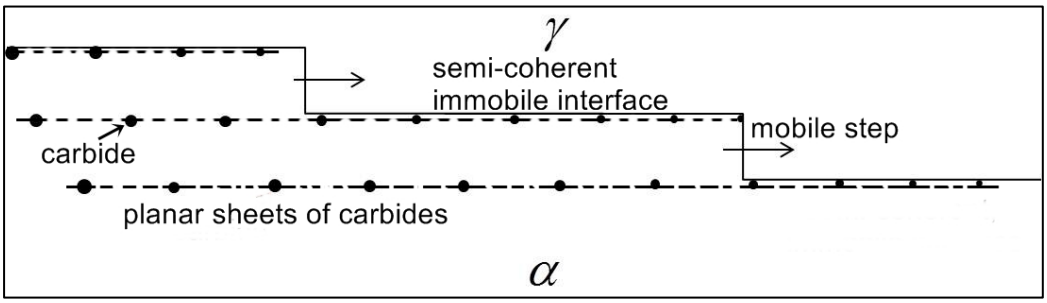

Figure 2-2 Schematic diagram showing the interphase-precipitated carbides with planar spacing

The process of interphase precipitation (with planar spacing) is briefly described in Figure 2-3. During γ to α transformation, the formation of α increases the carbon content in front of the ferrite/austenite interface. As the carbon concentration

reaches a critical value, alloy carbides would start to precipitate on the ferrite/austenite interface. The formation of carbide lowers the carbon content ahead of interface, increasing the driving force for austenite to ferrite transformation. The interface then advances and the above process repeat periodically, leading to dense of carbides arranged in regular spacing.

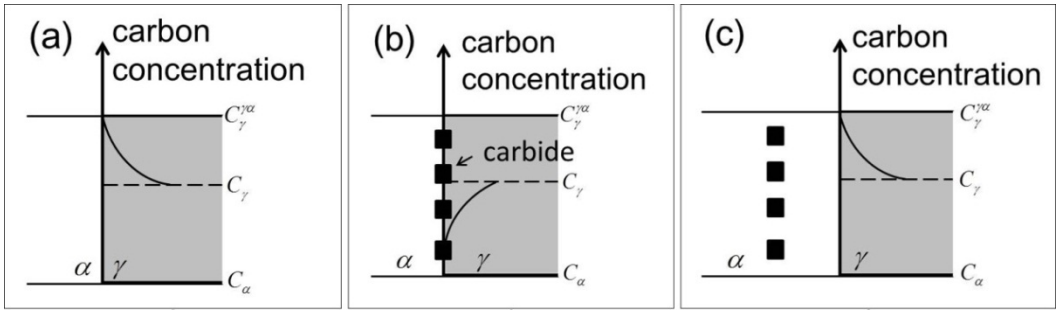

Figure 2-3 The carbon concentration profile ahead of ferrite/austenite interface during interphase precipitation process [29]

The ledge mechanism of austenite-to-ferrite transformation is viewed as the spirit of interphase precipitation [30-33]. A typical ledge structure of interface contains a broad plane and a mobile step, which are illustrated in Figure 2-4. The overall growth rate of a ledged interface, V, depends on the ledge height, h, and its spacing, b:

$$V = V_s \frac{h}{b} \tag{2-1}$$

where V_s is the step velocity, h is the ledge height, and b is the spacing of ledges.

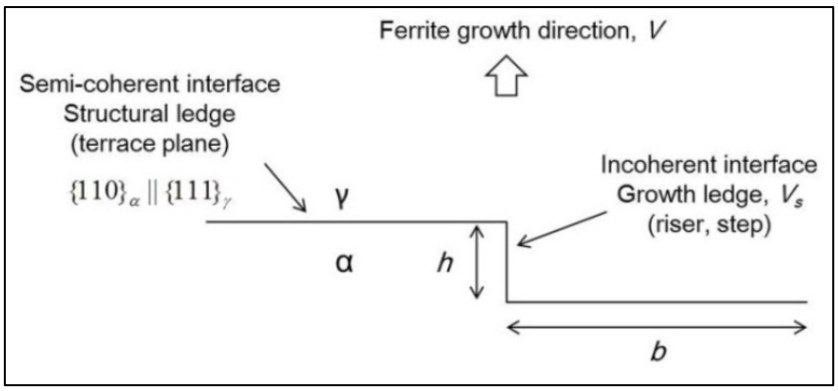

Figure 2-4. Schematic illustration showing a unit ledge accompanying with features of interests. The meanings of each term are referred to the text.

Based on the point of view of Honeycombe *et al.,* the broad interface is supposed to be semi-coherent. Ferrite follows $\{110\}_\alpha \parallel \{111\}_\gamma$ Kurdjumov-Sachs orientation relationships with respect to the parent austenite. On the contrary, the mobile steps are incoherent. Based on the metallurgical considerations, these steps are assumed to be the preferred carbide nucleation sites. However, in the case of interphase precipitation, these steps move too fast during transformation, making the carbide nucleus difficult to nucleate on them. Instead, carbides prefer to precipitate on coherent/semi-coherent interfaces, leading to interphase precipitation.

In addition to the planar interphase precipitation, other mechanisms had been proposed to explain the interphase precipitation with curved spacing. Ricks and Howell proposed the bowing mechanisms (for curved interphase precipitation with ***irregular spacing***) and quasi-ledge mechanisms (for curved interphase precipitation for ***regular spacing***) to illustrate the curved interphase precipitation [34, 35]. The bowing mechanism, as shown in Figure 2-5, requires the carbides to pin the moving interface. It can be expected that the carbide density and the particle spacing in rows determine the resulting sheet spacing. For quasi-ledge mechanism (Figure 2-6), the interface breaks into austenite at the place where the particle spacing is relatively

wider. The segment of the advancing interface accumulates sufficient carbon and solute, and then carbide starts to precipitate on its top. The newly formed carbide pins the advancing interface again, the mobile steps then move by sideway. Obviously, the carbide distribution determines which mechanism, bowing and quasi-ledge, is operated during transformation.

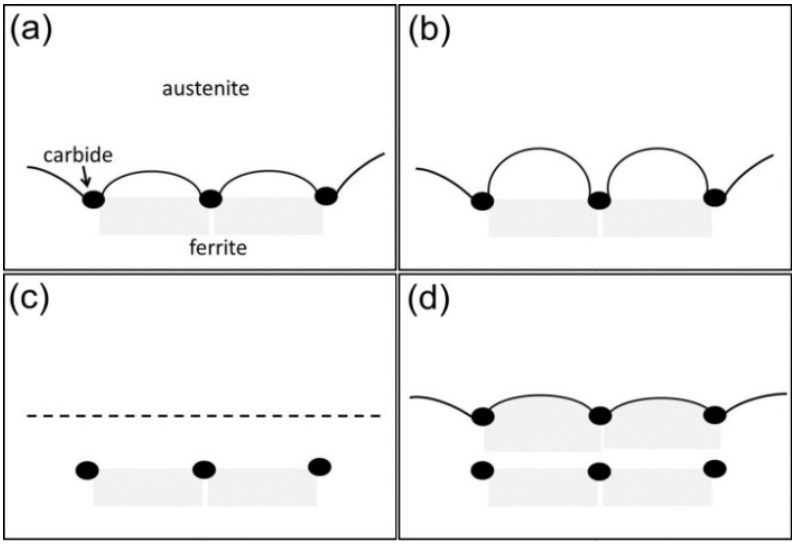

Figure 2-5 The bowing mechanism for the curved interphase-precipitated carbides with irregular spacing [34]

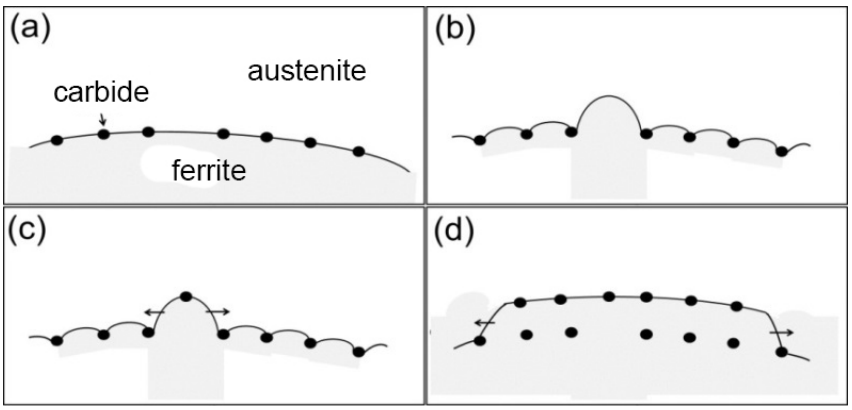

Figure 2-6 Schematic illustration of quasi-ledge mechanism of curved interphase precipitated carbides with regular spacing [34]

b. The carbide fiber growth

In addition to interphase precipitation, another carbide aggregate: carbide fiber, is usually found in Fe-Mo-C, Fe-Cr-C, and Fe-V-C steels as well, but the strengthening mechanism of fibrous carbide in ferrite is less discussed [36]. The observed features and proposed formation conditions for fibrous carbide are summarized in Table 2-1. Carbide fibers are known to be straight and branchless, generally growing in a single direction normal to the transformation interface. The occurrence of fibrous carbide depends on transformation temperature, chemical composition, and the nature of interfaces. The related literatures have been reviewed and the important concepts and ideas are summarized as follows:

(1) The carbide fiber in the Fe-V-C Steel

Generally, the addition of vanadium is widely used to strengthen steels by interphase precipitation hardening due to the temperature for precipitation is approximately close to austenite to ferrite transformation [37, 38]. The occurrence of alloy fiber in Fe-V-C steels is not greatly reported. Edmonds studied the VC fibers by varying cooling rate and by changing the content of Mn [3]. He found that as the amount of Mn was elevated from zero to 1.6 wt%, the density of VC fibers was increased of 50%.

The Mn has been reported to have strong effects on slowing down the advancement of the transformation interface [39]. Edmond's works indicate that the interface mobility is an important role in carbide morphology determination. He suggested that a higher transformation temperature would be favored for the development of fibrous carbide and pointed out that the selection of habit plane is a function of the transformation temperature. For interphase-precipitated carbide, its habit plane is expected to be as parallel to the interface because that minimizes the

interfacial energy and maximizes the diffusion of solute atoms [28]. However, the habit plane of VC does not to be as parallel to the transformation interface at the high transformation temperature because the solute now requires sufficient energy [28]; the formation of fibrous carbide becomes possible. These results indicate that the change in carbide morphology requires changing the transformation temperature.

VC carbide is f.c.c structure. The Baker-Nutting orientation relationships [40, 41] are commonly found for these carbides with respect to ferrite:

$$\begin{pmatrix}1 & 0 & 0\end{pmatrix}_{VC} \parallel \begin{pmatrix}1 & 0 & 0\end{pmatrix}_{\alpha}$$

$$\begin{bmatrix}0 & 0 & 1\end{bmatrix}_{VC} \parallel \begin{bmatrix}0 & 1 & 1\end{bmatrix}_{\alpha}$$

The structure of VC fiber is identical as that of interphase precipitated VC carbide. Berry had claimed that the VC fibers exhibited Kurdjumov-Sachs orientation relationships with respect to ferrite [42]:

$$\begin{pmatrix}1 & 1 & 1\end{pmatrix}_{VC} \parallel \begin{pmatrix}1 & 1 & 0\end{pmatrix}_{\alpha}$$

$$\begin{bmatrix}1 & \bar{1} & 0\end{bmatrix}_{VC} \parallel \begin{bmatrix}1 & \bar{1} & 1\end{bmatrix}_{\alpha}$$

The difference in orientation relationships implies the nucleation and growth of carbides follow different process. If the VC fibers follow Kurdjumov-Sachs orientation relationships with respect to ferrite, the nuclei of fibers are formed at the side of austenite at the austenite/ferrite interface, then growing in austenite, instead of ferrite. Otherwise, if Baker-Nutting orientation relationships are followed by ferrite and carbide, the development of carbides is related to ferrite, not austenite. The

orientation relationships of carbide with respect to austenite reveal important information of where nucleation and growth of carbide occur. The detailed results and discussions will be presented in the next chapter.

Table 2-1 The observed features and proposed mechanisms for the development of fibrous carbide

Reference	Basis of proposition	Features for carbide fiber	The clarified features
Barbacki and Honeycombe [43]	● Interphase precipitation on a semi-coherent interface (ledge mechanism)	● Transition in morphology without changing matrix orientation ● Plane normal to the interface (incoherent) becomes dominant for precipitation by decreasing temperature ● Curved interface is required ● The carbide aggregates are controlled by changing transformation temperatures.	● VC fiber still follows Baker-Nutting orientation relationships with respect to ferrite ● Coherency of interface would not be the factor controlling carbide morphology. Interphase precipitation does not have to be related a semi-coherent interface, so does carbide fiber ● Carbide fiber does not have originate from prior austenite grain boundary ● The transition of carbide morphology does not have to be associated with changing transformation temperature
Bee and Campbell [44, 45]		● Carbide fiber is in the side of ferrite without Kurdjurmov-Sachs orientation relationship and interphase precipitation in the other side. ● Carbide fiber originates from prior austenite grain boundary	
Berry and Honeycombe [42]		● Higher transformation is favored for carbide fiber ● VC fiber and ferrite matrix follows Kurdjurmov-Sachs orientation relationships	
Edmonds [3]	● The ledge mechanism was not emphasized	● Higher transformation temperature is favored because the habit plane does not have to be parallel to the interface. ● Higher addition of Mn promotes the formation of carbide fiber. ● Carbide fiber can develop inside the ferrite grain. ● Change in carbide morphology has to be associated with changing transformation temperatures	

(2) The carbide fiber in the Fe-Cr-C steel

The carbide fibers in isothermally transformed Fe-Cr-C steels were studied by Bee [44] and Campbell [45] *et al*. The interphase-precipitated carbides and the fibrous carbides were both observed among these works. From their TEM evidence, they pointed out that interphase precipitation was related to a stepped interface, but the carbide fiber was in associated with curved interfaces (Figure 2-7). They then concluded that the formation of the interphase-precipitated carbide or the fibrous carbide would be controlled by the coherency of interface.

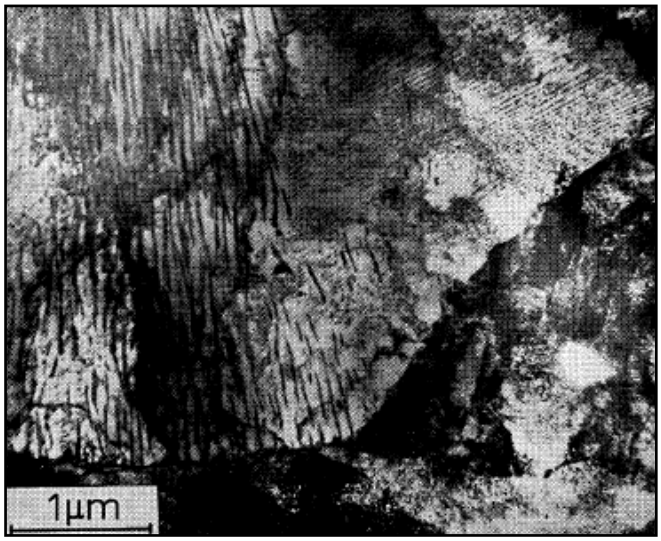

Figure 2-7 Fe-5Cr-0.2C (wt%) isothermal transformation at 650 ^{o}C for 30 min showing the interfaces associated with interphase precipitation (Right-hand side) and alloy fibers (Lef-hand side) [45]

Furthermore, two kinds of carbide fiber were found (M_7C_3 or $M_{23}C_6$). The examinations showed that the chemistry of carbide depends on the transformation temperature only. As transformation temperature is lowered, the spacing of fibers becomes finer, and the chemistry of carbide changes from $M_{23}C_6$ to M_7C_3.

The crystal structures of $M_{23}C_6$ and M_7C_3 are f.c.c. and h.c.p., respectively. For $M_{23}C_6$, the orientation relationships of these fibers with respect to ferrite were identified as:

$$\left(1\ \ 1\ \ 1\right)_{M_{23}C_6} \parallel \left(1\ \ 1\ \ 0\right)_{\alpha}$$

$$\left[1\ \ \bar{1}\ \ 0\right]_{M_{23}c_6} \parallel \left[1\ \ \bar{1}\ \ 1\right]_{\alpha} \qquad \text{Type I}$$

which are known as Kurdjumov-Sachs orientation relationships. For M_7C_3, which the structure is h.c.p., the orientation relationships with ferrite had been identified as follows:

$$\begin{aligned} &\left(0 \quad 0 \quad 0 \quad 1\right)_{M_7C_3} \parallel \left(0 \quad 1 \quad 1\right)_{\alpha} \\ &\left[1 \quad 1 \quad \bar{2} \quad 0\right]_{M_7C_3} \parallel \left[1 \quad 0 \quad 0\right]_{\alpha} \end{aligned} \qquad \text{Type II}$$

Bee and Campbell considered the carbide morphology was related to crystallographic of ferrite/austenite interface. As austenite starts to decompose to ferrite, ferrite initially nucleates on prior austenite grain boundaries. In the growing stage, this ferrite nucleus would not possess any orientation relationships with respect to the austenite into which it is growing (for the case of allotriomorphic ferrite). The other side where growth of ferrite does not occur, the ferrite and austenite exhibit Kurdjumov-Sachs orientation relationships. Thus, it is expected that the carbide fibers would form predominantly at the side of austenite where the ferrite is growing into, and interphase precipitation would occur at the other side of ferrite/austenite interface that follows Kurdjumov-Sachs orientation relationships. This argument is consistent with that proposed by Honeycombe *et al.* It implies that austenite/ferrite interfacial structures could be another factor on determining carbide morphologies but the above suggestions cannot explain the transition in carbide morphologies.

(3) The carbide fiber in the Fe-Mo-C steel

The carbide fibers formed in Fe-Mo-C steels were widely studied by Edmonds and Honeycombe *et al* [8, 46]. Three morphologies, interphase precipitation, Widmanstätten arrays, and carbide fibers were found in this alloyed system, as demonstrated in Figure 2-8.

The carbide in Fe-Mo-C steels is mainly Mo_2C with h.c.p structure. The analysis on the diffraction patterns showed that there are two orientation relationships of carbides with respect to ferrite. The orientation relationships of Mo_2C with respect to ferrite are:

$$\left(0 \quad 0 \quad 1\right)_{\alpha} \parallel \left(0 \quad 0 \quad 0 \quad 1\right)_{Mo_2C}$$

$$\left(1 \quad \bar{1} \quad 1\right)_{\alpha} \parallel \left(1 \quad \bar{2} \quad 1 \quad 0\right)_{Mo_2C} \qquad \text{Type I}$$

However, for the carbides that arranged in Widmanstätten way and interphase-precipitated carbide, the orientation relationships become to be:

$$\left(0 \quad 1 \quad 1\right)_{\alpha} \parallel \left(0 \quad 0 \quad 0 \quad 1\right)_{Mo_2C}$$

$$\left(1 \quad 0 \quad 0\right)_{\alpha} \parallel \left(1 \quad 1 \quad \bar{2} \quad 0\right)_{Mo_2C} \qquad \text{Type II}$$

Such orientation relationships were also confirmed by other studies.

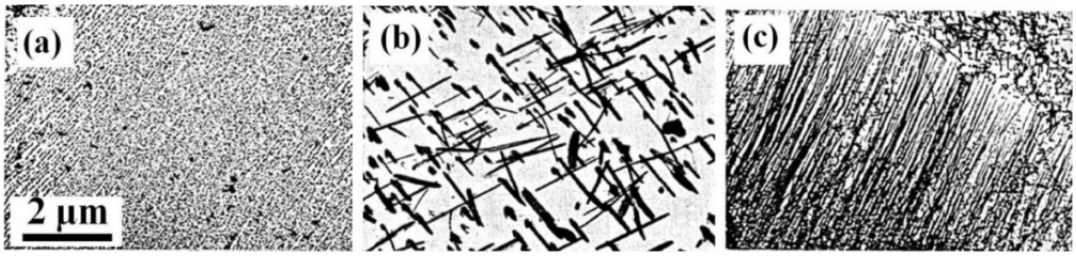

Figure 2-8 Mo_2C carbides with different morphologies in Fe-3.5Mo-0.22C (wt%) steels after isothermal transformation at 750 ^{o}C for 30 min. (a) interphase precipitation, (b) Widmanstätten arrays, and (c) Mo_2C fibers [46]

c. The transition in carbide morphology

The change in carbide morphologies is an important issue in alloyed steels because it directly affects performed mechanical properties. The transition in carbide morphologies was investigated by Barbacki and Honeycombe in Mo and V containing steels by simply altering the transformation temperatures [43]. These fibers mainly originated from curved interfaces, and with different spacing as the transformation temperature was changed (Figure 2-9). Even though the carbide morphology and its distribution are controlled by the transformation temperature, the transition in carbide morphology should not be associated with altering the orientation of ferrite matrix.

Compared to Edmonds' proposal, they thought that the carbide fibers were

predominant at lower transformation temperatures. There explanation was based on both transformation kinetics of Mo containing steels and misfits that result from different crystal structures of carbide/ferrite and carbide/austenite. By decreasing the transformation temperature, the solute atoms would mainly diffuse along the incoherent. For the ledge mechanism of austenite-to-ferrite transformation, the terrace plane was viewed as a semi-coherent interface for precipitation. Consequently, the carbide would like to precipitate on the mobile steps as the transformation temperature is lowered, and then grow in a direction perpendicular to the transformation front. However, this feature is not seen in other systems. For Fe-Cr-C and Fe-V-C steels, the fibrous carbides were found to be majority at higher transformation temperatures, instead of lower transformation temperatures.

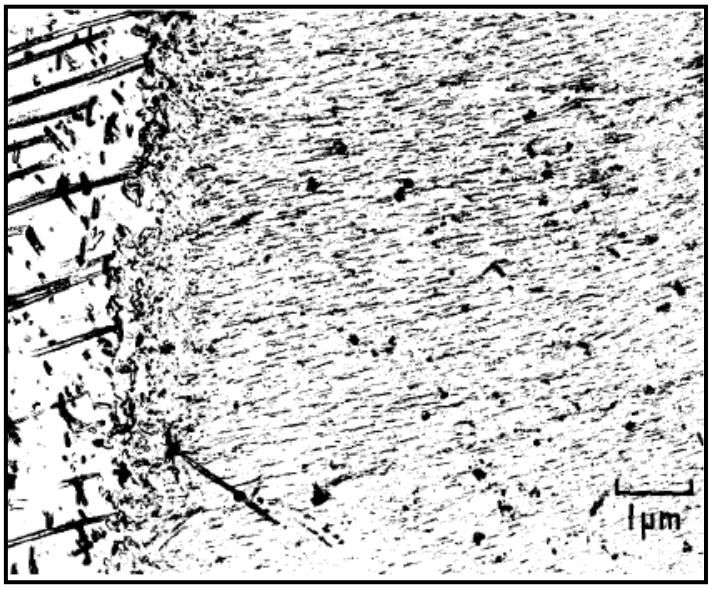

Figure 2-9 Fe-4Mo-0.2C (wt%) steels showing the spacing and fineness of fibers changed as transformation temperature was varied from 850 ^{o}C (left-hand side) to 750 ^{o}C (right-hand side) [43]

2.2 Precipitation in pearlitic ferrite

The pearlite reaction inevitably occurs after the interphase precipitation as the nominal content of carbon is increased. Previous sessions are all focused on the presence of carbides (interphase precipitation or carbide fiber) in proeutectoid ferrite. As the carbon and solute contents increase, the carbide precipitation is capable to occur in pearlitic ferrite [6, 47-50]. The interphase-precipitated carbides in pearlitic ferrite had been reported to have smaller size and finer sheet spacing than that precipitated in proeutectoid ferrite [51] because certain amount of C is consumed by

the formation of Fe_3C. Parsons *et al*. [52] used ledge mechanism to interpret such phenomenon, as shown in Figure 2-10. Moreover, if sufficient manganese (13 wt%) is added, which decelerates austenite to ferrite transformation, carbide fibers were found in the pearlitic ferrite [5], as shown in Figure 2-11. However, the occurrence of fibrous carbide in pearlitic ferrite was not deeply addressed.

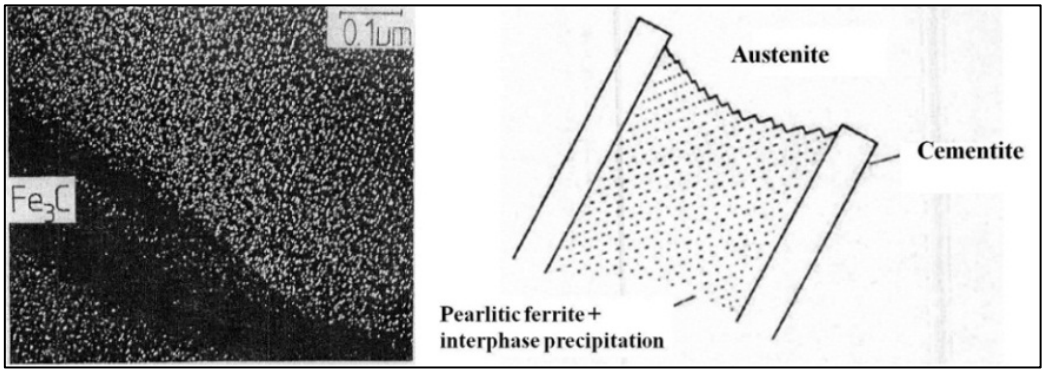

Figure 2-10 Proposed ledge mechanism illustrating interphase precipitation in pearlitic ferrite [52]

Figure 2-11 The observed fibrous carbides in pearlitic ferrite, a dark-filed image [5]

The presence of interphase precipitated carbide or VC fibers in pearlitic ferrite arises the problems on the nature of interface again. Zhou and Shiflet [48, 53] proposed the growth of pearlite in austenite is indeed associated with small ledges at the interface based on their TEM observations (Figure 2-12). The growing pearlite/austenite interface has been viewed as an incoherent interface [54, 55]. The observed interphase-precipitated carbide and fibrous carbide imply that the coherency

of the interface would not be the main factor in determining carbide morphologies.

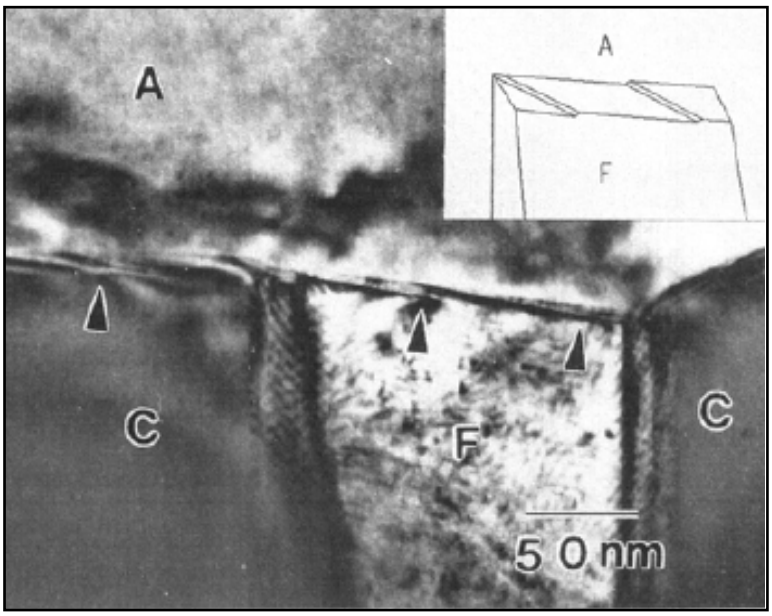

Figure 2-12 The observed growth ledge on the pearlite/austenite interface [48]

2.3 Models for interphase precipitation in vanadium alloyed steels

As discussed before, the proposed mechanisms of interphase precipitation are mainly based on microscopic observations. It was clearly showed that sheet spacing and carbide distribution depend on temperature. However, they are unable to give detailed understandings of precipitation processes and to give prediction of the features of interphase precipitation as the transformation temperature and the chemical composition of steel are given. For examples, it is deficient to explain: (a) the repeat nucleation process of precipitation along the interface boundary; (b) the uniform size distribution of carbides in a sheet; and (c) the temperature-dependence of observed sheet spacing. The prediction of microstructure is important for industry in manufacturing and casting materials. Out of this purpose, the numerical and computational models are therefore proposed to solve this problem by considering the thermodynamic and kinetic aspects of austenite-to-ferrite transformation and carbide precipitation. The experimental data from Honeycombe *et al*. and Ricks and Howell are mainly incorporated in the numerical models. According to the as-received materials, the models are limited to that proposed for vanadium alloyed steels. The basic propositions and the contributions of the proposed models are summarized in Table 2-2.

For the interphase precipitation in vanadium alloyed steels, the modeling work was initiated by Li and Todd. Their model is based on solute balance at the interface. Sophisticated mathematical equations and treatments were used to obtain the ratio of sheet spacing to carbide width by firstly measure the interface velocity with a given sheet spacing. This ratio, in their view points, is independent of transformation temperatures and can be used to calculate the modeled parameters. Therefore, the sheet spacing at different transformation temperatures can be predicted. The calculated results exhibit good agreement with experimental works.

On the contrary, Lagneborg and Zajac (L-Z model) propsed a semi-analytical model by introducing the concepts of superledge and assuming a local equilibrium condition at the interface. The L-Z model is mainly focused on the relation between sheet spacing and transformation temperatures and the effects of carbon and vanadium contents on the sheet spacing was briefly discussed. In fact, their goal was to clarify the effects of diffusion mechanisms of solute (volume or boundary diffusions) and natures of interface (coherent or semi-coherent) on interphase precipitation.

Table 2-2 A summary of the existing models for interphase precipitation in vanadium alloyed steels

	Important assumptions	Contributions	Remarks
Bhadeshia [56]	-	● The minimum height of ledge is given	● The height of superledge has to be larger than the predicted minimum height
Li and Todd [12]	● Vanadium re-distribution between austenite and ferrite and it accumulates at the interface ● The nucleation of carbide does not interfere with interface migration ● Transformation accomplished by advancing small steps, not a superledge ● Vanadium diffuses in ferrite (volume diffusion)	● Ratio of sheet spacing to carbide width can be obtained by measuring the boundary velocity where sheet spacing is known. ● The ratio is independent of transformation temperature	● Ledge mechanism is not highlighted ● Dealt carbide precipitation with the growing ferrite phase ● Sheet spacing, particle spacing, and carbide size can be predicted
Rios [10]	● The stepped interface migrates at a constant velocity and its ledge height equals to the sheet spacing of interphase precipitation ● Vanadium diffuses in pseudophase (volume diffusion)	● Solubilities of solute and carbon are emphasized ● Calculated velocity is half of that calculated by Li and Todd ● The concept of pseudo-phase is also applied.	● Stoichiometric composition of steel ● Followed ledge mechanism ● Predict the variation of sheet spacing with the transformation temperatures
Liu [57]	● Local para-equilibrium condition at the interface ● Nucleation of carbide is accompanied with advancement of interface. ● The ledge height is a constant value	● Consider force balance between pinning force of carbide and transformation driving force. ● Provide the precipitation start time. ● Empirical expression of boundary diffusion is given	● Ledge mechanism is not followed ● The empirical boundary diffusivity of vanadium atom was presented.
Lagneborg and Zajac [13]	● Local equilibrium at the interface ● Interphase precipitation is accomplished by boundary diffusion of vanadium ● Introducing the concept of superledge	● Discussed the diffusion mechanisms and natures of interface ● Revealed the composition-dependence (C, V, and N) of sheet spacing	● The term of superledge was firstly incorporated in model development

The positions of the proposed models are summarized in Table 2-2. Among these models, the predicted sheet spacing in their works generally shows good agreements with experimental data at higher transformation temperatures. Each of them will be examined carefully and the assumptions will be reviewed as follows.

2.3.1 The models for interphase precipitation

(1) The Model of P. Li and J.A. Todd

The model proposed by Li and Todd (the L-T model) is based on the coupling between growth of carbide and ferrite. The precipitate sheet widths, precipitation repeat periods and boundary velocities are formulated. Their final outputs are a ratio of sheet spacing to carbide size.

In the L-T model, the term "pseudo-phase boundary" was introduced in order to apply Zener's solution for plate precipitate growth and the following assumptions were made [58]:

a. the solute concentration is constant and equal to the average concentration of the sheet of interphase-precipitated carbides.
b. mass balance is applied at the interface
c. average solute concentration in ferrite at the interface boundary is constant
d. The motion of interface does not influence the carbide nucleation.
e. The passage of ledge is accomplished by advancing small steps. The row of carbides and the layer of ferrite are stacked layer by layer.

Figure 2-13 highlights the sequences of interphase precipitation in L-T model. As the first row of precipitates formed, the pseudo-phase is generated just ahead of the precipitates (Figure 2-13). The interphase-precipitated carbides are assumed to be small and uniformly distributed along the interface boundary, enabling the growth of precipitates in row to be approximately planar. The precipitates in the first row will grow with time, so does the austenite/ferrite interface boundary. Until the interface boundary moves away, accumulating sufficient solutes for further precipitation, the second cycle of interphase precipitation occurs. It should be kept in mind that the lateral growth of ledge is accomplished by small steps and the growth of carbide with interface motion is highlighted.

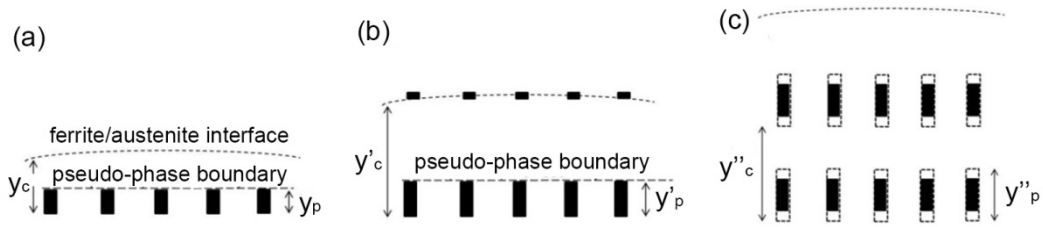

Figure 2-13 Schematic illustration showing the sequences of interphase precipitation in the L-T model. (a) the first row of precipitates nucleate with a size of y_p and generates the pseudo-phase boundary simultaneously; (b) the pseudo-phase boundary advances to the position where has sufficient solutes for further precipitation; the growth of the carbides in the first row is taken into considerations as well; and (c) carbides continue to grow, from the size $y_p^{'}$ to $y_p^{''}$ [12]

Coupling with the experimental work from Honeycombe *et al.*, it has found that the sheet spacing of interphase precipitation and the diffusivity of solute element can be expressed as:

$$y_c^{'} = K_e (D_V)^{1/2} \tag{2-2}$$

where D_V is the diffusivity of vanadium in ferrite. The proportional constant, K_e, is strongly dependent on compositions and austenitization temperatures.

Based on mass balance at the interface, the concentration in front of the advancing pseudo-phase has been expressed as

$$\frac{C^m - C^{mo}}{C^{mp} - C^{mo}} = \frac{1 - erf(y/2\sqrt{Dt})}{1 - erf(s/2)} \tag{2-3}$$

where $y_p = s\sqrt{Dt}$

D = solute diffusivity in ferrite

t = time

C^m = solute concentration in ferrite at position $y(t)$

C^{mo} =initial concentration of solute in ferrite

C^{mp} = concentration of solute in ferrite at the pseudo-phase/ferrite interface assuming to be zero in the present analysis

y_p = forward growth distance of the pseudo-phase

Zener had provided an approximated value for s [58]:

$$s = \frac{\Omega}{\sqrt{1-\Omega}} \tag{2-4}$$

and Li and Todd shows that the parameter Ω is expressed as [9]

$$\Omega = [\frac{1}{2}(\frac{y_c^{'}}{y_p^{'}} - 1) + 1]^{-1} \tag{2-5}$$

After mathematically analysis, the concentration of solute in the pseudo-phase, C^p, and the sheet spacing are derived as follows:

$$C^p = \frac{1}{2}(C^{mo} - C^{mp})(\frac{y_c^{'}}{y_p^{'}} - 1) + C^{mo} \tag{2-6}$$

$$y_c^{''} = y_c^{'} = A\sqrt{Dt_c^{'}} = A(D_o t_c^{'})^{1/2} e^{-\Delta H_V/2RT} \tag{2-7}$$

where $t_c^{'}$ is the interphase precipitate repeat period, and A is given by

$$A = \frac{2-\Omega}{\sqrt{1-\Omega}}$$

(2-8)

Then, the average velocity of interface can be obtained

$$\overline{V_b} = \frac{y_c^{'}}{t_c^{'}} = A\frac{D^{1/2}}{t_c^{'1/2}} = A(t_c^{'})^{-1/2} D_o^{1/2} e^{-\Delta H_V/2RT} \tag{2-9}$$

In addition, the forward growth distance of the pseudo-phase at the instant when a new sheet of nuclei is formed is derived as

$$y_p^{'} = \frac{\Omega}{1-\Omega}\sqrt{Dt_c^{'}} \tag{2-10}$$

Finally, the equation for y_c is shown as

$$y_c = 2\sqrt{Dt}erf^{-1/2}(1-\frac{C^{mc}-C^{mo}}{C^{mp}-C^{mo}}erfc\frac{\Omega}{2\sqrt{1-\Omega}}) \tag{2-11}$$

For now, it has been shown that all the parameters of interests for interphase precipitation have been correlated with composition and position terms. Generally, all the quantities can be classified into two categories:

(a) Measured quantities:

sheet spacing $(y_c^{''})$, particle size $(y_p^{''})$, diffusivity (D), alloy concentration (C^{mo}), and activation energy ΔH_V

(b) Calculated quantities:

sheet repeat period $(t_c^{'})$, solute concentration of pseudophase (C^p), average interphase velocity $(\overline{V_b})$, and critical supersaturation (C^{mc}).

The final purpose of L-T model is to relate the measured quantities to the calculated ones. Because all the calculated quantities are the function of the ratio of sheet spacing to carbide width, $y_c^{'}/y_p^{'}$, and it is independent of transformation temperatures, Li and Todd have suggested the first step is to measure the average interphase boundary velocity where sheet spacing is known. As the diffusivity of vanadium is calculated at a given temperature, the value of A can be obtained from

$$A = (\frac{\overline{V_b}y_c^{'}}{D})^{1/2} = \frac{2-\Omega}{\sqrt{1-\Omega}} \tag{2-12}$$

where $\Omega = [\frac{1}{2}(\frac{y_c^{'}}{y_p^{'}}-1)+1]^{-1}$, a quantity related by the ratio $y_c^{'}/y_p^{'}$

Because it has been approved that $y_c^{'} = y_c^{''}$, the ratio of $y_c^{'}/y_p^{'}$ can be determined. By measuring the interphase boundary velocity and sheet spacing, and with the knowledge of diffusivity of solutes, the value $y_p^{'}$ can be obtained. Finally $y_p^{''}$ is calculated from

$$y_p^{'} = \frac{y_c^{''} y_p^{''}}{2y_c^{''} - y_p^{''}} \tag{2-13}$$

In summary, the L-T model tries to relate all the interested parameters by using the ratio $y_c^{'}/y_p^{'}$, which is simply obtained by measuring the interphase boundary velocity and sheet spacing. It firstly provided a systematically model describing interphase precipitation. It should be noted that the calculations in L-T model yield a ratio of $y_c^{'}/y_p^{'}$, instead of giving a direct value. The calculated results show great consistencies with the microscopic data in other published papers.

However, some of their propositions deviate from real physical situations and are doubted by Rios [10] and Liu [57]. In L-T model, the sheet structure of ferrite and carbide develop one after another. It implies that the ferrite ledge height is not necessarily equal to the sheet spacing of carbide. However, in fact, the ferrite ledges are observed to move as a “train”, instead of individual layer. Furthermore, L-T model implies vanadium is enriched in austenite in front of the interface and re-distributed between ferrite and austenite during the motion of interface. Actually, the re-distribution of vanadium solute is expected to occur only at slow transformation rates (high transformation temperatures). In addition, vanadium diffusion in ferrite is about 3 times order of magnitude faster than in austenite; vanadium accumulated at the interface is expected to transfer into ferrite. Therefore, the enrichment in austenite is difficult to happen. These weaknesses have been discussed by Rios and Liu.

(2) The Model Proposed by P.R. Rios

Rios proposed an alternative to the L-T model. In that model, the vanadium volume diffusion is also considered but the ferrite ledge height is supposed to be in equal to the sheet spacing of interphase precipitation. The assumptions in Rios’ model

are shown as follows:

a. The ledge velocity is constant
b. The carbides form as a continuous layer in the pseudo-phase region which is indicated as the shaded area in Figure 2-14.

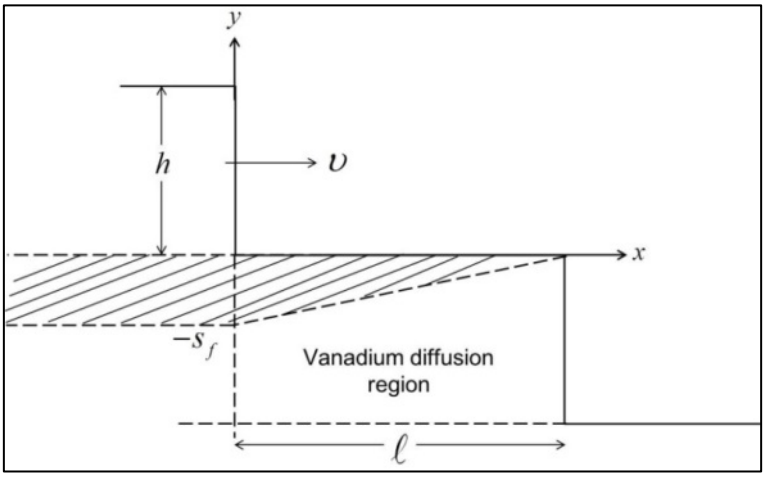

Figure 2-14 Schematic illustration showing the Rios' model. The pseudo-phase is indicated as a shaded area. In the vanadium diffusion region, the pseudo-phase boundary changes linearly from the previous ledge riser to the latter one, with a final thickness, s_f.

c. The thickness of pseudo-phase increases linearly from the advancing riser to the trailing one and finally reaches its final thickness, s_f.
d. Based on stoichiometric composition, the carbon content of austenite remains constant, it means that the carbon rejected by ferrite growth goes into the carbides directly.
e. The vanadium is limited to diffuse into carbide between the region $0 < x < l$ and $-h < y < 0$. The growth of pseudo-phase is controlled by vanadium diffusion in ferrite.
f. The boundary conditions of vanadium concentration are: (1) at $x = l$ along $-y$ direction, $C_v = C_v^o$; (2) at ferrite/pseudo-phase boundary, $C_v = 0$; (3) C_v in austenite remains constant and equals to C_v^o. The three boundary conditions will be further used in the following calculations.

Using the imaginary coordinates in Figure 2-14, the vanadium concentration in ferrite can be approximated in a plane by

$$C_V(x,y) = A + Bx + Cy \tag{2-14}$$

The goal now turns into finding the exact values of constants *A*, *B*, and *C*. By applying the boundary conditions mentioned in assumption f. Two equations can be written as

$$C_V^o = -\frac{\int_0^{-h} C_V(\ell, y)dy}{h} \tag{2-15}$$

$$\frac{\int_0^{\ell} C_V(x,0)dx}{\ell} = 0 \tag{2-16}$$

Furthermore, the average vanadium concentration in ferrite within the limited region is assumed to be equal to $C_V^o / 2$ where the latter one is given by

$$\frac{C_V^o}{2} = -\frac{\int_0^{-h}\int_0^{\ell} C_V(x,y)dxdy}{\ell h} \tag{2-17}$$

Using the above Equations, the constants, A, B, and C are solved by the final expression of vanadium concentration in the limited diffusion region becomes

$$C_V(x,y) = C_V^o(-\frac{1}{2} + \frac{x}{\ell} - \frac{y}{h}) \tag{2-18}$$

From mass balance under steady-state consideration, the vanadium entering the ferrite through ledge riser is equal to that entering the growing pseudo-phase

$$\ell[\frac{\partial C_V(x,y)}{\partial y}]_{y=0} = -h[\frac{\partial C_V(x,y)}{\partial x}]_{x=\ell} \tag{2-19}$$

Equations (2-18) and (2-19) yield a useful relation which is $h = \ell$.

The average pseudo-phase boundary velocity can be calculated by taking the flux of vanadium at position y = 0

$$\upsilon_p(0-kC_V^p) = -D[\frac{\partial C_V(x,y)}{\partial y}]_{y=0} \tag{2-20}$$

where D is the vanadium diffusivity in ferrite, C_V^p is vanadium composition in carbide, kC_V^p is the vanadium concentration in pseudo-phase, and k is a constant. Using equation (2-18), the average pseudo-phase boundary velocity becomes

$$\upsilon_p = -\frac{fD}{kh} \tag{2-21}$$

where $f = C_V^o / C_V^p$, the volume fraction of carbides.

The ledge velocity is determined as follows. When the ledge riser moves from $x = 0$ to $x = h$ (the ledge spacing has been shown to be equal to ledge height) at given time τ, it means that the pseudo-phase boundary moves its average position from $y = -s_f/2$ to $y = -s_f$. Therefore, the following relation between ledge and pseudo-phase velocities can be written as (the ledge and pseudo-phase velocities are assumed to be independent of time)

$$\tau = -\frac{s_f}{2\upsilon_p} = \frac{h}{\upsilon} \tag{2-22}$$

Assuming all the vanadium entering the ledge riser goes into pseudo-phase to form carbide, $s_f(kC_V^p) = hC_V^o$ or $f = (ks_f)/h$, a simplified expression for ledge velocity can be obtained by:

$$\upsilon = \frac{2D}{h} \tag{2-23}$$

Equation 2-23 shows that the ledge velocity is inversely proportional to ledge height but it does not demonstrate how the transformation temperatures and carbide volume fraction affect ledge height clearly. From equations 2-21 to 2-23, the three parameters, ks_f, h, and τ, can be related as

$$K = \frac{ks_f}{D^{1/2}} = f(2\tau)^{1/2}$$
$$\frac{h}{D^{1/2}} = (2\tau)^{1/2} \tag{2-24}$$

Equation 2-24 yields another relation describing the ledge height with K

$$h = K\frac{D^{1/2}}{f} \tag{2-25}$$

The value of K is defined as a model parameter. Great efforts were made in Rios model to determine its value by using a phenomenological analysis from other researches. Obviously, as we plotting the ledge height, h, against $D^{1/2}/f$, a straight line can be obtained. The slope of this line gives K. However, by using equation 2-25, the results have greater deviations with the experimental data which were obtained at higher transformation temperatures and lower alloy contents. Rios proposed that such deviations were associated with the ratio of total solutes, I_o, to the solutes which are insoluble in austenite, I_{in}. In order to correct such a deviation, Rios introduced solubility product into K. Then, K is re-written as

$$K = K_s(\frac{I_o}{I_{in}}) \tag{2-26}$$

where

$$\frac{I_o}{I_{in}} = \frac{C_o}{C_o - C_s} \tag{2-27}$$

Using the solubility product of VC in austenite, the C_s can be expressed as

$$C_s = \frac{K_{VC}}{C_V^o} \tag{2-28}$$

Then, equation 2-25 becomes

$$h = K_s (\frac{I_o}{I_{in}}) \frac{D^{1/2}}{f} \tag{2-29}$$

Replacing equation 2-29 into 2-23, the ledge velocity becomes

$$\upsilon = (\frac{2}{K_s})(\frac{I_{in}}{I_o}) f D^{1/2} \tag{2-30}$$

Equations 2-29 and 2-30 couple with the concept of super-saturation in term of carbon solubility ratio, I_{in}/I_o, with the parameters of interests. By referring to equation 2-29, a greater ratio (I_o/I_{in}, super-saturation is low) will generate a wider sheet spacing of interphase precipitation. The physical interpretation is that as the degree of super-saturation is decreased, it would result in reducing the nucleation rate of carbide as well, forming a coarser and wider spaced carbide distribution. Of course, a smaller ratio of (I_o/I_{in}) contributes to an opposite effect. The most advantageous part of equations 2-29 and 2-30 is that only one adjustable model parameter, K_s, is used for calculations. In addition, equation 2-29 has been established to be coupled with the relationships developed in the other work for calculating carbide size and volume fraction [59]. The sheet spacing calculated by equation 2-29 exhibits a better agreement (compared to equation 2-25 with the experimental data obtained by Batte and Honeycombe [37] and Balliger and Honeycombe [60].

The ledge velocity calculated by equation 2-30 represents the velocity of ledge riser during its migration. It indicates that the ledge velocity decreases with transformation temperatures, carbide volume fraction, and solubility of carbide. However, compared to the average velocity calculated by Li and Todd, the results obtained by Rios present a smaller value, about half of that obtained by Li and Todd. As mentioned previously, the velocity calculated by Li and Todd is the overall interface velocity which advancing direction is normal to the sheet of carbides. Carbide precipitation on the terrace plane and the passage of ferrite ledge happen one after another and the ledge height does not have to be equal to sheet spacing of interphase precipitation. That is, the height of ferrite ledge is taken as an average

value, so does the interface velocity. However, in Rios model, the velocity calculated by equation 2-30 is for ledge riser only. He proposed that the ledge mechanism of austenite-to-ferrite transformation is accomplished by the passage of ferrite ledge which its height is equal to the sheet spacing of interphase precipitation, and the ledge riser advances with a constant velocity. It can be expected that the ledge height in Rios model is greater than that in L-T model and requires a longer time to develop, leading to a slower velocity than that calculated by Li and Todd.

(3) The Model Proposed by W.J. Liu

In addition to Rios, the propositions of L-T model were also challenged by Liu through different points of views. He pointed out that part of the assumptions made by Li and Todd were deviated from real thermodynamic and kinetic conditions. The arguments are summarized as follows:

a. In L-T model, vanadium solute is assumed to re-distribute with the advancing interface. Liu pointed out it is unreasonable. Because generally the activation energy of substitutional element is greater than that of interstitial element, the vanadium re-distribution is expected to operate at a higher transformation temperature. However, the experimental data coupled with the L-T model were obtained at the transformation temperatures around 700 ^{o}C. Liu argued that the vanadium atoms are difficult to be driven at these transformation temperatures.
b. Li and Todd proposed that the vanadium would accumulate in front of interface. However, the diffusivity of vanadium in ferrite is three times order of magnitude faster than that in austenite. It means that the vanadium solute would diffuse into ferrite more rapidly. Accumulation of substitutional solute at the interface is almost impossible to happen
c. Carbide nucleation on the interface and its pinning effect were not involved in L-T model. It implies that the precipitation of VC does not interfere with interface motion. However, it was recognized that interphase precipitation could effectively retard the interface motion and have influences on the growth kinetics of allotriomorphic ferrite. Liu had actually provided detailed derivations to against this point.

Based on these arguments, Liu proposed a computational model to modify the

L-T model. The ferrite/austenite interface was supposed to be under para-equilibrium condition and a force balance between pinning force exerted from carbide, F_p, and transformation driving force, F_d, was supposed. The latter force affects directly interface velocity, which is dependent on the ease of carbon diffusion from the interface into austenite and gradually decreases because of carbon enrichment in austenite. The reduced velocity stimulates carbide precipitation, at the same time, increasing the pinning force, F_p. Until $F_p = F_d$, the interface is pinned by carbides and becomes stationary but the carbon continuously diffuses from the interface into austenite. This process will increase F_d again. On the other hand, the rate of increment of F_p will become slower because the solute concentration decreases as carbide precipitation. In the latter stage, F_d will take over F_d again, unpinning from the carbides. The evolutions of F_p and F_d with time are schematically illustrated in Figure 2-15. As a result, the first issue of Liu's model is to determine the values of F_p and F_d, and this is obviously dependent on the carbon diffusion in austenite.

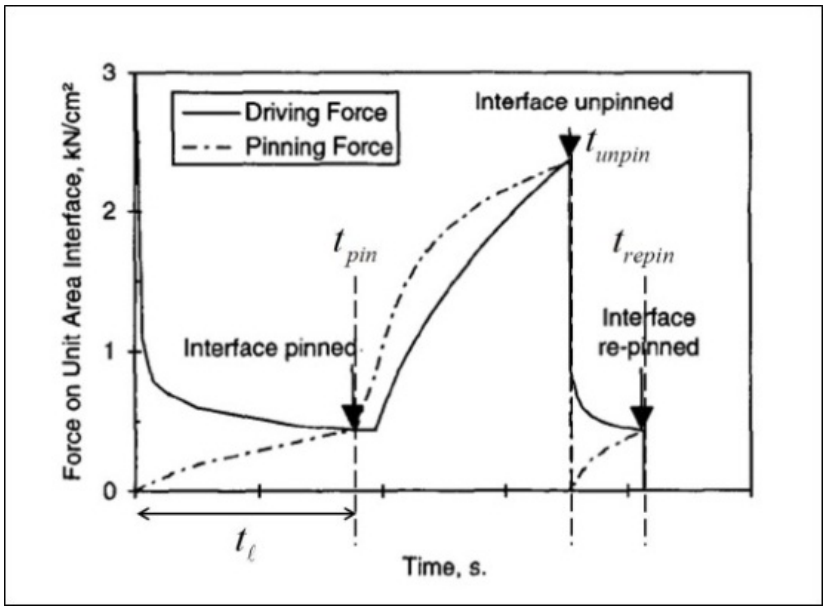

Figure 2-15 Schematic illustration showing the model proposed by Liu. The important time parameters are indicated in this figure. In his model, the process of interphase precipitation is a repeated force balance between the driving force, F_d, and the pinning force, F_p [57]

In the beginning of calculations, carbon diffusion in austenite should be first introduced because it determines the interface velocity and in calculating the sheet spacing of interphase precipitation. Using one-dimensional version of Fick's second law and considering the composition-dependence of carbon diffusivity, the resulting

differential equation is

$$\frac{\partial c}{\partial t} = D_c \frac{\partial^2 c}{\partial x^2} + \frac{\partial D_c}{\partial c}(\frac{\partial c}{\partial x})^2 + v \frac{(d_a/2) - x}{(d_a/2) - w_f} \frac{\partial c}{\partial x} \tag{2-31}$$

where D_c is the diffusion coefficient of carbon in austenite, d_a is the austenite grain diameter, w_f is the width of ferrite grain, x is the dimensional coordinate, c is the volume concentration of carbon in austenite, and v is the interface velocity. With the boundary conditions

$$\begin{aligned} &(c^\gamma - c^\alpha)v = D_c \left.\frac{\partial c}{\partial x}\right|_i \\ &c = c^\gamma \Big|_{x=w_f} \end{aligned} \tag{2-32}$$

where c^γ and c^α are the para-equilibrium carbon levels in austenite and ferrite, respectively, and the subscript i stands for interface. The interface velocity can be obtained.

Then, the sheet spacing of interphase precipitation, λ, can be obtained by integrating the velocity from the t_{unpin} to t_{repin}.

$$\lambda = \int_{t_{unpin}}^{t_{repin}} v dt \tag{2-33}$$

Replacing the obtained interface velocity into the equation 2-31, the carbon concentration at the interface and composition-dependence carbon diffusivity in austenite can be derived as

$$\begin{aligned} &D_c = \frac{D_c^o}{[1 - 2Y_V(1 - 0.088\exp(67.4kJ/RT))]} \\ &D_c^o = D^o(1 - BY_c)\frac{\psi}{\psi_M}(\frac{BY_c}{1 - BY_c} + 1 + Y_c \frac{d\ln(\psi/\psi_M)}{dY_c}) \end{aligned} \tag{2-34}$$

$$c = c^o + (c^\gamma - c^o) erfc(\frac{x}{2\sqrt{D_c t}}) \tag{2-35}$$

where Y_c is the site fraction of carbon in its corresponding sub-lattice, B is a carbon site blocking parameter, ψ and ψ_M are the activity coefficients of carbon in austenite and of the activate complex of carbon, respectively.

The thermodynamic at the interface should be considered as well. Two free energy terms are introduced in Liu's calculations, ΔG_n and ΔG^*. From classical nucleation theory, the total free energy change accompanied with the formation of a carbide nucleus on the interface can be expressed as

$$\Delta G_n = V(\Delta G_{chem} + \Delta G_\varepsilon) + S\sigma - E_{\gamma\alpha} \tag{2-36}$$

where V and S are the volume and surface area of the embryo, ΔG_{chem} and ΔG_ε are the chemical driving force and coherency strain energy of forming an unit volume embryo, respectively, , σ is the embryo/matrix interface energy, and $E_{\gamma\alpha}$ is the energy released from the interface nucleation site. The terms of V, $S\sigma$, and $E_{\gamma\alpha}$ are estimated by

$$\begin{aligned} V &= 4\rho r^3 \\ S\sigma &= (8\rho r^2 + 4r^2)\sigma_{p\alpha} + 4r^2\sigma_{p\gamma} \\ E_{\gamma\alpha} &= 4r^2\sigma_{\gamma\alpha} \end{aligned} \tag{2-37}$$

where $\rho = h/r$ is the aspect ratio of carbide. The terms, $\sigma_{p\alpha}$, $\sigma_{p\gamma}$, and $\sigma_{\gamma\alpha}$, represent as the interfacial energies at precipitate/ferrite, precipitate/austenite, and austenite/ferrite interface, respectively. From equations 2-36 and 2-37, the critical nucleation energy can be obtained. The detailed mathematical treatments will not be shown here but he final derivative results are presented as follows:

$$\Delta G^* = \frac{16\sigma_{p\alpha}^2(\sigma_{p\alpha} + \sigma_{p\gamma} - \sigma_{\gamma\alpha})}{\Delta G_{chem} + \Delta G_\varepsilon} \tag{2-38}$$

$$\Delta G_{chem} = \frac{RT}{2\Omega_{MI}}[2.3\log[M][I] + (1+y)\ln(\frac{A_{Fe}}{100}) - \ln(A_M A_I^y) - \ln[X_M^\alpha][X_I^\alpha]^y] \tag{2-39}$$

$$\Delta G_{\varepsilon} = \frac{2}{3}\frac{\mu_{\alpha}(\Delta^{*})^{2}K}{[K + \frac{(1-K)K_{\alpha}}{K_{MI}}]} \tag{2-40}$$

$$\Delta^{*} = (1 - C_{\ell})\frac{(a_{MI}^{3}/2) - a_{\alpha}^{3}}{a_{\alpha}^{3}} \tag{2-41}$$

where Ω_{MI} is the molar volume of *MI*, *log[M][I]* is the solubility product of carbide in ferrite, *y* is the interstitial/substitution ratio in the *MI* phase, A_{Fe}, A_M, and A_I are atom weights of *Fe*, *M*, and *I*, respectively. The terms X_M^{α} and X_I^{α} are the mole fraction of *M* and *I* in ferrite. μ_{α} is the shear modulus of ferrite. K, K_{α}, and K_{MI} are all elastic parameters, and Δ^{*} is the effective cubic dilatation. So far, the kinetics and thermodynamics parameters have been constructed for further F_p and F_d calculations.

The nucleation rate of carbide is required to determine F_p. Ashby had shown that the maximum pinning pressure exerted on such an interface is expressed as

$$F_p = \frac{2r\sigma_{\gamma\alpha}}{s_h^2 - r^2} \tag{2-42}$$

where s_h is the half-interparticle spacing which is calculated by

$$s_h = \frac{1}{\sqrt{N}} \tag{2-43}$$

where *N* is the precipitate density, being a function of nucleation rate, *J*, as.

$$N = \int_0^{t_{\ell}} J \exp(\frac{-\tau}{t})dt \tag{2-44}$$

where τ is the incubation time of carbide. The integral time interval is from zero to the lifetime of the phase boundary, t_{ℓ} (see Figure 2-15), which can be determined by

$$t_\ell = \frac{w}{v} \tag{2-45}$$

where w is the thickness of an incoherent interface (or height of ledge on coherent interface) and v is the interface velocity in the direction normal to the interface which can be calculated by equation 2-32.

Using the classical nucleation theory, J and incubation time, τ, are written as

$$J = Z\beta^* N_s \exp(\frac{-\Delta G^*}{kT}) \tag{2-46}$$

$$\tau = \frac{-1}{\frac{\beta^*}{kT}\frac{\partial^2 \Delta G_n}{\partial n^2}\bigg|_{n^*}} \tag{2-47}$$

$$Z = \sqrt{\frac{-1}{2\pi kT}\frac{\partial^2 \Delta G_n}{\partial n^2}\bigg|_{n^*}} \tag{2-48}$$

$$\beta^* = \frac{48 r^* D_M^i Y_M}{a_\alpha^3} \tag{2-49}$$

where Z is the Zeldovich non-equilibrium factor, β^* is the rate at which atoms are added to the critical nucleus, and N_s is the number of nucleation sites per unit area at the interface. The energy terms, ΔG^* and ΔG_n, are the energy of forming a critical nucleus and an embryo that contains n atom pairs, respectively. The n^* is the atom pair number in the critical nucleus. In equation 2-49, r^* is the critical radius of the nucleus, D_M^i is the diffusion coefficient of the metal element along the interface, Y_M is the site fraction of the metal solute in ferrite, and a_α is the lattice parameter of ferrite. The value of N_s is defined to be equal to number of lattice sites on $\begin{pmatrix}1 & 0 & 0\end{pmatrix}$ ferrite plane

$$N_s = \frac{\sqrt{2}}{a_\alpha^2} \tag{2-50}$$

For the driving force, F_d, it is defined as the difference of iron and substitutional atoms between ferrite and austenite phases at the interface under a para-equilibrium

condition, which is expressed as

$$F_d = \frac{(\overline{G_i^\alpha} - \overline{G_i^\gamma})}{\Omega_i} \cong \frac{(\overline{G_i^\alpha} - \overline{G_i^\gamma})}{\Omega_\alpha} \tag{2-51}$$

where $\overline{G_i^\alpha}$ and $\overline{G_i^\gamma}$ are the chemical potentials of rion and substitutional atoms in ferrite and austenite, respectively, at the interface. Ω_i is the molar volume of the interface and assumed to be that of ferrite matrix, Ω_α. A simplification is made by assuming $\overline{G_i^\alpha}$ is equal to the chemical potential of Fe and substitutional atoms in the para-equilibrium austenite phase, $\overline{G_{PE}^\gamma}$, and is time-independent. The two-sublattice model proposed by Hillert was applied to calculate $\overline{G_{PE}^\gamma}$ and $\overline{G_i^\gamma}$. The detailed algorithms are complicated and have been presented in elsewhere. Generally, $\overline{G_{PE}^\gamma}$ can be obtained by initially determining the para-equilibrium carbon level via given thermodynamic database. However, the determination of $\overline{G_i^\gamma}$ is associated with giving the carbon level in austenite at the interface is more difficult to be operated. From Liu's propositions, the needed carbon level can be solved by using Fick's second law for carbon diffusion in austenite during the immobilization period under the boundary condition

$$\frac{\partial c}{\partial x_i} = 0 \tag{2-52}$$

The carbon concentration in austenite at a pinned interface was calculated by the same approach.

In addition to the force balance at the interface, the carbide growth is of interests in Liu's model. However, an average carbide size, instead to calculate individual one, is presented. The mean particle size can be obtained by numerical integration

$$\bar{r} = \frac{1}{N}\sum_{i=1}^{N} r_i^* + \int_0^t (\overline{\frac{dr}{dt}})dt \tag{2-53}$$

where $\left(\overline{dr/dt}\right)$ is the mean particle growth rate. According to the conventional grain growth theory, the mean particle growth rate can be written as

$$(\frac{\overline{dr}}{dt}) = \frac{-D_M^i}{c_M^p - c_M^e} \frac{\partial c_M}{\partial x}\bigg|_i \tag{2-54}$$

where c_M^p is a constant for a given type of MI component. On the contrary, the quantity c_M^e is a function of temperature and particle size can be estimated as

$$c_M^e = \frac{1}{\Omega_{MI}}[\exp(\frac{\Delta G_{MI}}{RT} + \frac{4\sigma_{p\alpha}\Omega_{MI}}{RT\bar{r}}) - X_I^\alpha] \tag{2-55}$$

where ΔG_{MI} is the Gibbs energy of formation of MI from ferrite with infinite dilution as the reference state, and Ω_{MI} is the molar volume of *MI*. $(\partial c_M/\partial x)\big|_i$ is the mean concentration gradient of *M* around each precipitate along the interface. c_M^p and c_M^e are the equilibrium volume concentrations of the metal element in precipitate and at the particle/ferrite interface, respectively. In Liu's paper, the final expression of mean carbide size is given as

$$\bar{r} = \sqrt[3]{\frac{(s_h^2 \lambda c_M^o)}{\rho c_M^p}} \tag{2-56}$$

where c_M^o is the overall volume concentration of *M* in the steel and ρ is set to be 3/5 in the present analysis.

It can be expected that as the carbides start to nucleate and grow on the interface, the consumption of solute element will change the boundary condition of interface and further influence the precipitation nucleation and growth in the following stages. In order to solve this problem, Liu considered three solute flows of solute element at the interface: J_p, J_a, and J_d which correspond to atoms transferred from the interface into carbide, atoms transferred from austenite into ferrite, and atoms transferred from

austenite to the interface, respectively, and expressed as

$$J_p = -4\rho c_M^p (3N\overline{r^2}\ \frac{dr}{dt} + \overline{r^3}\frac{dN}{dt})$$
$$J_a = \rho(c_M^\gamma - \overline{c_M})\frac{d\overline{r}}{dt} \tag{2-57}$$
$$J_d = D_M^\gamma \left.\frac{\partial c_M^\gamma}{\partial x}\right|_i \cong D_M^\gamma \frac{(c_M^o - \overline{c_M})}{L_a}$$

where c_M^γ is the volume concentration of M in austenite, $\overline{c_M}$ is the mean M concentration in ferrite at the interface, D_M^γ is the diffusion coefficient of M in austenite, and L_a is the length of the solute diluted zone in front of the interface in austenite. By using the solute flows presented in equation 2-57, the mean M concentration at the interface at a given time is obtained

$$\frac{d\overline{c_M}}{dt} = \frac{(J_p + J_a + J_d)}{w} \tag{2-58}$$

Equation 2-58 gives the time evolution of the solute concentration. The solute concentration in front of interface influences directly the nucleation rate of carbide J, that is, the pinning force F_p. Thus, by coupling with equation 2-58, the evolution of pinning force with time can be revealed. Furthermore, the other application of equation 2-58 is to modify the growth rate equation which is shown in equation 2-54; the differential term in equation 2-54 can now be re-written as

$$\left.\frac{\partial c_M}{\partial x}\right|_i \cong \frac{(\overline{c_M} - c_M^e)}{L} \tag{2-59}$$

where L is the mean radius of the solute dilution zone around each particle at the interface which is expressed as

$$L = \sqrt{\frac{3\left(c_M^o - \overline{c_M}\right)}{(c_M^o - c_M^e)\pi N}} \tag{2-60}$$

Now, the derived all equations are used to simulation. The final output data of Liu's model are sheet spacing, λ , carbide size, *d*, and the start time of interphase precipitation, P_s. It is noted that these equations still contain three unknown parameters for simulations. They are: (1) *w*, the thickness of incoherent boundary (or the ledge height of a semi-coherent interface; (2) D_M^i , the diffusivity of solute at the interface, and (3) C_ℓ , the coherence loss parameter of VC nucleus. These parameters are calculated repeatly until the designed program find out their best fitting values. The final best fitted results are shown as follows:

a. $w = 2a_\alpha$ and is almost a constant independent of transformation temperatures

b. $D_M^i = 11464.4\exp(\frac{-272.4kJ}{RT})$ [cm^2/s] (2-61)

For the coherence loss parameter, it is assumed to be associated from the inaccuracies and incompleteness of the thermodynamic database which is used in calculations. An additional term, ΔG_c, related to this correction is introduced. Then, the coherence loss parameter can be estimated by

$$\begin{aligned}(1-C_\ell)^2 - \Delta G_c &= -1.40 + 5.88\times10^{-3}T - 3.94\times10^{-6}T^2 \\ \Delta G_c &= -0.371 - (0.0419 - 0.0007T)[V] - 0.557[V]^2 + 0.193[V]^3\end{aligned} \quad (2\text{-}62)$$

It shows that in addition to *w*, D_M^i and C_ℓ are dependent on temperatures. It is noted that the activation energy of solute to diffuse at interface in the present study (272.4 kJ) is larger than that in ferrite matrix (239.3 kJ). This result is obviously non intuitive. The solutes are expected to diffuse along interface boundary more efficiently than in well-packed matrix. Liu had provided his view points to interpret such a deviation. However, his explanation remain unpersuasive and not so clear.

In summary, Liu's model provided another approach to set up a computational model of interphase precipitation in vanadium steels. His model modified parts of arguments of L-T model and the simulated results presented good agreements with

experimental data. The most important part of Liu's model is the precipitation start time, P_s, were introduced. The values of P_s were checked via the *TTT* curves of given steels and found that the P_s generally started after the transformation-start times but the gap between P_s and transformation-start time became smaller as the content of vanadium increased. However, the availability of his model checked by this way seems inappropriately because the experimental data which coupled with his modeling works did not have the same carbon contents. As we know, the final shape of a *TTT* curve is determined by the nucleation and growth of ferrite in a austenite-to-ferrite transformation and this reaction is strongly dependent on the carbon diffusion from ferrite into austenite. Therefore, the gap between transformation-start time and P_s could not be simply interpreted by the amount of vanadium content in a given material even though it is expected to have effects on precipitation which is going to retard the advancement of interface in the following process.

In addition, the ledge mechanism of interphase precipitation, which is a key mechanistic issue in interphase precipitation, was not greatly emphasized in Liu's model. Indeed, the thickness of an incoherent boundary (or the height of ledge), w, was defined as a fitting parameter and showed to be independent of transformation temperatures. It is claimed that value of w is approximately to be $2a_\alpha$ and independent of transformation temperatures. However, this is obviously far beyond the real case. It has been shown that the ledge height is a function of transformation temperatures. Bhadeshia [56] had actually derived a simple equation to predict the minimum ledge height which is required for ledge mechanism of austenite-to-ferrite transformation. It had argued that as the ledge height is smaller than this critical value, the ledge is difficult to form at the interface. The required minimum height of ledge for ledge mechanism is generally ten or hundred times than the lattice parameter of ferrite and is dependent on nucleation energy of ferrite nucleus.

In Liu's model, carbide precipitation occurs during the lifetime of interface boundary. The number of carbide density increases as the time increases, finally making the interface velocity to become zero (at t_{pin}). It means that the carbide precipitates simultaneously with the advancement of interface until this interface is totally pinned by carbides. This proposition is quietly different from the models proposed by other researchers. In general, interphase precipitation is thought to occur when the solute concentration ahead of the interface reaches a critical value for

nucleation. The accumulation of solute is accompanied with the motion of interface, implying that there are no carbides to form during the accumulation stage. Indeed, if the carbide precipitation occurs with the advancing interface, the formation of carbide would be expected to consume large amount of the carbon ahead of interface. It will change the boundary conditions in determining interface velocity; therefore, the interface velocity would not decrease continuously until it is pinned by the carbides. The interface should be treated as a new one after every carbide nucleation step within the lifetime. Actually, the role of carbon in Liu's model is only considered as to diffuse from the interface into austenite matrix. The carbon consumed by the formation of carbide is not well-addressed. However, it is the main proposition of classical interphase precipitation.

(4) The Model Proposed of R. Lagneborg and S. Zajac

In recent years, Lagneborg and Zajac proposed a semi-analytical model by using vanadium alloyed steels [13]. It concerned with the composition-dependence (C, N, and V) and temperature-dependence on sheet spacing of interphase precipitation by considering boundary diffusion of solute atoms. The equations they derived were claimed to be the general case, independent of the natures of interface. Compared to the model addressed previously, the L-Z model seems more analytical and the concept of superledge was introduced. In addition, the effects of diffusion path and nature of interface were discussed.

The first issue in L-Z model is to clarify the exact diffusion mechanism of solute atoms of interphase precipitation. Both volume and boundary diffusions of solute atoms were discussed and compared to each other. Their works showed that the sheet spacing predicted by volume diffusion of solute atom would be finer than that from experimental data, and concluded that interphase precipitation should be accomplished by boundary diffusion of solute atoms.

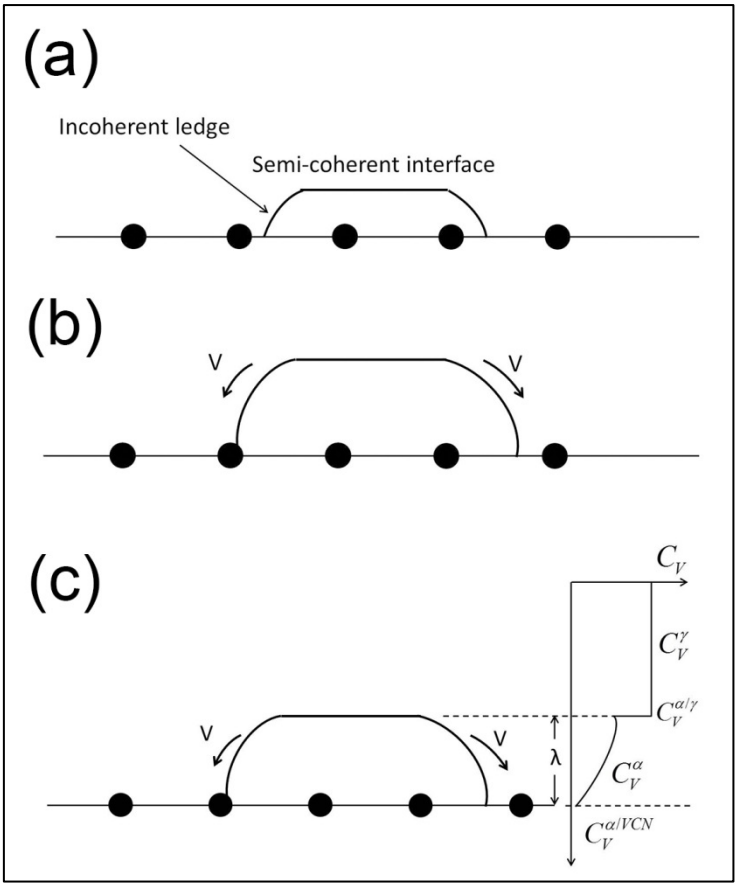

Figure 2-16 Interphase precipitation on a semi-coherent interface in L-Z model. (a) a ledge developed on the interface; (b) the ledge expands laterally and gradually increases its height; and (c) another precipitation process occurs on the interface again as the ledge reaching a critical height. The corresponding concentration profile is presented. [13]

As the diffusion mechanism is determined, they further extended their work to understand how the natures of interface (semi-coherent or incoherent) affect the sheet spacing of interphase precipitation. Figure 2-16 shows the L-Z model of interphase precipitation on a semi-coherent interface. Because diffusion of solute is expected to be less efficient on a semi-coherent interface, the diffusion of V is restricted to occur in one direction of the superledge, from the foremost part of the ledge to the precipitates in the previous sheet. Indeed, the diffusion of solute on the semi-coherent interface was neglected in L-Z model. The carbides precipitate on a semi-coherent interface would have a limited growth rate as well. Because there is only one diffusion path and the advance of the superledge is controlled by lateral transfer of carbon (the gradient is normal to the precipitate sheet), the planar growth of ferrite was applied to calculate the growth rate of the superledge in this case.

Assuming a local equilibrium condition exists at the interface, the planar growth

rate of ferrite had been shown to be

$$S^2 = D_c^{\gamma} \frac{(c_c^{\gamma/\alpha} - c_c^{\gamma/\infty})^2}{(c_c^{\gamma/\alpha} - c_c^{\alpha})(c_c^{\gamma/\infty} - c_c^{\alpha})} t \tag{2-63}$$

where S is the distance from the point of α nucleation to the location of the interface at time t. By differentiating equation 2-63 with t, it yields

$$S = \frac{K_1}{2v} \tag{2-64}$$

where K_1 is the proportionality factor related to the compositions, and v is the velocity of interface. Equation 2-64 will be widely used to calculate the sheet spacing at different transformation temperatures. The required composition parameters in equation 2-63 can be programmed via Thermo-Calc database.

The composition profile presented in Figure 2-16(c) shows the vanadium gradient at the interface. It can be mathematically expressed as

$$\frac{c_V^{\alpha} - c_V^{o}}{c_V^{\alpha/VCN} - c_V^{o}} = \frac{\cosh(x\sqrt{a}/2\lambda)}{\cosh(\sqrt{a}/2)}, \text{ where } a = \frac{4v\lambda^2}{(D\delta)^{boundary}} \tag{2-65}$$

at x = 0, equation 2-65 gives the vanadium content of ferrite in the upper end of the superledge. The equation becomes

$$\frac{c_V^{o} - c_V^{\alpha/\gamma^*}}{c_V^{o} - c_V^{\alpha/VCN}} = \frac{1}{\cosh\sqrt{a}/2} \tag{2-66}$$

where c_V^{α/γ^*} is the critical concentration of vanadium content for carbide nucleation. As a given velocity of interface using equation 2-64, equation 2-66 shows the relation between the critical solute concentration for carbide precipitation and superledge height can be calculated. The procedures to obtain required parameters are summarized as follows:

a. *Compositions of different positions at the interface*

The equilibrium composition could be obtained via Thermo-Calc software, except for c_V^{α/γ^*}, which is the minimum vanadium content for carbide nucleation.

b. *Interface velocity*

It can be calculated indirectly via selecting *S* arbitrary.

c. *Diffusion coefficient of solute at the boundary*

Because such a parameter is very deficient, it is provided approximately by multiplying the boundary diffusion of Fe by a factor of 8 at given temperatures.

The occurrence of interphase precipitation on an incoherent interface possesses a different mechanism. Compared to the semi-coherent interface, the incoherent interface is more curved, acting as another efficient diffusion path for solute atoms. The model for an incoherent interface is shown in Figure 2-17.

At the initial stages, as shown from Figure 2-17(a) to Figure 2-17(c), they are similar to the case of a semi-coherent interface. When the new precipitate forms, the ledge expands laterally accompanied with vanadium diffusion along the superledge (Figure 2-17(d)), generating the concentration profile of vanadium. The maximum vanadium concentration is assumed to be *always* located at the middle of superledge boundary, thus, the new carbide forms initially at these sites. Furthermore, because diffusion of solute atoms on an incoherent interface is possible (segment *de* in Figure 2-17(d)), it will lead to further precipitation at later stages (Figure 2-17(e)). In order to distinguish the carbide forms at different stage, the carbide forming at the middle of superledge boundary (maximum of vanadium content) is called primary precipitates; the carbide precipitating at other position of the incoherent interface, on the contrary, is called secondary precipitation. The curved interface would lead to the interphase precipitation with irregular spacing. From the view points of the authors, would be smoothened due to particle growth affected by the surface-tension forces of the corrugated sheet.

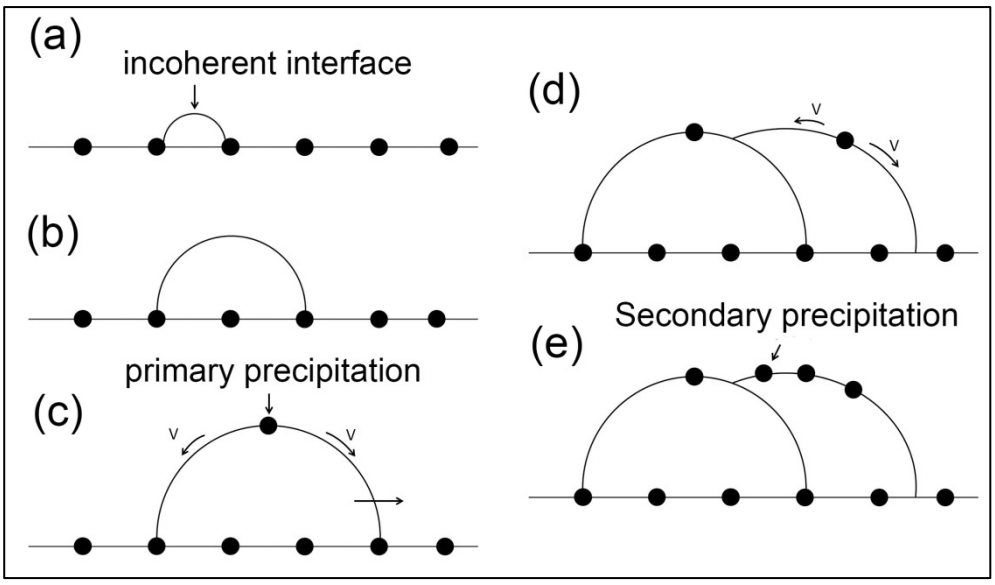

Figure 2-17 The developments of interphase precipitation on an incoherent interface in L-Z model, the front of interface is curved for this case. (a, b) a ledge developed on the interface then grows laterally and increases its height, generating the flow of solutes from the top to the previous row of precipitation (c) primary precipitation occurs on the top of ledge (the superledge); (d) the superledge continues to expand laterally, leading additional precipitation to form at the middle of superledge boundary; and (e) the diffusion of solute atoms along incoherent interphase boundary leads to further precipitation (secondary precipitation). [13]

It is expected that the sheet spacing contributed from different interfaces would possess great differences. However, Lagneborg and Zajac had compared the geometry of interphase precipitation using Figure 2-16 and Figure 2-17, and claimed that the sheet spacing contributed from different interfaces was differed by less than 20%. They claimed that such a discrepancy was an acceptable value. In their following discussion, the equations 2-63 to 2-66 are used to yield an approximation in predicting sheet spacing at different transformation temperatures, independent of the nature of interface (semi-coherent or incoherent). The combination of equations 2-65 and 2-64 yields the final form of sheet spacing.

$$\lambda = \left(\frac{a(D\delta)^{boundary} S}{2K_1} \right)^{1/2} \tag{2-67}$$

The sheet spacing can be obtained from c_V^{α/γ^*} (equation 2-65) and the corresponding a can be determined by equation 2-67. The diffusivity of solute at

interface is assumed to be 8 times than that of Fe. At a given transformation temperature, it has shown that for Fe, the empirical expression of $(D\delta)^{boundary}$ is

$$\left(D\delta\right)^{boundary} = 5.4\times10^{-5}\exp(\frac{-155000}{RT}) \tag{2-68}$$

The L-Z model also reveals the variation of sheet spacing with different V, N, and C contents were examined. The results can be summarized as follows:

a. higher carbon content would lead to a wider sheet spacing because the growth rate of ferrite is decelerated as the carbon content is increased. It means that the interface would move further to accumulate sufficient alloying elements for precipitation.
b. Lowering V addition generates a wider sheet spacing as well. It is rationalized as the ferrite/austenite interface should move further to collect sufficient solute content ahead of the interface for another precipitation process. Such an effect is corresponding to increase carbon concentration.
c. Increasing the N content will make the sheet spacing finer significantly because the driving force of precipitation is increased. It means that the critical concentration for precipitation is reduced as well.

In summary, the sheet spacing predicted by the L-Z model shows reasonable agreements with experimental data, even though it exhibits inconsistencies with the data obtained at lower temperatures (< 700 ^{o}C). The deviations at lower temperatures were supposed to be resulted from the interface equilibrium conditions transits from local equilibrium to para-equilibrium.

2.3.2 The Superledge on the ferrite/austenite interface

The determination of the height of a superledge was firstly addressed by Bhadeshia. His model is aimed at predicting the *minimum height* of superledge in the diffusional austenite-to-ferrite transformation. In his work, it did not involve any carbide precipitation events in the minimum ledge height calculation. Instead, he used the sheet spacing of interphase precipitation to check the availability of his model. It shows that the sheet spacing of interphase precipitation, which is dependent on ledge

height, is *always* higher than that he predicted. This confirms his argument that the superledge height predicted in his model offers the lowest limitation for a ledge nucleation. As the height of a ledge is smaller than this value, the nucleation of a ledge is not possible.

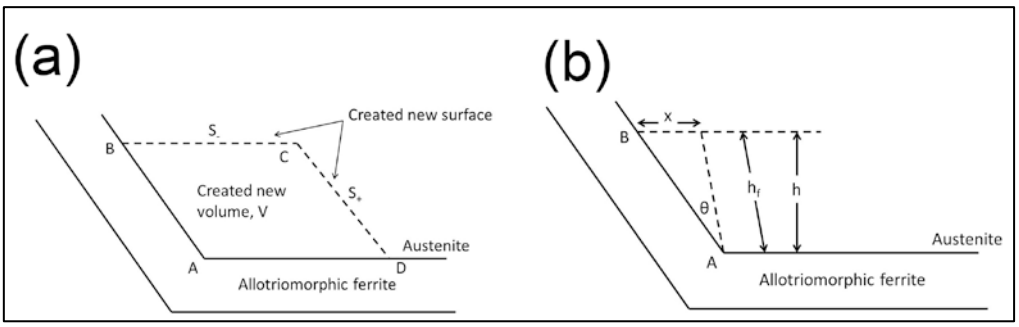

Figure 2-18 Schematic illustrations showing (a) the developing of a unit ledge on allotriomorphic ferrite by diffusional transformation, and (b) geometric analysis of superledge development. [56]

The minimum height of ledge is predicted by energy balance and classical nucleation theory. For a unit ledge nucleates on a ferrite/austenite phase boundary, as shown in Figure 2-18(a), it creates a new volume of ferrite (area *ABCD* with a unit height pointing out of the paper) and creates two additional surfaces (segments *BC* and *CD*). This process accompanies with the changes in a chemical free-energy change (ΔF_V^m) and increases the surface energies (S_+, and S_-). In order to nucleate a unit ledge, the change in free energy change should be larger than the surface energies for creating the two additional areas. Therefore, the condition

$$V \cdot \left|\Delta F_V^m\right| > (S_+ + S_-) \tag{2-69}$$

is expected to be followed.

Assuming the interface *AB* is the active phase boundary. Because the solute is accumulated ahead of the interface during austenite-to-ferrite transformation, the point *A* would act as a pivot point as the segment *AB* advances. As the nucleation of a superledge occurs, the interface *AB* will try to move forward to certain distance, *x*, around the point *A,* as indicated in Figure 2-18(a). Assuming $h_1 \sim h$, as shown in Figure 2-18(b), the free-energy change per volume, ΔF, generated by the formation of the nucleus of ferrite is written as

$$\Delta F = \sigma x + S_{+} + \Delta F_V^m (xh/2) \tag{2-70}$$

where h is defined as the height of a superledge and σ is the unit surface energy. Again, the height of this volume is set to point out of the paper with a magnitude of unity. The change of ΔF with respect to the volume of nucleus can be obtained by differentiating ΔF with respect to the area $xh/2$

$$\frac{d(\Delta F)}{dA} = \frac{2\sigma}{h} + 2\left|\Delta F_V^m\right| \tag{2-71}$$

The critical condition for the nucleation of a superledge is obtained by simply making equation 4-71 to be zero, and it yields

$$h^* = \frac{\sigma}{\left|\Delta F_V^m\right|} \tag{2-72}$$

This critical height, h^*, provides a lower limit for the size of superledges in any steel. That is, all experimental measurements should exceed h^*.

2.3.3 The models for fibrous carbide

Several models had been proposed to describe the formation of carbide fibers in different alloy systems. For the Mo_2C in spiky nodules (Figure 2-19), it was suggested that while austenite transformed to ferrite, carbons rejected from austenite surround ferrite platelets, providing sufficient carbon solutes for Mo_2C nucleation at both sides of ferrite platelets. In the successive of transformation, the growth of ferrite continues to reject carbon, leading to repeated nucleation and growth of Mo_2C.

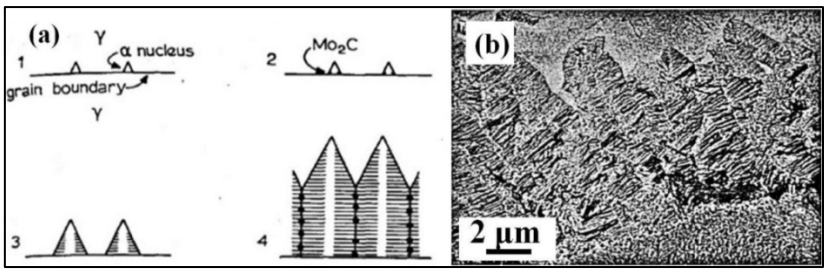

Figure 2-19 Model illustrating the Mo2C carbides formed in spiky noduls. Fe-4.10Mo-0.23C (wt%) isothermal transformation at 650 oC for 2 hours [46]

For Fe-V-C steels, Edmonds also provided another model to illustrate the fiber growth of VC, and compared it to interphase precipitation (Figure 2-20). It shows a basic difference between interphase precipitation and carbide fiber. In the case of interphase precipitation, the interface should *wait for* carbides to precipitate on it until sufficient carbons are consumed for further austenite to ferrite transformation. On the contrary, the carbide fiber *grows with* a direction normal to the interface. The carbons consumed by the formation of fibers should be approximately equal to that rejected from ferrite phase. The development of carbide fiber is similar to pearlite reaction in steels [54], which the pearlitic ferrite and cementite grow into the austenite via cooperative process. The difference between carbide fiber growth and pearlite reaction lies on the diffusion of atom. For carbide fiber, it is controlled by the ease of diffusion of substitutional solute atom (Cr, Mo, V, etc.). For pearlite reaction, the Fe_3C formation is mainly related to carbon diffusion.

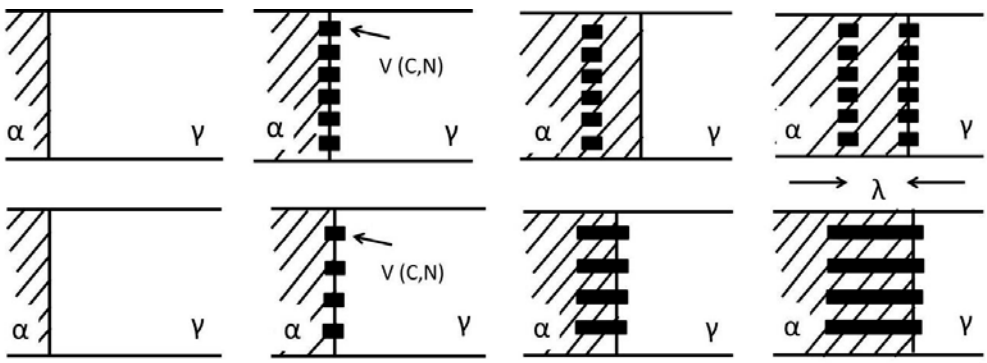

Figure 2-20 A comparison (a) interphase precipitation, and (b) fiber growth. [3]

Other models based on different considerations from other workers were briefly summarized by Li and Todd [12], as shown in Figure 2-21 and Figure 2-22. However, the proposed models cannot be used to cover so far observations of carbide fiber in

alloy steels. For example, the model illustrated in Figure 2-21 indicates the ferrite/austenite interface is incoherent, not crystallographic related by Kurdjumov-Sachs orientation relationships. However, this model cannot explain the transition of carbide morphology from interphase precipitation to fibrous from. On the other hand, the model presented in Figure 2-22 takes crystallographic into considerations. It demonstrates the formation of carbide fiber initiates on low energy interface, and its nucleation and growth are on the side of austenite, not ferrite. However, it is generally accepted that fibrous carbides are mainly associated with high energy, incoherent interfaces and our investigations on the diffraction patterns have shown the fibrous carbides exhibit Baker-Nutting orientation relationships with respect to ferrite. It indicates the nucleation and growth of fibrous carbides are related to ferrite, not austenite.

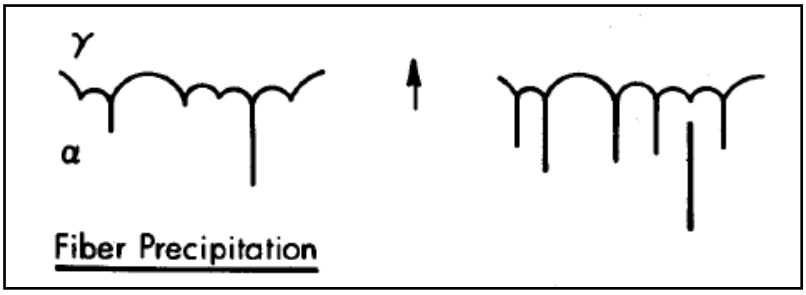

Figure 2-21 A model describing the fiber precipitation in association with migrating austenite/ferrite interface [12]

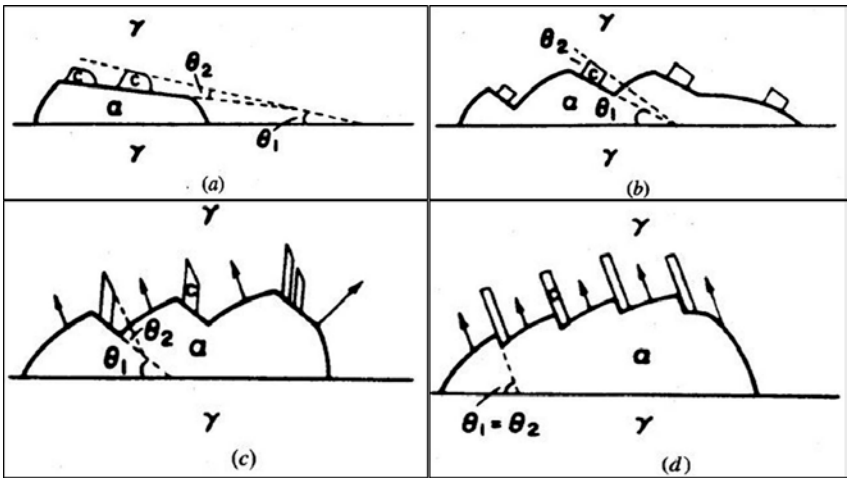

Figure 2-22 Another model concerning the crystallographic basis. The carbide morphologies are controlled by θ_1 and θ_2, where θ_1 is the angle between slowest moving austenite/ferrite interface and grain boundary, and θ_2 is the angle between slowest moving austenite/ferrite and austenite/carbide interfaces [61]

2.4 The mechanical properties of microalloyed steels

The mechanical property of steel is mainly controlled by its microstructure. In order to obtain high strength steels, four methods are generally applied to modify the microstructure:

(a) *By transformation at different temperatures or different cooling rates:*

It controls the proportion of ferrite, pearlite, bainite and martensite in the microstructure.

(b) *By deformation before transformation:*

This approach is mainly used to refine the microstructure. The degree of deformation before austenite decomposition determines the density of defect. The more defects generated in the prior austenite, the finer the microstructure and the better strength and toughness.

(c) *By introducing second phases:*

This method now usually stands for precipitation or dispersion hardening. The carbide, nitride, and second particles showing in the matrix act as the obstacles to limit the movement of dislocation during deformation. The particle (or the second phase) can be sheared or by-pass, depending on its size and physical bonding between atoms.

(d) *By inducing the lattice strain*

This is mainly attributed by substitutional alloying elements. The difference of atom size between the substitutional atom and matrix creates a strain field. The type of the strain field can be compression or expansion, depending on the size of substitutional atom. Si and B have been well applied in this field.

The following discussions will be concentrated on the third strengthening mechanism, i.e. the precipitation hardening.

2.4.1 The strength of ferrite

For low carbon steels, ferrite is the main phase shown in the microstructure. It is

a soft phase and usually responsible for formability of steels [62]. If the strength of ferrite is increased, the steel is expected to perform high strength in combination of considerable elongation. The strength of ferrite can be considered as the addition of various strengthening effects. Following the empirical equation proposed by Gladman [63]

$$\sigma_{y,\alpha} = \sigma_i + \sigma_{ss} + \sigma_g + \sigma_{pp} = 115.58 + 53.4wt\%Si + 4.28wt\%Mn + 0.58d_\alpha^{-1/2} + \sigma_{pp} \tag{2-73}$$

where σ_i is the friction stress of ferrite, σ_{ss} is solid solution strengthening, d_α is ferrite grain size in mm, and σ_g is the grain refinement strengthening. The precipitation strengthening, σ_{pp}, is contributed by the interaction of carbide and dislocation (being on similar scales and strength, they should be quadratically summed up)

$$\sigma_{pp} = \sqrt{\Delta\sigma_{disl.}^2 + \Delta\sigma_{Orowan}^2} \tag{2-74}$$

where $\Delta\sigma_{disl.}$ is the increased yield strength because of the increased dislocation density and $\Delta\sigma_{Orowan}$ is the precipitation strengthening estimated from Orowan equation. For dislocation strengthening, it is formulated as [64]

$$\sigma_d = \kappa MGb\sqrt{\rho} \tag{2-75}$$

where κ is a geometric constant assumed to be 0.435 [64], *G* and *b* are the shear modulus and Burger's vector respectively, and *M* is the Taylor factor. The relation of dislocation density ($1/m^2$) to the amount of strain is given by

$$\rho = 5.3\times10^{15}\varepsilon^{1.1} \tag{2-76}$$

By using the proof strength at 0.2% strain, the dislocation density, ρ, is assumed to

be $5.69\times10^{12}\,\mathrm{m}^{-2}$ in isothermally transformed allotrimorphic ferrite [14], and then the calculated dislocation strengthening is $\Delta\sigma_{disl.} = 66.28$ MPa.

The relevant equations for estimating each strengthening mechanisms in ferrite have been widely used in numerous studies [14, 20, 65, 66]. Among the strengthening components in equation, $\Delta\sigma_{Orowan}$ is the most difficult one to be determined because it is associated with carbide distribution in matrix and with nature of particle, and how the carbide interacts with dislocations. An approximate precipitation strengthening is viewed as the difference between measured $\sigma_{y,\exp}$ and other strengthening components

$$\sigma_{pp} = \sigma_{y,\exp} - \left(\sigma_{\circ,\alpha} + \sigma_{ss} + \sigma_{g}\right) \tag{2-77}$$

This approach, however, does not give objective interpretations on how the presence of carbide improves the strength of materials. Theories for predicting precipitation hardening were rigorously proposed and will be discussed in detail as follows.

2.4.2 Precipitation hardening in alloyed steels

The interaction of dislocation with particle is schematically visualized in Figure 2-23, followed after the work of Gladman [67]. The precipitation strengthening depends on the ease of dislocation to pass through particles in matrix, depending obviously on spacing between carbides on the slip plane (related to carbide volume fraction and carbide size), nature of carbide (the resistance to dislocation tension), and crystallographic orientation at particle/matrix interface (degree of coherency). From Figure 2-23, the force balance between the line tension of dislocation, *T*, and the resistance force of the second phase particle, *F*, shows that

$$F = 2T\sin\theta \tag{2-78}$$

It requires additional stress have to be increased for further deformation. Under this condition, the final strength of precipitation hardening predominantly depends on the particle spacing, which is related to carbide volume fraction and its size. On the contrary, if $F_{\max}$ is attained before $\sin\theta = 1$, the carbide will be cut by dislocation

and the precipitation strengthening is accordingly resulted from the creation of new particle/matrix interface, known as cutting mechanism or chemical strengthening.

It has been recognized that cutting mechanism can occur only under the special condition that the interface between the particle and the matrix is coherent. The generated new particle/matrix interface could be an anti-phase disorder interface or a stacking fault, depending on the orientation relationship of particle and matrix. Furthermore, a feature of precipitated-hardened is associated with the strain field around particles, especially in the early stage of precipitation. The proposed equations for calculating the strength contribution of chemical strengthening are given in Table 2-3

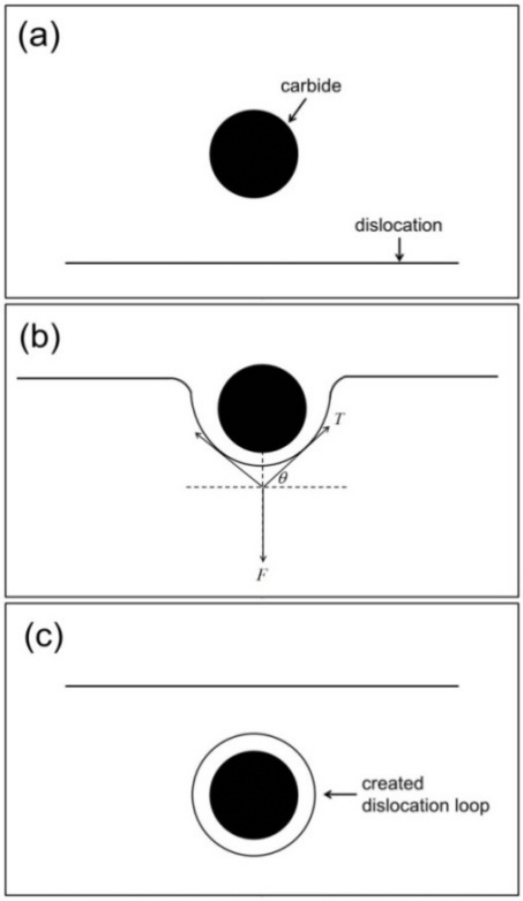

Figure 2-23 Schematic illustration showing Orowan bypass mechanism of dislocation through carbide. (a) a dislocation is going to pass by a particle in matrix; (b) the dislocation is bowed because of the resistance force exerting from the particle, and (c) the dislocation passed by the particle and left a dislocation loop around the particle

It has been recognized that cutting mechanism can occur only under the special condition that the interface between the particle and the matrix is coherent, and only

when the spacing is small enough so that bypassing the precipitates requires too much stress. The generated new particle/matrix interface could be an anti-phase disorder interface or a stacking fault, depending on the orientation relationship of particle and matrix. Furthermore, a feature of precipitated-hardened is associated with the strain field around particles, especially in the early stage of precipitation. The proposed equations for calculating the strength contribution of chemical strengthening are given in Table 2-3

It can be seen that in Table 2-3, the coherent strain strength shows different carbide equations proposed by Gladman. For small particles, coherency strain hardening increases with increasing particle size; whereas for larger particles, the coherency strain hardening demonstrates an opposite tendency. The critical particle size for the transition is given by [67]

$$\frac{r}{b} = \frac{1}{4}\varepsilon^{-1} \tag{2-79}$$

Generally, a large particle is recognized to be able to resist dislocation tension during deformation; on the contrary, a small particle is easy to be deformed by the passage of dislocations. The critical size of particle to avoid being sheared by dislocation is also given by equation 2-79.

Table 2-3 The equations for chemical or cutting strengthening mechanisms

Ref.	Mechanisms	Equations
Ham [68]	Anti-phase boundary	$\Delta\tau_{pp} = \frac{2}{b}\sqrt{\frac{\gamma r_s f_p}{\pi T}}$
Kelly [69]	Stacking fault	$\Delta\tau_{pp} = 2\frac{(\gamma_s/b)^{3/2}}{\sqrt{bLT}}$
Gladman [67]	Coherent strain field for small particle	$\Delta\tau_{pp} = 4.1G\varepsilon^{3/2}\left(rf_p/b\right)^{/2}$
	Coherent strain field for large particle	$\Delta\tau_{pp} = 0.7Gf_p^{1/2}\varepsilon^{1/4}\left(b/r\right)^{3/4}$

2.4.3 The Orowan and Ashby-Orowan equations

It has been known that a smaller particle, the easier to be deformed or sheared by dislocations. However, for alloyed carbides, it has been pointed out that the transition

of cutting mechanism to Orowan looping must occur at extremely small particle size because of their small volume fraction. For alloy carbides, it is suggested that a carbide size of 5 nm is capable of resisting deformation [67]. As a consequence, for the steels which are hardened by alloy carbides, the yield strength is suggested to be described by the Orowan [70] or Ashby-Orowan equations [71].

Theory for estimating precipitation hardening in ferrite is originated from the well-known Orowan equation

$$\tau_{Orowan} = \frac{Gb}{L} \tag{2-80}$$

where L is the inter-particle spacing on slip plane, as discussed by Kocks [72], related to volume fraction (f_p) and carbide diameter in three dimension (D)

$$L = D\sqrt{\frac{\pi}{6f_p}} = \sqrt{\frac{2\pi R^2}{3f_p}} \tag{2-81}$$

where R is the carbide spatial radius. By combining equations 2-80 and 2-81, the increased yield strength by precipitation hardening is given by [63]

$$\sigma_{Orowan} = \frac{6Gb}{D}\sqrt{\frac{3f_p}{2\pi}} \tag{2-82}$$

where G is shear Modulus of material and b is the Burger's vector. It should be kept in mind that D presented in equation is the carbide diameter in spatial, not in the projected 2 dimension image; out of convenience, the conversion of D to the carbide size in the intersection of slip plane, d, is proposed by [63].

$$D = d\sqrt{\frac{3}{2}} \tag{2-83}$$

from which d is the diameter of carbide measured directly from the micrographs.

The Orowan equation generally yields an overestimated prediction because it

considered carbides are regular array and lie on a square grid in the slip plane, as shown in Figure 2- 24.

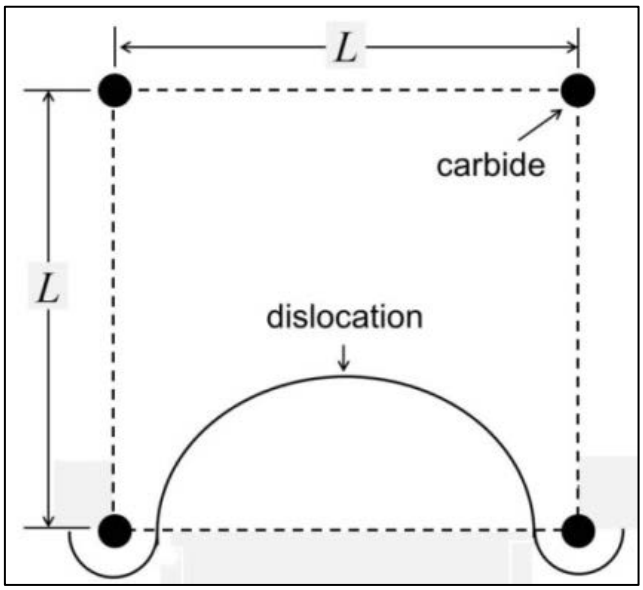

Figure 2- 24 Schematically illustration showing the regular square array of particles and their interaction with a dislocation proposed in Orowan model.

It would be more realistic to use the case of carbides are randomly distributed in matrix. Ashby considered the real dislocation line segment interacts with carbide and finite particle size; the Ashby-Orowan equation for precipitation hardening now derived as

$$\tau_{Ashby-Orowan} = 0.84 \frac{Gb}{2\pi(1-\nu)^{1/2} L} \ln(\frac{d}{2b})$$

(2-84)

where ν is the Poisson ratio, approximately being 0.3 for metals. Attention has to paid on *d,* instead of *D*, is used in Ashby-Orowan equation. Out of convenience, equation is generally expressed in terms of particle volume fraction and size [67]

$$\sigma_{Ashby-Orowan} = \left(0.538Gb\frac{f_p^{1/2}}{D}\right)\ln\left(\frac{D}{2b}\right) \quad (2\text{-}85)$$

For the case of carbide precipitates in ferritic matrix, it becomes [63]

$$\sigma_{Ashby-Orowan} = 10.8\frac{\sqrt{f_p}}{D}\ln(1630D) \tag{2-86}$$

Or in another form

$$\sigma_{Ashby-Orowan} = 5.9\frac{\sqrt{f_p}}{\bar{d}}\ln\left(\frac{\bar{d}}{2.5\times10^{-4}}\right) \tag{2-87}$$

Equations 2-86 and 2-87 have been widely used to estimate the precipitation hardening of the interphase-precipitated carbide [19, 20], even though these equations are derived for the carbides in random array. The random array of carbide, that is, an effective spacing, in matrix is expected to result in a smaller precipitation hardening increment than that predicted simply from Orowan equation, which considered the case of the minimum particle spacing in the slip plane. General speaking, Orowan equation is more important in steels with high volume fraction of large carbide; on the contrary, the Ashby-Orowan equation is suitable for the case which particle size is negligible with respect to the particle spacing [63].

However, how to precisely describe and determine the magnitude of L is the most difficult part for the precipitation hardening prediction [72, 73]. The proposed equations to estimate the particle spacing, L, are summarized in Table 2-4.

Table 2-4 The used particle spacing in different approaches.

References	L
Orowan and Ashby-Orowan [63]	$D\sqrt{\frac{\pi}{6f_p}}$
Batte [66]	$\sqrt{\left[\frac{\pi a}{4}\left(\frac{a}{f_p p\lambda}+1\right)-\frac{3.5a}{p}\right](\lambda-0.233a)\bullet 3.72}$
Yen [14]	$\sqrt{\left[\frac{b_p^2}{d}+\frac{\pi d}{4}-\frac{1.73d}{p}\right]3\bullet(\lambda-0.61d)}$
Kuo [65]	$\sqrt{\frac{2\pi r_p^2}{3f_p}}$

Miyamoto [74]	$\frac{1}{\sqrt{2\overline{r_p}\rho_p}} - 2\overline{r_p}\sqrt{\frac{2}{3}}$

2.5 Summary of the chapter

After the review on the previous studies concerning the microstructure, modeling, and mechanical properties, the motivation of the present study can be revealed. It has shown that the conditions for the development of fibrous carbide are contradicted among studies and the transitions of the interphase-precipitated carbide to the fibrous carbide are unclear. The present work firstly deals with these issues and then clarifies the conditions for the fibrous carbide development. A model is subsequently developed to predict the features of interphase precipitation process with the growing ferrite phase during transformation. It computes in a self-consistent manner all the features of the microstructures from thermodynamics and kinetic data only. The features of the obtained microstructures will be compared to the prediction of the model. Finally, efforts will be made to correlate the observed microstructure with the mechanical properties.

Chapter 3

Experimental investigations of the as-received materials

3.1 Introduction

The as-received materials are the hot-drawn steel bars for reinforcing concrete (RC) construction uses. Because of the increasing population density in the world (and especially in the economically booming Asia), the high-rise building becomes more and more efficient to store more people in a given area. Therefore, the improvement of RC structure becomes the priority for the construction companies.

The capability of high-rising RC building to anti-earthquake has been deeply considered since 1981, and a five-year project, the new RC project, was initiated to develop the new materials (concrete and steel bar) and construction methods for RC high-rising buildings [1]. The one division of new RC project conducted by Prof. Morita et al. was devoted to developing ultra-high strength steel bars (UHSB). A series of UHSB had been successfully developed and commercialized for different requirements, as shown in Figure 3-1. The newly developed UHSBs had been claimed to possess a yield strength higher than 685 MPa, and several strength levels of UHSBs have been designed for different applications. The detailed classifications can be seen in Reference [1]. The UHSBs presented attractive mechanical properties, for examples, high strength, good elongation, apparent yield point and yield plateau.

However, the detailed microstructure of UHSB has not drawn much attention. The difference of microstructure between conventional steel bar (CB) and UHSB is briefly revealed in Figure 3-1. It can be found that the ferrite grains are greatly reduced in the microstructure of UHSB but this could not be the only one reason to account for the high yield strength of UHSB (> 685 MPa). In the next section, the detailed microstructures of UHSBs were examined via microscopies. Furthermore, some efforts have been made to calculate the strengths contributed from different mechanisms quantitatively, and to correlate the microstructure with stress-strain curves.

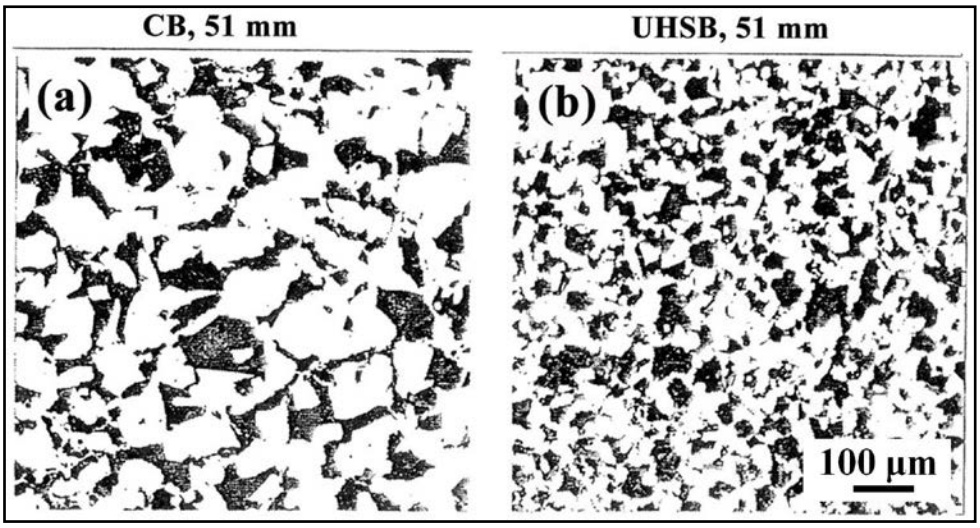

Figure 3-1 The optical metallography of (a) CB, and (b) UHSB showing that both of them are consisted of ferrite and pearlite but the microstructure of UHSB is greatly refined [75]. The white phase is ferrite and the dark phase is pearlite.

3.2 Experimental Procedures

The present analyzed steels were provided by Taiwan Tunghe Steel Corporation. Steel-A and Steel-B are studied first to give the representative microstructure of this engineering material. Their compositions are given in Table 3-1. The detailed processing condition cannot be revealed here due to the proprietary reasons.

Table 3-1 Chemical compositions of Steel-A and Steel-B (wt%)

	C	Si	Mn	V	Nb
Steel-A	0.37	0.26	1.10	0.26	0.04
Steel-B	0.34	0.34	1.37	0.27	0.05

Samples for optical microscopy were ground and etched with 3% nital solution. Thin foils for TEM were electro-chemically polished in a twin-jet electro-polisher using a solution of 5% per-chloric acid, 25% glycerol and 70% ethanol at -7 ^{o}C and 50 V. They were examined by JEOL 100CX II TEM and TECNAI G2 TEM operating at accelerating voltage 100 kV and 200 kV, respectively. The size of carbides, inter-sheet spacing of carbides, and inter-lamellar spacing of pearlite were measured directly from the TEM micrographs. Microhardness tests employed a loading of 10g and a dwelling time of 7 seconds. Each average value of microhardness has been determined from at least 30 data points in a sample. The size of the indenter was about 3 μm.

3.3 The Microstructure

a. Optical Microscopy

Figure 3-2 shows the optical metallography of each sample. The both microstructures consist of ferrite and pearlite and the grain size of the ferrite is relatively fine (< 10 μm). The difference in grain sizes of ferrite was mainly controlled by the degree of deformations. For Steel A with more amount of thermo-mechanical deformation, the grain size of ferrite was further to be smaller than 5 μm. For Steel B, the banding structure can be observed. The existence of the banding structure was supposed due to element segregation, especially those of manganese and sulfur. However, in the later section, the testing of the mechanical properties showed that the banding structure did not have any significant effect on the mechanical properties. The grain size and volume fraction of each phase are listed in Table 3-2.

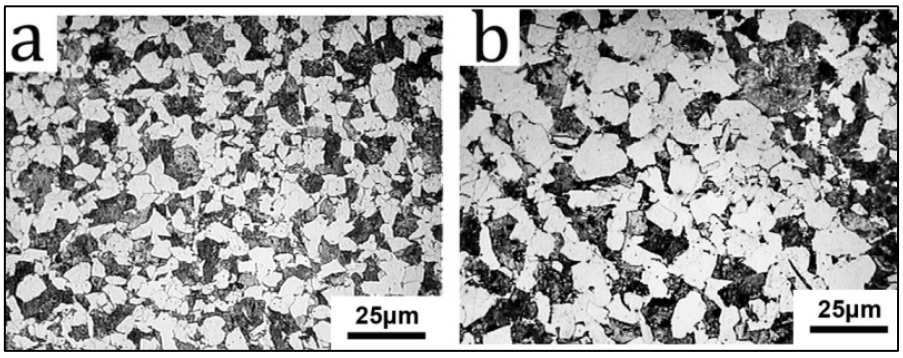

Figure 3-2 Optical micrographs of UHSSBs revealing microstructures composed of ferrite and pearlite: (a)Steel-A; (b) Steel-B.

Table 3-2 The microstructural features of UHSBs

Sample No.	Steel-A	Steel-B
Ferrite volume fraction (%)	40.3	45.2
Ferrite grain size (μm)	4.7 ± 1.2	8.3 ± 0.8
Sheet spacing of interphase precipitation (nm)	19.6 ± 2.8	20.3 ± 1.8
Carbide size (nm)	9.0 ± 2.3	11.4 ± 2.6
Pearlite spacing (nm)	173.4 ± 11.7	145.8 ± 8.3
Dislocation density in ferrite (m^{-2})	9.3×10^{13}	2.1×10^{13}

b. Mechanical properties

In the beginning, Vickers microhardness test has been used for the estimation of

the strength of each phase. Because the grain size of ferrite is relatively fine, the indenter would cover the grain boundaries or very close to grain boundaries. Thus, the effects of ferrite grain boundary strengthening would be included in the tested values. In Table 3-3, the value of Vickers hardness (Hv) of ferrite in Steel A is slightly higher as compared with that in Steel B. The difference is suggested to be resulted from different ferrite grain size. The smaller the ferrite grain size, the higher the value of Hv. On the other hand, the Hv of the pearlite is higher in Steel B than in Steel A. That could be explained by the finer inter-lamellar spacing of pearlite in Steel B. The detailed microstructures will be discussed in the later section.

Table 3-3 The mechanical properties of UHSBs

	Steel-A	Steel-B
Ferrite (Hv)	281.6±7.3	273.9±3.7
Pearlite (Hv)	351.5±8.6	361.2±5.9
Yield Strength (MPa)	830.75±13.7	752.5±10.6
Tensile Strength (MPa)	1002.6±14.2	921.7±9.2
Elongation (%)	11	12

Tensile tests were used to reveal the elasto-plastic behaviors of UHSB. In Figure 3-3, the relative stress-strain curves show the amount of strain of the yield plateau can rise to be about 1.4% as the stress (785 MPa) is reached. It is suggested that the proportion of ferrite was sufficient to provide soft phase to be sustaining deformed under the high stress, leading to apparent yield points and yield plateaus in stress-strain curves.

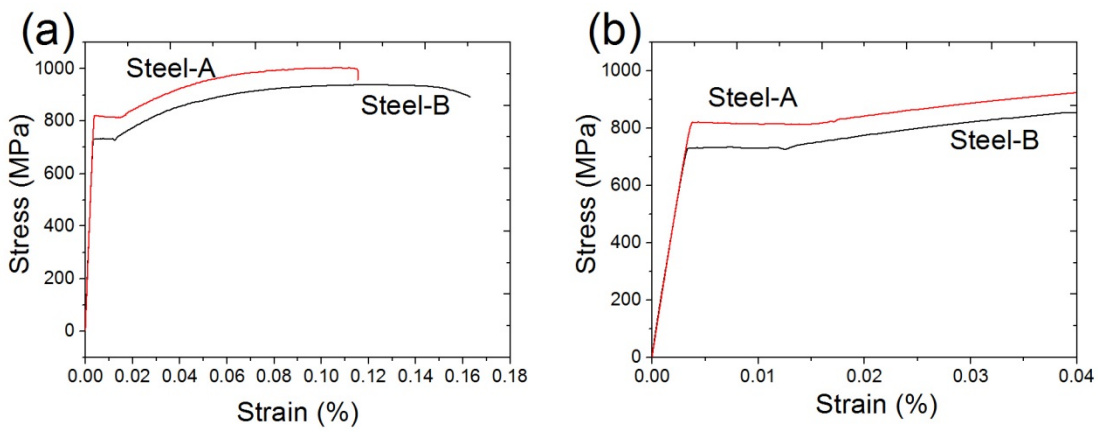

Figure 3-3 (a) Stress-Strain Curves of Steel-A and Steel-B, demonstrating apparent yield point and yield plateaus, and (b) local magnification at yield point.

The microstructures of UHSB were similar to conventional steel bars; both consisted of ferrite and pearlite. But the results of tensile tests and macroscopic mechanical properties (presented in Table 3-3) demonstrate that the yield strengths and microhardness values of each phase are much higher than those of conventional steel bars. For conventional steel bars, the strengths of ferrite and pearlite are about 120 Hv and 280 Hv, respectively. In order to understand the increment of strengths, Transmission electron microscopy has been utilized to examine the microstructures of UHSBs in detail.

c. Transmission Electron Microscopy (TEM)

The detailed microstructure was analyzed by TEM. Figure 3-4 clearly displays that the carbides interphase precipitated in a ferritic matrix with regular spacing. Such a carbide array has been widely studied and applied to manufacture high strength steel plates for automobiles [76]. For Steel-A, the carbide size and sheet spacing are about 9 nm and 20 nm, respectively; for Steel-B, the two parameters were about 11.5 nm and 21.4 nm, respectively. It indicates that the degree of deformation before austenite-to-ferrite transformation did not affect greatly on the interphase-precipitated carbides. The carbides distributed in this manner are effective to limit dislocation motion. Figure 3-4(a) clearly gives an example showing how the interphase-precipitated carbides interact with the dislocation.

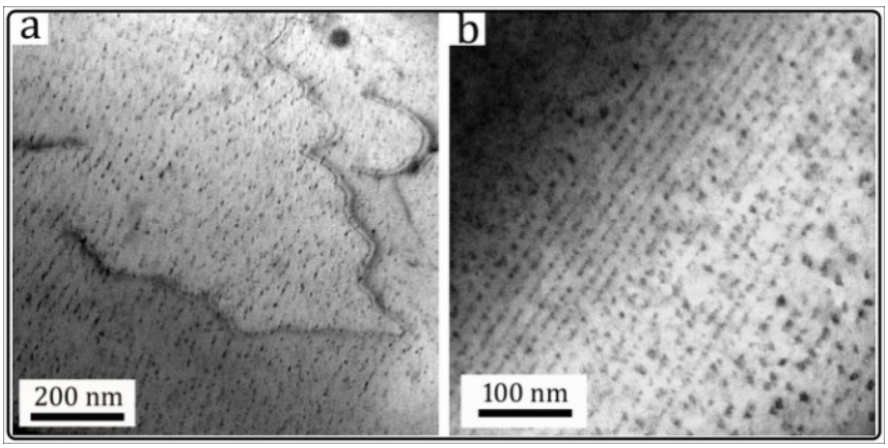

Figure 3-4 The TEM micrographs showing typical inter-phase precipitated carbides in ferrite: (a) Steel-A; (b) Steel-B. Fig. 2(a) clearly showing that dislocations were pinned by these carbides.

The structure and chemistry of the interphase-precipitated carbide were analyzed by electron diffraction patterns and EDX analysis. The bright-field and dark-field

image with the corresponding diffraction patterns are shown in Figure 3-5. The diffraction patterns reveal that the carbide had an FCC structure and obey one variant of Baker-Nutting orientation relationship with the ferritic matrix as follows:

$$\begin{pmatrix}0 & 0 & 1\end{pmatrix}_{VC} \parallel \begin{pmatrix}0 & 0 & 1\end{pmatrix}_{\alpha}$$

$$\begin{bmatrix}1 & 1 & 0\end{bmatrix}_{VC} \parallel \begin{bmatrix}1 & 0 & 0\end{bmatrix}_{\alpha}$$

, which is consistent with previous studies on vanadium-containing steels [6, 7, 17, 18]. EDX analysis shows that these carbides contain a significant level of vanadium and niobium, as indicated in Figure 3-6.

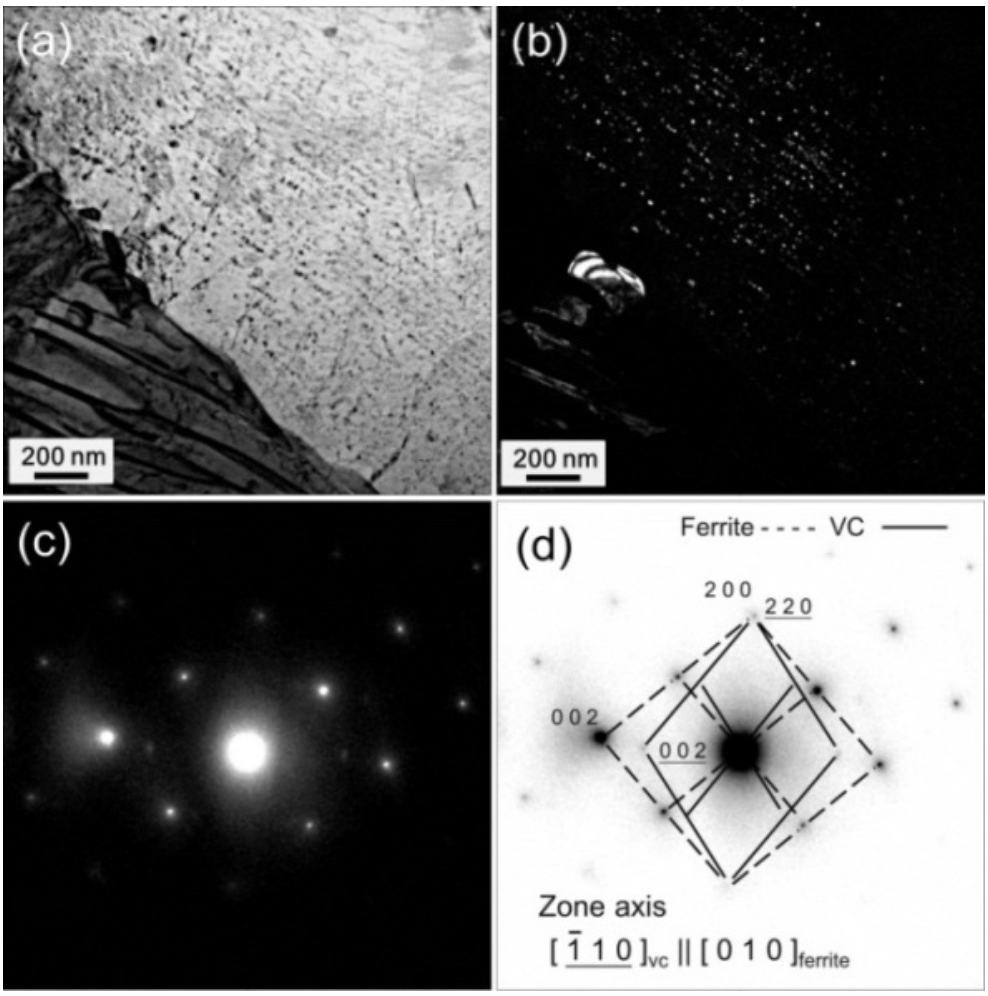

Figure 3-5 Bright-field and dark-field images and corresponding diffraction patterns of carbides. (a) Bright-field image; (b) Dark-field image illuminated by 002 carbide reflection; (c) Corresponding diffraction; (d) Identified orientation relationship of carbides and ferritic matrix.

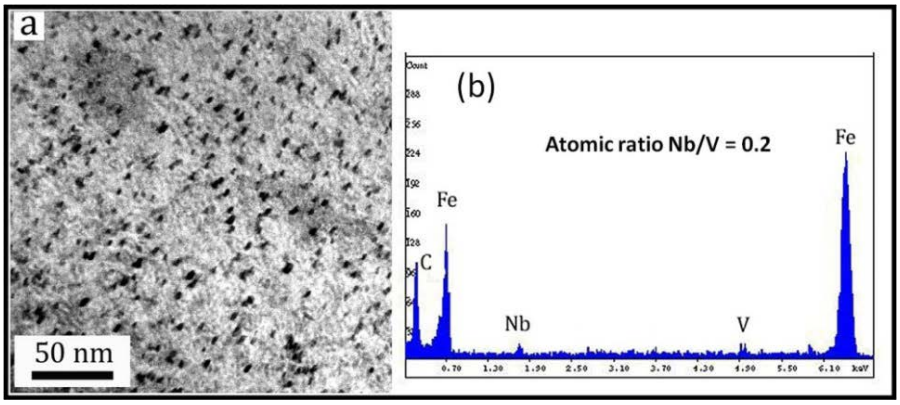

Figure 3-6 EDX analysis on nano-sized carbides demonstrating that were composed of niobium and vanadium.

In addition, the lamellar spacings of the pearlite in Steels-A and -B have been resolved by TEM. Figure 3-7 shows that the lamellar spacings of pearlite are very fine, and no carbides were observed into the pearlitic ferrite. This result is not similar to that reported in other studies [6, 47, 52], which asserted that carbides were found in pearlitic ferrite. The occurrence of carbides in pearlitic ferrite has not been systematically investigated yet. It was presumed that the rate of transformation should be slow enough to allow carbides to have time to precipitate in pearlitic ferrite. For the present as-received materials, the prior austenite grain size was relatively small due to the addition of Nb and great amounts of defects created during hot-rolling process, so the rate of transformation of these UHSB was expected to be relatively higher. Thus, no carbides precipitated in pearlitic ferrite can be observed in the Steels-A and -B.

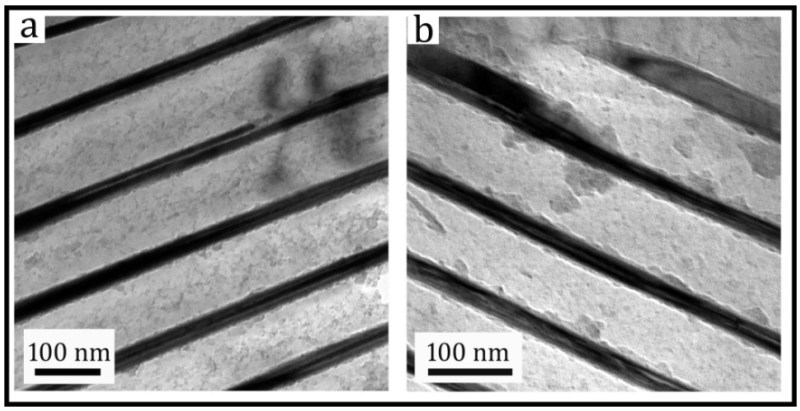

Figure 3-7 The fine inter-lamellar spacing of pearlite in UHSSBs: (a) Steel-A; (b) Steel-B. It shows that the spacing is about 100 nm.

The mean lamellar spacing has been measured via by mean truce spacing , $\lambda_{\circ}$, which is related with mean intercept spacing *L*. *L* and $\lambda_{\circ}$ are related by a factor of 0.5 [54]:

$$\lambda_{\circ} = 0.5L \tag{3-1}$$

The results of estimated lamellar spacings have been listed in Table 3-2. The lamellar spacing of Steel-B is finer than that of Steel-A. As a consequence, the measured Hv of Steel-B is higher than that of Steel-A. The difference of pearlite spacing is presumed to be resulted from the degree of deformation during the thermo-mechanical process. The lamellar spacing of pearlite depends only on transformation temperature [77]. It is proposed that Steel-A is expected to have a higher transformation rate than Steel-B because it experienced a more severe deformation. During the continuous cooling, the pearlite reaction in Steel-A would start at a higher temperature than in Steel-B, resulting in a larger pearlite spacing.

3.4 Quantitative estimations of the strengthening contributions

The microstructural investigation has demonstrated that the UHSBs can achieve a higher strength level via refinement of ferrite grain, interphase precipitation, and decrease in inter-lamellar spacing of pearlite. The amount of strength contributed by each of the different mechanism was further estimated. Several useful equations to calculate the amount of strength contributions have been proposed and widely used in many studies. The strength of ferrite, $\sigma_{y,\alpha}$, can be estimated as the sum of contributions from different strengthening mechanisms:

$$\sigma_{y,\alpha} = \sigma_{\circ} + \sigma_s + \sigma_g + \sigma_i \tag{3-2}$$

where $\sigma_{\circ}$ is the friction stress of ferrite, σ_s the component of solid solution strengthening, σ_g the strength contributed by grain refinement, and σ_i the increment of strength from precipitation or dislocation interactions [63].

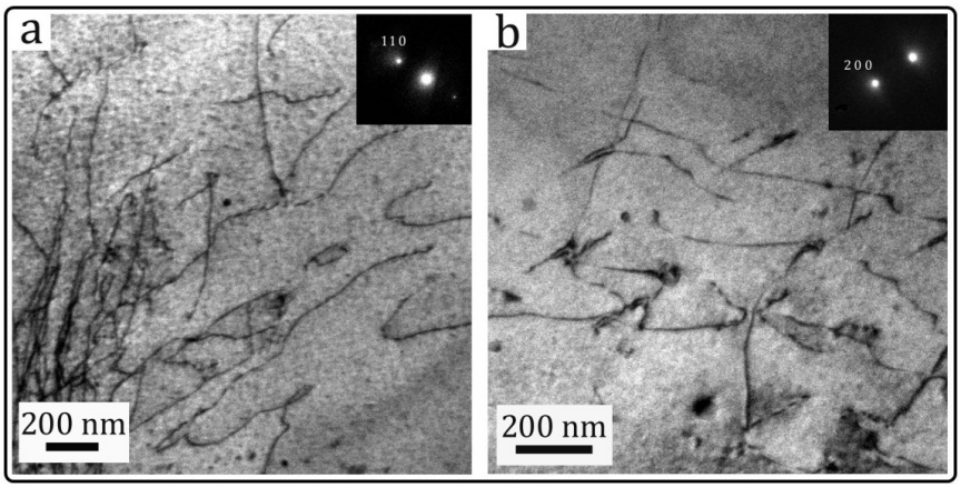

Figure 3-8 Representative TEM micrographs for the dislocation structures in ferrite matrix and corresponding two-beam conditions: (a) Steel-A; (b) Steel-B.

All the data in Table 3-2 and Table 3-3 have been used for the strength contributions in ferrite. In the calculations, the value of σ_i is considered mainly due to the dislocation strengthening, σ_{dis}, estimated by the following equation [64]:

$$\sigma_{dis} = 0.38Gb\rho^{0.5} \tag{3-3}$$

where G is the shear modulus of ferrite, b is Burger's vector, and ρ is the dislocation density. The representative TEM micrographs for the dislocation structures in ferrite in Steel-A and Steel-B are shown in Figure 3-8. Using the method in [64], the dislocation density can be quantitatively obtained. Table 3-4 gives the data for the measured dislocation density. It shows that the dislocation density in Steel A is higher, contributed from higher degree of deformation.

Table 3-4 The parameters of dislocation density calculations obtained via TEM

	Two-beam condition	Thickness fringe	Thickness of thin foil (nm)	Dislocation density (m^{-2})	Average
Steel-A	<110>	5	201.5	1.7×10^{14}	9.3×10^{13}
	<110>	5	197.6	4.8×10^{13}	
	<110>	6	241.8	5.7×10^{13}	
Steel-B	<112>	5	375.5	4.0×10^{13}	2.1×10^{13}
	<200>	4	235.6	1.6×10^{13}	
	<112>	4	300.4	8.0×10^{12}	

The calculated results of all strengthening mechanisms of ferrite were summarized in Table 3-5. It shows that the grain refining strengthening and precipitation hardening played key roles in UHSBs. However, the effect of dislocation hardening is not significant.

Table 3-5 The summary of strengths contributed from different mechanisms

Strengthening contribution (MPa)								
	σ_α				σ_p	$\sigma_{cal.}$	σ_{real}	$\Delta\sigma$
	$\sigma_\circ$	σ_s	σ_g	σ_{dis}				
Steel-A	65	57.6	261.1	54.7	647.7	492	830.8	338.8
Steel-B	65	71.4	196.5	35.6	757..3	442	725.5	221.5

The strength of pearlite was quantitatively estimated as well. Studies had shown that the strength of pearlite strongly depends on its spacing [7, 78, 79], which is a function of transformation temperature [24]. The relation of pearlite spacing to the strength of pearlite is given by [77, 80]:

$$\sigma_{y,p} = \sigma_{\circ,p} + KS^{-1} \tag{3-4}$$

where S is the pearlite spacing, K is a constant, and $\sigma_{\circ,p}$ is the friction stress of pearlite. In order to simplify our calculations, we neglected the dislocation interactions in pearlite and the internal stress caused by different thermal expansions of ferrite and pearlite at the interfaces [78]. The strength of pearlite can be estimated, as shown in Table 3-5, by using the measured pearlite spacing listed in Table 3-2.

After the strength of each phase is determined, the overall strength can be further estimated [63]. For the steels consisted of two phases, the total strength is controlled by the relative proportion of phases as

$$\sigma_{total} = f_\alpha^{1/3}\sigma_\alpha + \left(1 - f_\alpha^{1/3}\right)\sigma_p \tag{3-5}$$

where f_α is the volume fraction of ferrite; σ_α and σ_p are the strengths of ferrite and pearlite, respectively. Using the Table 3-2, the theoretical strengths of steel bar can be calculated, as listed in Table 3-5. The results indicate that there is a difference

between actual strength and theoretical strength. This difference is suggested to be attributed to precipitation hardening of the carbides (interphase precipitation). It is pointed out that the precipitation hardening in Steel-A plays a more important role on its strength, which is probably resulted from the more severe deformation of Steel A.

3.5 The occurrence of fibrous carbide in Steel-C

In addition to the interphase precipitation, carbide fiber was found in proeutectoid ferrite of Steel-C (Figure 3-9). The proportion of these carbide fibers is less to make great effects on the mechanical properties of UHSBs. Because such a carbide aggregate did not be found in Steel-A and in Steel-B, it is suggested the occurrence of fibers is mainly related with the slower cooling rate of Steel-C.

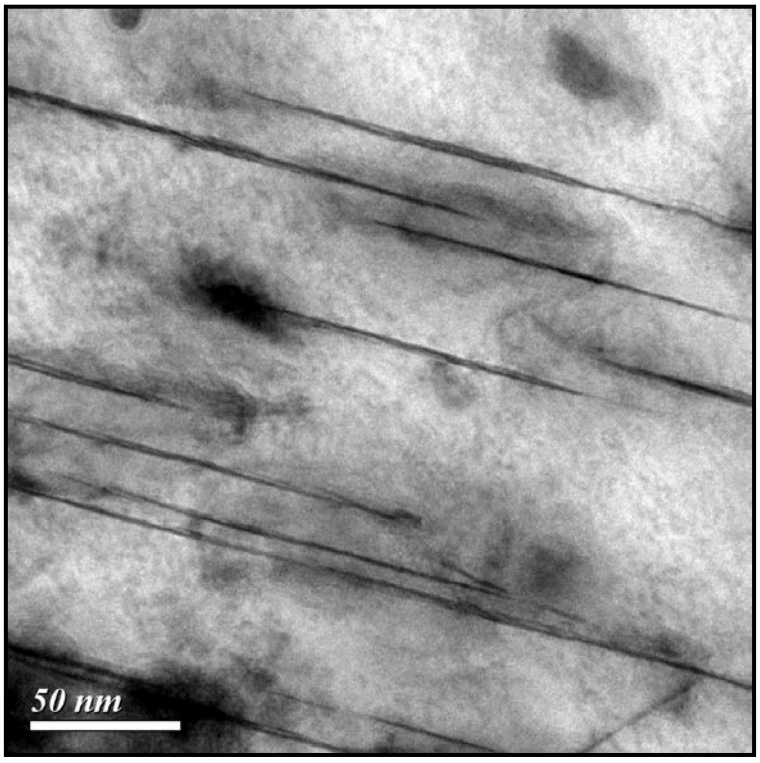

Figure 3-9 The VC fibers in Steel-C

3.6 Conclusions

Via the microscopic observations and quantitatively estimations on strength contributions from different mechanisms, some conclusions can be made as follows:

a. The higher strengths of UHSBs were mainly resulted from the refined ferrite grains and pearlite spacing than conventional steel bars.

b. The interphase-precipitated carbides in ferrite strengthened steel bars significantly. These carbides arranged in rows, acting as an effective way to inhibit the movement of dislocations.

c. The degree of deformation would be the key point in determining the resulting microstructure of UHSBs. It has shown that the more server deformation (Steel A), the finer the ferrite grain, and the higher in precipitation hardening contribution.

d. Sufficient ferrite makes the amount of strain in a “Luders’ like plateau” to be up to 1.4% before the onset of work hardening.

Chapter 4

The TEM investigations of the features of the interphase-precipitated carbide and the fibrous carbide

4.1 Introduction

Because Steel-C exhibits both interphase-precipitated carbide and fibrous carbides, such a composition of the steel is suitable to study the features of the different carbide aggregates and their competition. In the present work, precipitation of carbides in both pearlitic ferrite and ferrite was examined by transmission electron microscopy (TEM) after isothermal transformations at 650 ^{o}C for 1 h. The aim of the present work is to discuss the formation mechanisms of fibrous carbide and IP in both ferrite and pearlitic ferrite in a vanadium-containing medium-carbon steel, and to clarify the conditions of carbide morphology transition.

4.2 Experimental Procedure

The composition of Steel-C has been given in Table 1-1. The dilatometric specimens, prepared from the quarter diameter position of the original steel bars, were machined to 3 mm in diameter and 6 mm in length. The specimens were sealed in quartz tubes under argon atmosphere and thus homogenized at 1200 ^{o}C for 3 days in order to reduce the segregations, and water quenched to room temperature. The homogenized specimens were reheated to 1200 ^{o}C for 3 min and subsequently cooled at a rate of 20°C/s to 650 ^{o}C for isothermal transformation for 1 h. Finally, the transformed specimens were quenched to room temperature 100°C/s. The transformed specimens were ground, polished, and etched in 3% nital solution for optical microscopy (OM) observations. The Vickers microhardness was measured with loadings of 10 kg and 25 kg for ferrite and pearlite phases, respectively. The smaller loading conducted on ferrite was intended to avoid the influence from neighboring pearlitic domains. Thin foils for transmission electron microscopy (TEM) observations were electrical-chemical polished at a potential of 40 V using electrolyte with 5% perchloric acid, 25% glycerol, and 70% ethanol at -3 ^{o}C. The thin foils were examined by using an FEI Tecnai G^2 20 TEM and an F30 field-emission-gun TEM equipped with an energy dispersive X-ray (EDX) spectrometer operated at

accelerating voltages of 200 kV and 300 kV, respectively.

4.3 Results and discussions

a. Macrostructure and Vickers Microhardness

The OM metallograph presented in Figure 4-1 shows the microstructure of the steel consisted of ferrite (white-etched phase) and pearlite (dark-etched phase) after isothermal transformation at 650°C for 1 h. A great number of intragranular ferritic grains are formed. The microstructure seems to include both allotriomorphic and idiomorphic ferrite.

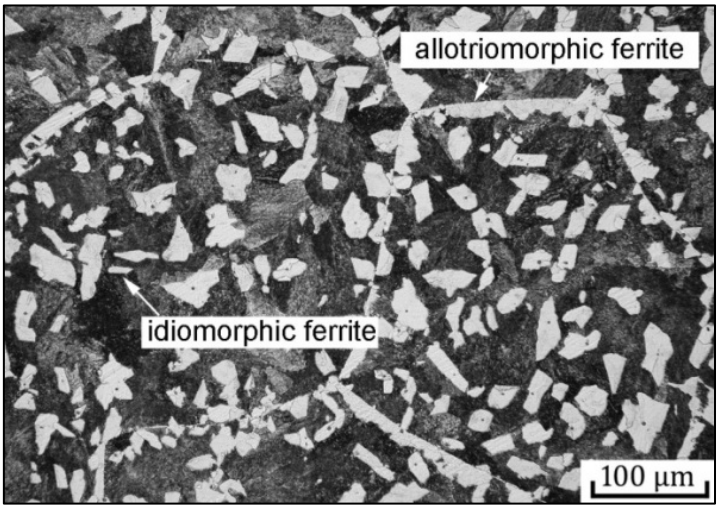

Figure 4-1 The optical micrograph of the microstructure of the sample austenitized at 1200 ^{o}C subsequently isothermally transformed at 650 ^{o}C for 1h.

The term “allotriomorphic” means that the phase is crystalline in internal structure, but not in outward form [39]. Therefore, the allotriomorphic ferrite, as indicated in Figure 4-1, reveals non-equiaxed morphology, determined by bicrystallography of ferrite and austenite. The term “idiomorphic” implies that the concerned phase has faces belonging to its intrinsic crystalline form [39]. In steels, idiomorphic ferrite is understood to be that which has a roughly equiaxed morphology, as indicated in Figure 4-1. The volume fraction of each phase was determined by point counting method: 6 ± 0.5 % for intergranular ferrite; 22 ± 2.3 % for intragranular ferrite; and 72 ± 1.8 % for pearlite. The measured values were Hv 254.2 ± 11.0 and Hv 356.0 ± 9.0 for ferrite and pearlite after isothermal transformation, respectively. Actually, there

was little difference in the hardness of each ferrite isomorph (Hv 249.3 ± 8.2 for intergranular allotrimorphic ferrite, Hv 243.6 ± 12.1 for intragranular allotrimorphic ferrite, Hv 259.4 ± 11.7 for idiomorphic ferrite). There could be a significant contribution from the strengthening of dispersion of carbides to all ferrite isomorphs and maybe pearlite.

b. Precipitation in ferrite

Figure 4-2(a) shows the transition of vanadium carbide (VC) morphology from IP into fibrous form in a single ferritic grain during the austenite-to-ferrite transformation. However, as shown in Figure 4-2(b), the selection area diffraction pattern (SADP) indicates that both interphase-precipitated VC and fibrous VC were NaCl-type carbides. Furthermore, it should be highlighted that the interphase-precipitated VC and fibrous VC had two different variants of the Baker-Nutting (B-N) orientation relationship (OR): $\langle 1\ 1\ 0\rangle_{VC} \parallel \langle 1\ 0\ 0\rangle_{ferrite}$ and $\{0\ 0\ 1\}_{VC} \parallel \{0\ 0\ 1\}_{ferrite}$ with the ferritic matrix.

There are three crystallography variants of B-N OR between NaCl-type carbides and body-centered cubic (bcc) ferrite in steels. In the present analysis, one variant of B-N OR between interphase-precipitated VC and ferrite was $[1\ 1\ 0]_{VC(IP)} \parallel [1\ 0\ 0]_{ferrite}$ and $(0\ 0\ 1)_{VC(IP)} \parallel (0\ 0\ 1)_{ferrite}$, as identified in Figure 4-2(c). In contrast, fibrous VC possessed another variant of B-N OR with ferrite: $[1\ 1\ 0]_{VC(F)} \parallel [0\ 0\ 1]_{ferrite}$ and $(0\ 0\ 1)_{VC(F)} \parallel (\bar{1}\ 0\ 0)_{ferrite}$, as identified in Figure 4-2(d). The two variants imply that there is a 90° rotation in the orientations of the carbide broad planes, $(0\ 0\ 1)_{VC}$. The center dark-field images shown in Figure 4-2(e) and Figure 4-2(f) were illuminated by individual 002 reflections in Figure 4-2(b) of the two B-N variants, respectively. This new finding implies that the nucleation and growth of fibrous VC might be different from those of interphase-precipitated VC because they hold obviously different variants of B-N ORs with ferrite on the ferrite/austenite interface and grow into distinctive carbide morphologies. Edmonds had initially proposed different growth mechanisms for interphase-precipitated and fibrous carbides [3]. However, there has been no direct and striking evidence for his proposition until the present crystallography characterizations by TEM.

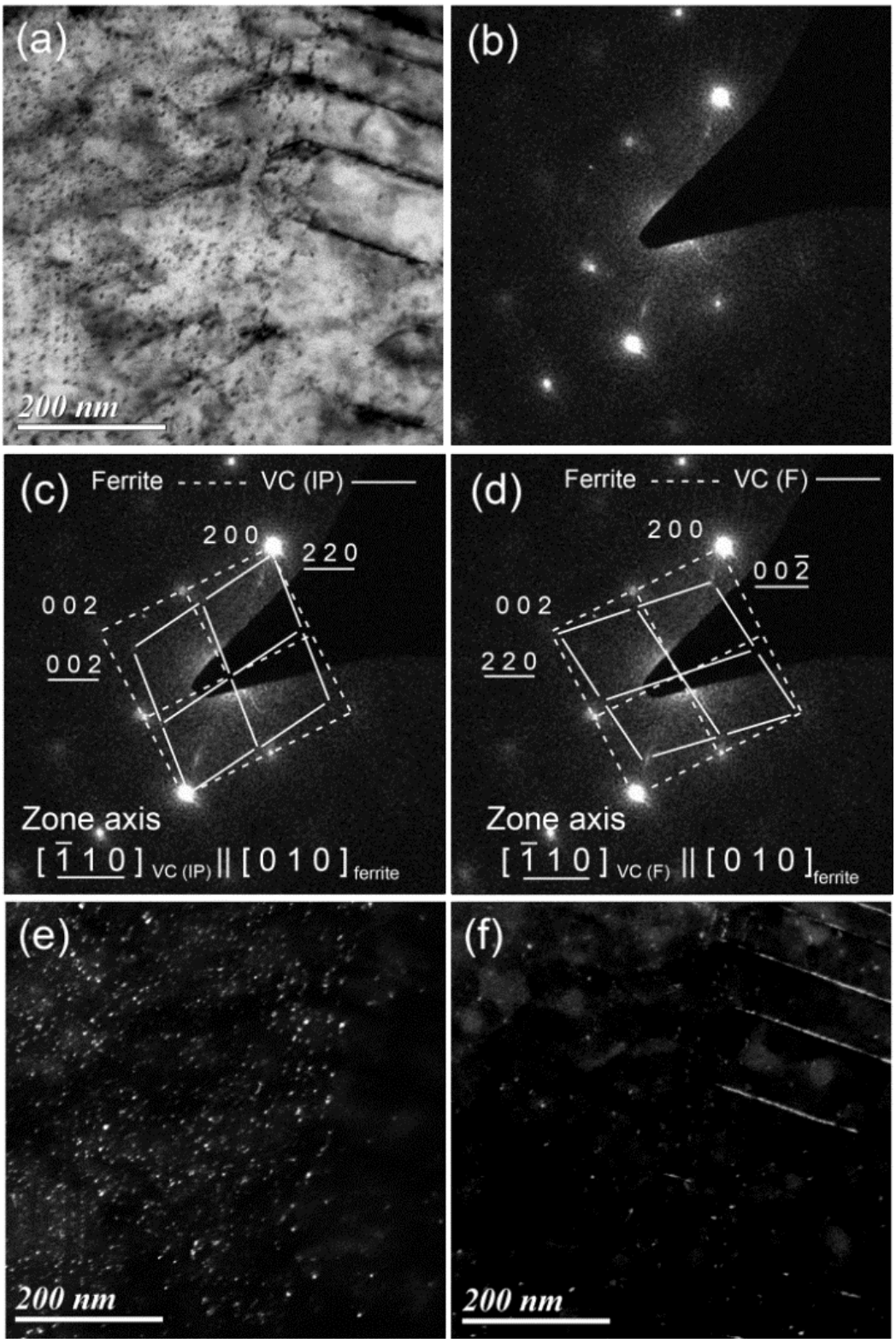

Figure 4-2 TEM analysis on the area containing two carbide aggregates in ferritic matrix. (a) a bright-field image. (b) the SADP, (c) the indexed SADP of the interphase-precipitated carbide, (d) the indexed SADP of the carbide fiber, (e) and (f) the dark-field image illuminated by carbide 002 reflection for the interphase-precipitated carbide and carbide fiber, respectively.

The growth mechanisms of interphase-precipitated and fibrous carbides have been extensively studied and discussed [3, 43]. However, the transition of IP to carbide fiber growth associated with the variant changes of B-N OR has not been reported. Smith and Dunne claimed that the interphase-precipitated MC (TiC, VC, or NbC) plate-like carbide would keep its broad plane as parallel as possible to the terrace plane of the ledged interface during austenite-to-ferrite phase transformation. This provides the shortest diffusion path and minimizes interfacial energy at the interface. However, this rule of variant selection seems not be applied to fibrous carbide, in which carbide also nucleate on the interface. The variant selection of carbide nuclei for fibrous carbide might be resulted from other mechanism. Actually, it has been reported that the fibrous carbide nuclei continue cooperative growth with ferrite into austenite, resulting in a fibrous morphology in ferritic matrix. Such a mechanism is similar to that of pearlite reaction: cementite (Fe_3C) continues cooperative growth with pearlitic ferrite, and Fe_3C follows only one variant of Bagayaski [81] or Pitsch-Petch [82]OR with pearlitic ferrite [83]. The B-N OR always causes MC carbide growth with the broad plane, $\{0\ 0\ 1\}_{MC} \parallel \{0\ 0\ 1\}_{ferrite}$, such that only one variant of interphase-precipitated carbide is generally observed in ferritic matrix. Figure 4-2(a) and Figure 4-2(d), the broad planes of VC fibres, $(0\ \ 0\ \ 1)_{VC(F)} \parallel (\bar{1}\ \ 0\ \ 0)_{ferrite}$, were nearly parallel to its growth direction. However, if the fibrous carbides nucleated on the terrace plane of the interface, two contradictions would arise: (1) they could be interphase-precipitated carbides, and (2) no variant transition would be required. Evidence provided in Figure 4-2(b) implies that the nuclei of fibrous VC have to nucleate in different locations on the interface during the austenite-to-ferrite transformation but not on the terrace plane of the interface, and then grow into fibrous morphology.

Incoherent interface had been suggested to be associated with the formation of fibrous carbides during the austenite-to-ferrite phase transformation [3, 43]. However, Berry *et al.* [42] reported that the VC fibers could hold a Kurdjumov-Sachs (K-S) OR with ferrite. They further concluded that the VC fibers formed on the interface associated with ferrite and austenite by K-S OR. The SADPs given in Figure 4-2(b) show VC fibres follows B-N OR with respect to ferrite. It indicates VC fibers should form on the ferrite/austenite interface which is relatively incoherent. It is recently recognized that IP is related to the ledge mechanism on the terrace planes of the

ferrite/austenite interface associated with irrational OR. The transformation ledge nucleates on a high-indexed incoherent interface and is composed of a terrace plane with relatively low interfacial energy and a high-energy step plane. Hence, the massive nucleations of transformation ledges have to be suppressed if the cooperative transformation of ferrite and carbide is expected to occur on the incoherent interface. It implies that the development of fibrous VC should occur when the driving force of austenite-to-ferrite transformation is low, such that fibrous VC should always take places after interphase-precipiated VC, as shown in Figure 4-3. Therefore, the embryos of VC fibers are supposed to nucleate on a slowed-down incoherent ferrite/austenite interface (not on the terrace plane of an interfacial ledge). The present suggestion rules out the possibility for carbides to form the interphase-precipitaed VC. It is presumed that the nucleation of VC fiber consumes local carbon contents and increases the driving force of austenite-to-ferrite transformation. At the same while, it induces ferrite formation then carbide continuously and cooperatively grows with ferrite, holding one new variant of B-N OR with respect to the ferritic matrix. The cooperative growth process of VC fibre and ferritic matrix is an eutectoid reaction which is controlled by the diffusion of carbide-forming elements, i.e. Ti, Nb, Mo, Cr, and V. Previous studies had suggested that high transformation temperatures, and increasing the addition of Mn, which slowed-down the growth rate of ferrite are the conditions for the development of fibrous carbide.

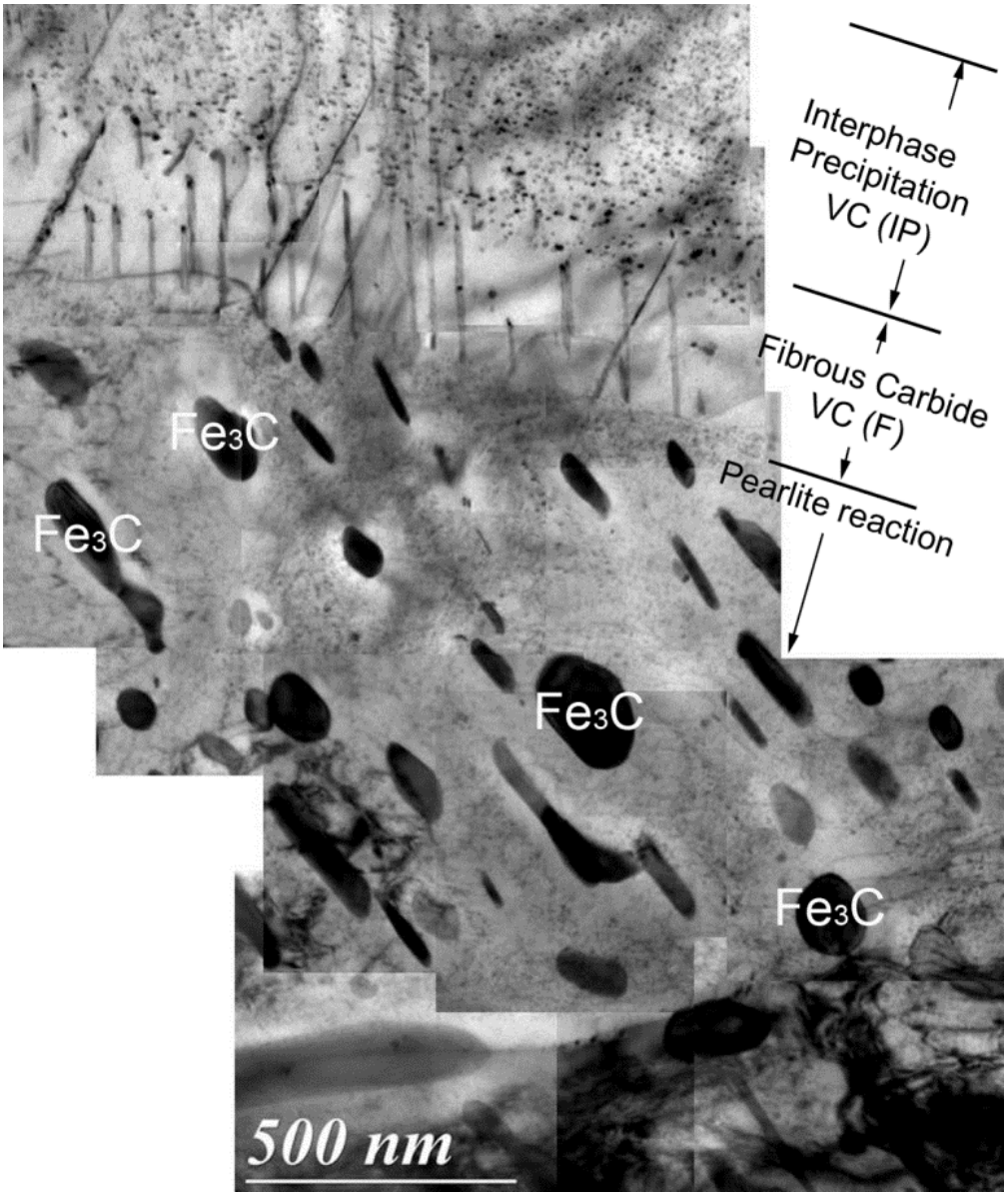

Figure 4-3 Transition of carbide aggregates (interphase precipitation, carbide fiber, and pearlite) during the austenite-to-ferrite transformation.

c. Precipitation in pearlitic ferrite

In addition to intragranular ferrite, both interphase-precipitated VC and fibrous VC were observed in pearlitic ferrite as shown in Figure 4-4. Once again, the interphase-precipitated VC, see Figure 4-4(a) to Figure 4-4(c), was related to pearlitic ferrite by the B-N OR. Parsons and Edmonds suggested that the interphase-precipitated VC nucleate on the terrace plane of the pearlite/austenite interface, which is associated with a rational OR between pearlitic ferrite and austenite during pearlitic transformation. However, Ohmori had pointed out that the pearlite can grow into the austenite without rational OR with pearlitic ferrite [84]. The

pearlitic ferrite can, by epitaxy-like growth, inherit the orientation of the original ferritic grain formed before the pearlite transformation. Yen *et al.* [14] recently reported that IP can occur on the terrace plane of the ledged ferrite/austenite interface, related to an irrational OR between pearlitic ferrite and austenite. Therefore, it is supposed that the IP occurs by ledge mechanism on the interface corresponding to either rational or irrational ORs between pearlitic ferrite and austenite.

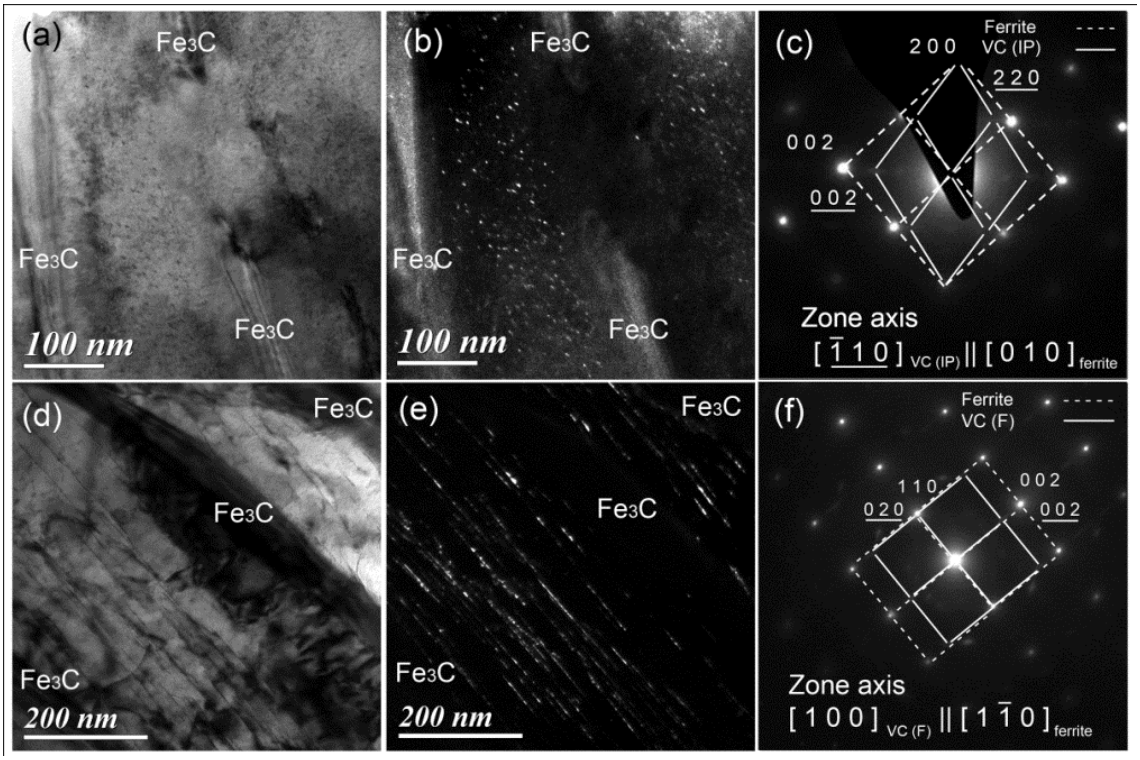

Figure 4-4 The observed interphase-precipitated carbide and carbide fiber in pearlitic ferrite. (a-c) the bright-field, dark-field images and associated SADP of the interphase-precipitaed carbide; (d-f) that for carbide fiber.

The present investigation also observed that the VC fibers precipitated in the pearlitic ferrite, as shown from Figure 4-4(d) to Figure 4-4(e). The fibrous VC was also related to pearlitic ferrite by the B-N OR, as shown in Figure 4-4(f). As elucidated for VC fiber growth in ferrite, the fibrous VC will orient to pearlitic ferrite by B-N OR and keep growing cooperatively with pearlitic ferrite during the pearlitic transformation. The present analysis shows that VC fiber keeps B-N OR with pearlitic ferrite and indicates that it should form on the interface associated with an *irrational* OR between pearlitic ferrite and austenite as well.

For carbide fiber growth in pearlitic ferrite, it can be expected that the

thermodynamic driving force for Fe_3C formation is lower than that for VC. As a consequence, the carbide fiber formation would precede the pearlite formation. It also implies if a slower transformation pearlite/austenite front presents, it is possible for VC fiber to form in the pearlitic ferrite between cementite lamella, as shown from Figure 4-4(d) to Figure 4-4(f). Moreover, Fe_3C formation consumes great amounts of carbon; it further causes nucleation of ledges on the transformation front. In such a case, as displayed in Figure 4-4(a) and Figure 4-4(c), IP carbides can form in pearlitic ferrite. The mechanisms to form interphase-precipitated VC and fibrous VC are similar to that one in ferrite. The above illustrations are well-consistent with the model proposed by Parsons and Edmonds [52] to describe the interphase-precipitated VC in pearlitic ferrite. However, not every pearlite colony was found to have alloy carbides (interphase-precipitated or fibrous VCs) in pearlitic ferrite. The criterion is determined by (1) the interfacial structure at pearlite/austenite interface, (2) the consumption of the carbon by the formation of Fe_3C, and (3) the diffusion rate of carbide forming elements. However, the proposition of diffusion and consumption of carbon and alloy elements during the transformation is beyond the scope of the present TEM investigation.

A high-resolution TEM (HRTEM) lattice image was taken from a region in which VC fibers precipitating in ferrite (Figure 4-5). The diffractogram generated by two-dimensional fast Fourier transform of the lattice image is given in Figure 4-5(b). It reveals, once again, that the VC fiber has B-N OR with respect to the ferritic matrix along a zone axis $[1\ 0\ 0]_{\text{ferrite}} \parallel [1\ \bar{1}\ 0]_{\text{carbide}}$ $[100]_{\text{ferrite}} // [1\bar{1}0]_{\text{carbide}}$. The overlap of carbide and ferrite lattices contributes the moiré fringes, which can be used to determine the size of carbides. The fibrous VC is about 3.06 nm in thickness and has a great aspect ratio (length/width), demonstrating a slender morphology unlike that of the plate-like interphase-precipitated carbides. For the interface of interphase precipitation or supersaturated precipitation, the broad plane of the MC carbide is the broad face of the carbide platelet. In other words, the carbide growth rates in directions on the broad face are approximately equivalent under B-N OR. However, the face of the fibrous VC is also the broad plane, $(1\ 0\ 0)_{\text{VC(F)}} \parallel (1\ 0\ 0)_{\text{ferrite}}$, as shown in Figure 4-5(a), strongly suggesting that the growth rates of the advancing and side directions of VC fiber are quite different, due to the nature of cooperative growth with ferrite. The Nano-Probe EDX spectrum of the VC fiber is displayed in Figure

4-5(c), and its chemical composition is mainly vanadium.

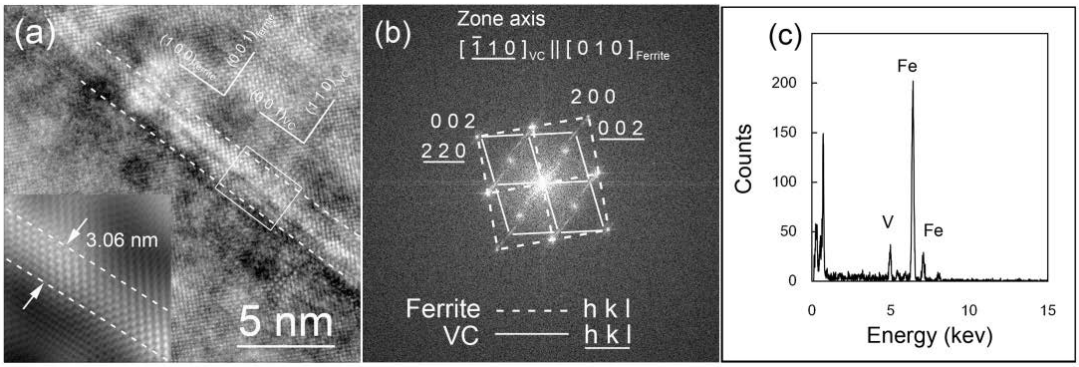

Figure 4-5 The HRTEM image of the carbide fiber in ferrite. (a) the lattice image, (b) the FFT diffractogram, and (c) the EDS analysis of carbide fiber.

4.4 The conditions for the development of fibrous carbide

The present investigation provides some new directions to improve our understanding about the morphologic evolution of carbides. Furthermore, it helps us to clarify the conditions for the development of fibrous carbide. It has been pointed out the chemical composition of steel, the transformation temperature, the coherency of interface are the factors on determining carbide morphologies, which are summarized as follows:

a. Effects of the transformation temperature

Based on the microscopic observations and diffusion considerations, as the transformation temperature is lowered, interphase precipitation becomes dominant on the basis of minimizing interfacial energies and maximizing diffusion efficiency. It makes the carbide that the carbide platelet would be as parallel as to the terrace plane, leading to interphase precipitation. On the contrary, carbide fiber would be originated from a curved interface. Edmonds addressed that at higher transformation temperature, the habit plane of carbide does not have to be on the terrace plane because the mobility of solute atom is able to diffuse in the direction perpendicular to the interface as the transformation temperature is elevated, and carbide fiber is then developed. However, Barbacki and Honeycombe proposed that the carbide fiber is favored as the transformation temperature is lowered. According to the ledge mechanism proposed by Honeycobme, the terrace plance of interphase precipitation is supposed to be

semi-coherent, followed $\{1\ 1\ 0\}_{\alpha} \parallel \{1\ 1\ 1\}_{\gamma}$ orientation relationships. As the transformation temperature is lowered, the solute atom tends to diffuse along an incoherent interface to maximum the diffusion efficiency, which is perpendicular to the ferrite/austenite interface.

Cahn [85] had pointed out that the ledge mechanism of transformation would occur at higher transformation temperatures because the lower transformation driving force at higher transformation temperatures is unable to make the overall interface to advance uniformly. According to this proposition, it concludes that the carbide fiber would be dominant at lower transformation temperatures because the driving force of transformation is large enough. However, this obviously deviates from the experimental observations of the carbide aggregates. The contradiction between Cahn's proposition and microscopic observations has not been highlighted.

b. The effect of interface coherency

The deviation indicated in the previous point implies that the crystallographic and coherency of interface would not be the main factors to determine carbide morphologies. The crystallographic aspects had been discussed by Law *et al* [86]. Miyamoto and Yen have shown that a ledged interface can even be developed from an incoherent interface. However, the original ferrite/austenite interface characteristics are difficult to retain because the austenite would transform into martensite. Kitahara *et al.* had developed a method to re-construct the orientation of the interface by using the inverse orientation matrix [87, 88]. An area with ferrite and martensite was scanned by EBSD clarify this issue, as shown in Figure 4-6. The analysis of the misorientation of ferrite/austenite interface is according to the work of Furuhara and Miyamoto [89, 90]. The sample is a Fe-0.36C-1.35Mn-0.33V-0.33Si alloyed steel isothermally transformed at 650 ^{o}C for 3 min. It can be seen that allotriomorphic ferrite and idiomorphic ferrite were transformed from austenite with this grain. The misorientation of ferrite/austenite interface is revealed by OIM-software. SEM was then used to examine the microstructure of each ferrite grain (allotriomorphic and idiomorphic), as shown in Figure 4-7. Only the ferrite labeled as i3 was found to have carbide fibers, and no carbide was observed in the rest ferrite grains. By referring to the proposition for carbide fiber development, it is expected that the misorientation of i3 is supposed to be larger than other ferrite grains. The misorientaiton map presented

in Figure 4-7(a) indeed shows that the i3 actually has a larger misorientation angle (~ 40°). However, for other grains which exhibit large misorientation angles (a3 and a5 for examples), carbide fibers did not appear. As a consequence, it can conclude that the coherency of the ferrite/austenite interface does not influence greatly on the determination of carbide morphology. This is complementary with the findings presented by Yen [14], Okamoto [91] and Miyamoto [51], which showed that a ledge interface does not have to be semi-coherent.

c. The alloying elements

Alloying elements which influence the transformation kinetics can be used to alter the carbide morphologies as well. Mn and Ni are generally recognized to slower the rate of austenite to ferrite transformation and had been found in increasing the amount of carbide fibers in alloy steels [5]. However, increasing in vanadium content did not promote the volume fraction of VC fibers. No attempts had been made on the competition between interphase precipitated carbides and fibrous carbides by varying carbon or vanadium contents. The effects of carbon and solute contents on the development of fibrous carbides are still unclear.

The conditions and features of carbide fiber proposed among studies have now are presented in Table 2-1. Nevertheless, the carbide fibers in Fe-V-C steels are less studied. Detailed studies on the development of fibrous carbide have been few in number, and direct evidence of the propositions is still lacking, particularly in terms of how fibrous carbides nucleate and grow.

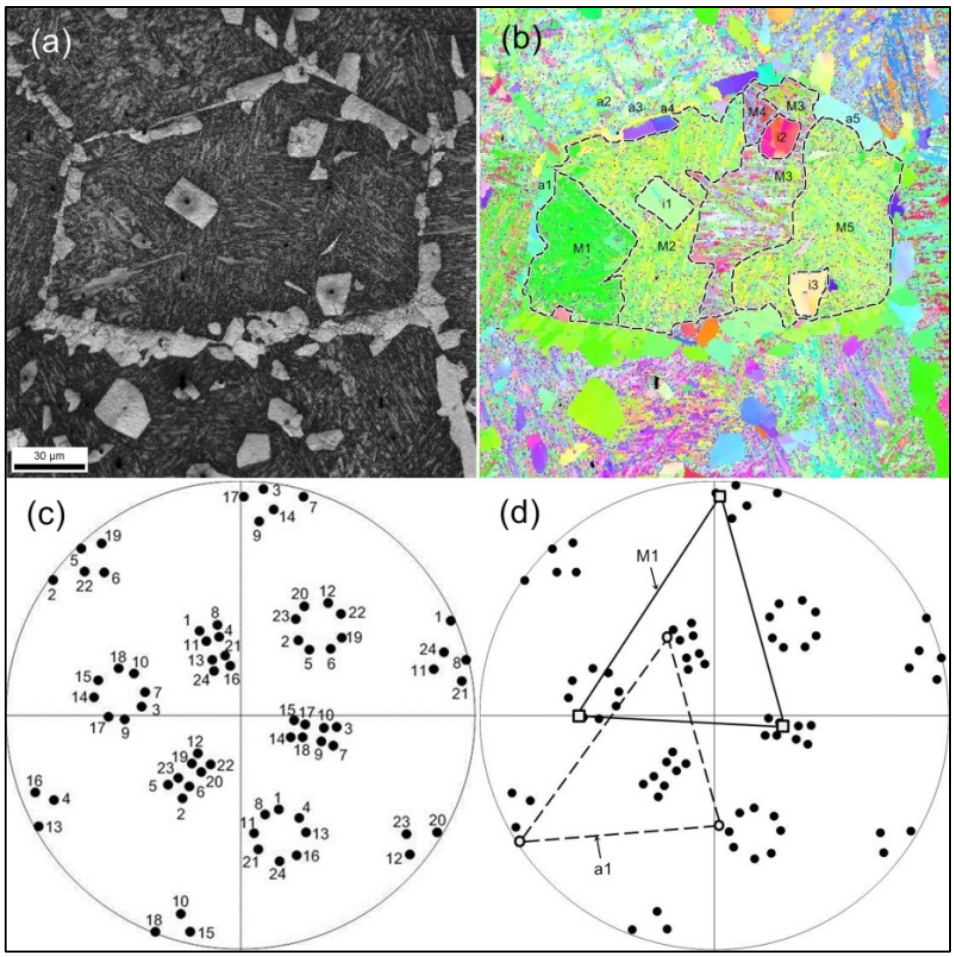

Figure 4-6 (a) The selected area for EBSD analysis showing ferrite allotriomorphs, idiomorphs, and martensite; (b) Orientation map of the selected area; (c) a stereographic projection showing the martensite variants transformed from this prior austenite grain, and (d) coupling with measured martensite (M1) and ferrite (a1) orientations.

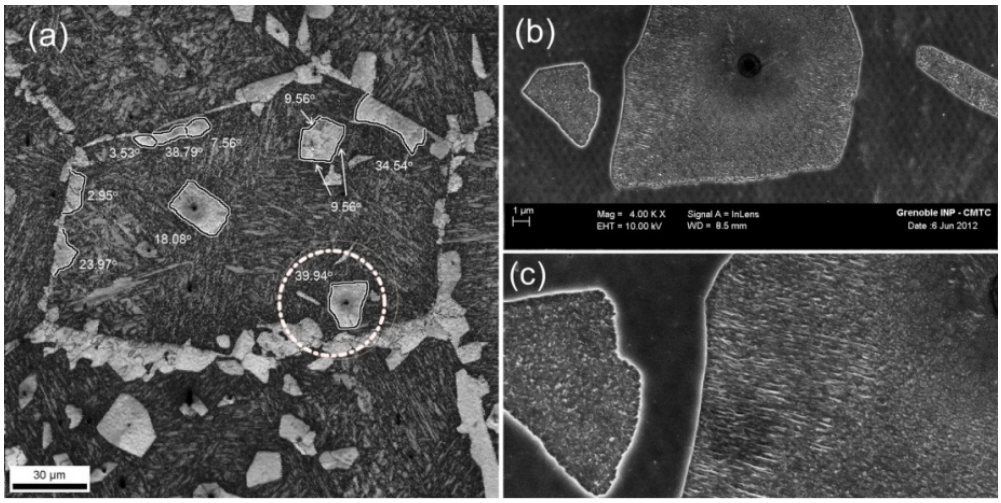

Figure 4-7 (a) A micrograph showing the calculated deviation angle of ferrite grains; the ferrite with carbide fiber is labeled, (b) a SEM image of the labeled ferrite grain, and (c) a larger magnification of (b).

4.5 Conclusion

In summary, the present study discusses in detail a mechanism of alloy carbide formation, particularly for the development of fibrous VC based on extensive TEM investigations. The IP usually occurs via the ledge mechanism. Importantly, the variant transition is always observed as the carbide morphology changes from interphase precipitation to carbide fibre growth. It supports the proposition that the embryos of fibrous carbides nucleate on a slowed-down incoherent ferrite/austenite or pearlite/austenite interface (not on the terrace plane of an interfacial ledge). Then carbide and ferrite continue the cooperative growth and hold another variant of the B-N OR, resulted in an elongated morphology. The cooperative growth of ferrite and fibrous carbide is a eutectoid reaction, controlled by the diffusion of carbide-forming elements, i.e. titanium, niobium, vanadium, molybdenum, or chromium. This proposed mechanism further holds for carbide precipitation in pearlitic ferrite, and it is also consistent with previous suggestions and experiments.

The conditions for fibrous carbide development are discussed. Previous studies indicated that the carbide morphology is a function of transformation temperature and the nucleation of fibrous carbide is on an incoherent interface. The new experimental observations have shown that

(1) The change in carbide morphology does not actually need to alter the transformation temperature.
(2) The coherency of interface would not be the dominant factor in determining the carbide morphology.

Based on these two clarifications, it may be concluded that the occurrence of fibrous carbide is indeed an issue of the kinetic of austenite-to-ferrite transformation. The mobility of interface is supposed to be responsible for the carbide morphology determination, which is eventually beyond the scope of microscopic observations.

Chapter 5

The superledge model for interphase precipitation

5.1 Introduction

It is well-established that the interphase precipitation has to be accomplished together with the ledge mechanism of austenite-to-ferrite transformation. As a consequence, both phenomena should be strongly coupled. The ferrite and carbide nucleation interacts and the driving force for austenite-to-ferrite transformation may affect the carbide aggregate formation. The ferrite and carbide nucleation rates and the driving force for austenite-to-ferrite transformation at one time in order to describe correctly this special carbide aggregate. However, by referring Table 2-2, it obviously shows that this point is NOT incorporated in the existing models, in spite of their ability to describe experimental data. It is worth noticing that the experimental data, sheet spacing, used in the numerical models was generally measured from the samples transformed at a high transformation temperature (> 700 ^{o}C), as listed in Table 5-1. The availability of these models at lower transformation temperature has not been examined. Lagneborg and Zajac had shown great deviations of their model with the measured sheet spacing and concluded that partition of solute at the interface transited from local equilibrium into paraequilibrium. This deviation was also observed in the work of Li and Todd but they did not provide the explanations.

The present superledge model aims to provide a new approach to describe interphase precipitation in a coherent manner. The ledge mechanism of austenite-to-ferrite transformation is strictly followed in superledge model. Furthermore, it tries to relate the characteristic features of interphase precipitation

with thermodynamic and kinetic quantities; for example, ferrite and carbide driving forces controlling their nucleation rates. The driving force for austenite-to-ferrite transformation and the diffusion coefficients are the main ingredient of the present model. The calculated results will be compared to the existing models and the temperature dependence of sheet spacing will be discussed.

Table 5-1 The experimental data used for supporting the proposed numerical models

References	Alloy in wt%	Austenitization at	Isothermally transformed at
Batte and Honeycombe [37]	Fe-0.20C-1.04V-0.023Nb	1200 ^{o}C	825 ^{o}C
			800 ^{o}C
			775 ^{o}C
			750 ^{o}C
			725 ^{o}C
	Fe-0.15C-0.75V-0.02Nb and Fe-0.09C-0.48V-0.016Nb		830 ^{o}C
			806 ^{o}C
			780 ^{o}C
			755 ^{o}C
			730 ^{o}C
Wilyman and Honeycombe [92]	Fe-0.20C-0.96V-1.5Ni		700 ^{o}C
			650 ^{o}C
	Fe-0.21C-0.96V-0.97Al		750 ^{o}C
			700 ^{o}C
			650 ^{o}C
Balliger and Honeycombe [60]	Fe-0.05C-0.27V-0.0002N	1150 ^{o}C	810 ^{o}C
			790 ^{o}C
			760 ^{o}C
			740 ^{o}C
			720 ^{o}C

5.2 The derivations

a. Assumptions

The typical microstructure of interphase precipitation has been shown elsewhere

in this thesis. The main characteristic features we are interested in are illustrated in Figure 5-1.

The following assumptions are made for the superledge model development:

a. Carbon enrichment in austenite during $\gamma \rightarrow \alpha$ transformation is neglected since it is considered either large austenitic grains and/or low carbon content.

b. The carbides are spherical in shape.

c. The α ledge density is at a dynamic steady-state condition.

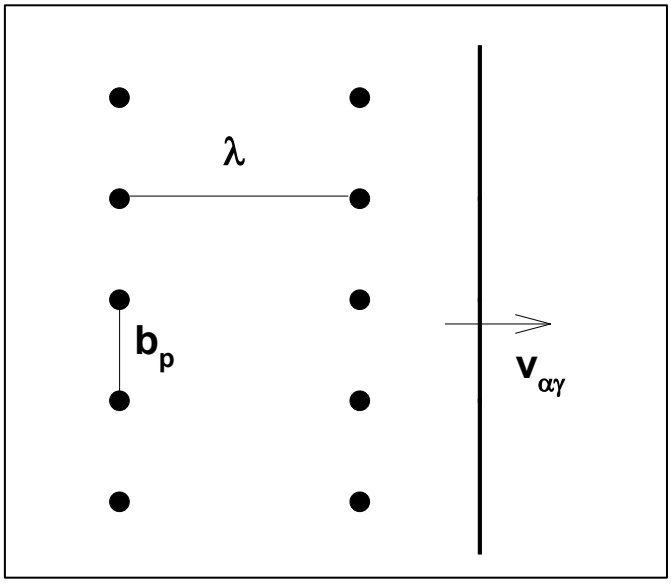

Figure 5-1 The characteristic features of interphase precipitation focused in the present superledge model.

The superledge model can be subsequently divided into five steps: (1) α unit ledge forms on the interface which has already carbides on it; (2) α unit ledge moves laterally and is then pinned by the presence of carbide; (3) a new α unit ledge forms on the top of the base ledge, increasing the ledge height; (4) when the stacking of unit ledges into a superledge reaches a critical height, the superledge unpins from carbides and moves laterally, merging the neighboring superledges; (5) the α/γ interface advances forward until another precipitation cycle occurs. These

steps are schematically illustrated in Figure 5-2.

b. The classical ledge mechanism of austenite-to-ferrite transformation

Let's start from a α/γ interface without any carbide. Using the interface mobility, *M*, the interface ledge velocity, v, is given by

$$v = M\Delta G \tag{5-1}$$

where ΔG is the driving force for $\gamma \rightarrow \alpha$ transformation.

The overall interface velocity of a ledged interface, $v^{\circ}_{\alpha\gamma}$, depends on the ledge spacing, *b*, and its height. Under a steady state assumption, the nucleation rate J_B and the ledge spacing are related:

$$J_B = \frac{1}{b^2\tau} \tag{5-2}$$

where τ is the characteristic time for steady-state ledge-wise growth, which is defined as

$$\tau = \frac{b}{v} \tag{5-3}$$

Defining *a* as the ledge height, the conversion between overall interface velocity and ledge velocity can be formulated by

$$v^{\circ}_{\alpha\gamma} = v\frac{a}{b} = \frac{a}{\tau} \tag{5-4}$$

For a unit α ledge, the magnitude of a is taken as the lattice parameter of α.

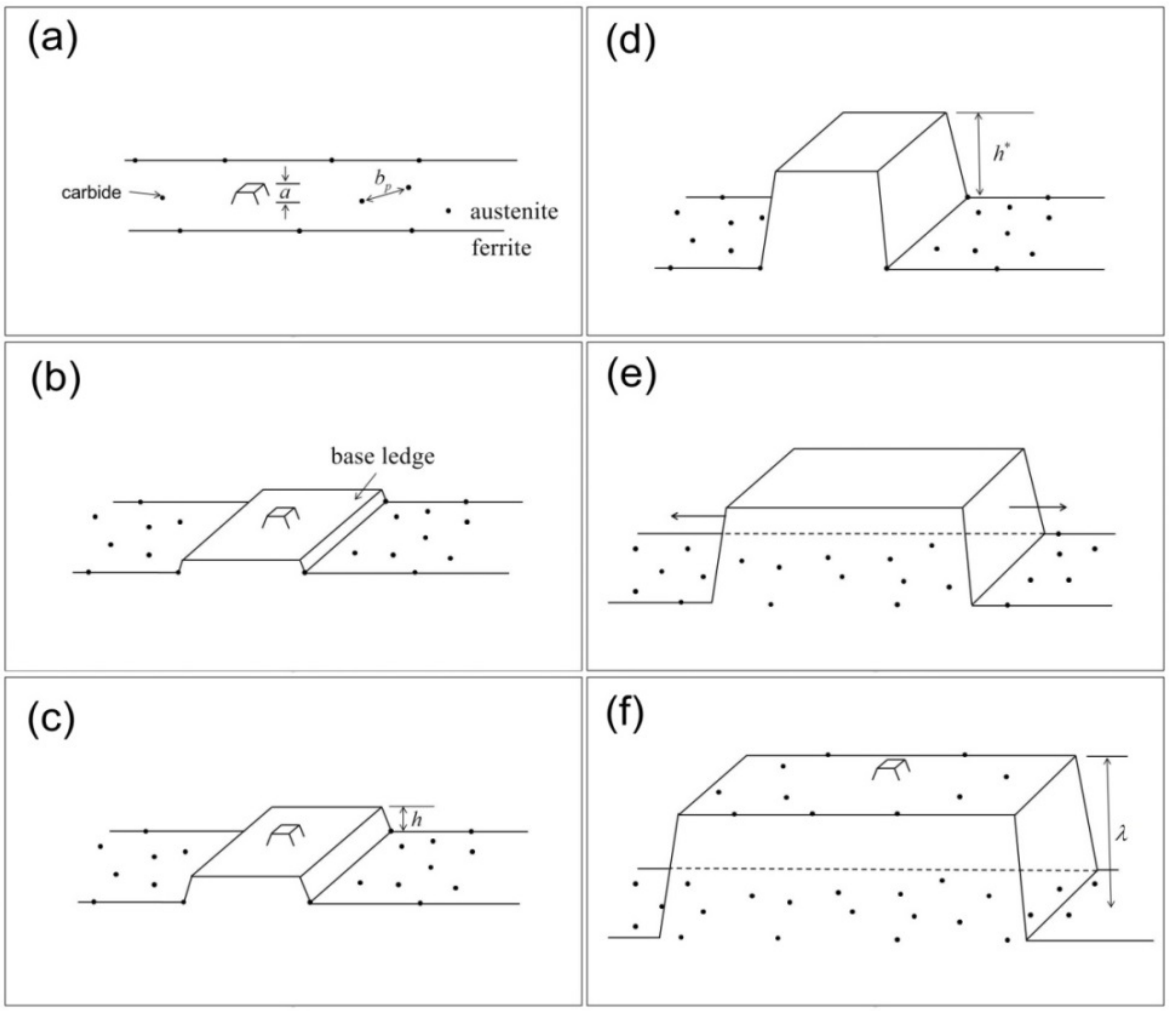

Figure 5-2 The proposed sequence of the development of a superledge originated from the ferrite/austenite interface. (a) a unit ledge forms on an interface with carbides; (b) the first ledge moves laterally and is pinned by carbides, and then another unit ledge nucleates on the top of it; (c-d) the ledge continues to increase its height to unpin from carbides; (e) the superledge is able to move laterally again and then merge the neighboring superledges, and (f) the overall interface advances until carbides precipitate on the interface again, completing a cycle of interphase precipitation.

c. The interaction of carbide with the growing ferrite phase

The competition between transformation driving force and carbide pinning force is the core of the present superledge model. In the case of interphase precipitation, the presence of carbides pins the lateral movement of ledges, leading v to be temporarily zero. A superledge is then built up, and unpins from carbides as it reaches a critical height, h^*. The present model requires that the spacing between ledge nuclei, b, is much larger than the spacing between precipitates, b_p, and that the sheet spacing, λ, is larger than the critical ledge height, h^*

$$b \geq b_p \tag{5-5}$$

$$\lambda > h^* \tag{5-6}$$

. Defining τ_λ as the time for the interface to advance a distance of λ, the overall velocity of an interface with IP is given by

$$v_{\alpha\gamma} = \frac{\lambda}{\tau_\lambda} \tag{5-7}$$

τ_λ is equivalent to the time to complete one cycle of IP which can be further be divided into three sequences : (1) the waiting time to build a critical superledge, τ_w; (2) the time for unpinning superledge to merge neighboring superledges, τ_f, and (3) the time for the interface to move forward until next precipitation row is formed. It can be formulated as

$$\tau_{\lambda} = \tau_{w} + \tau_{f} + \frac{\lambda - h^{*}}{a}\tau \tag{5-8}$$

τ_{w} can be determined by considering repeated ledge nucleation on the top of the base ledge, J_T, which is given by

$$J_T = \frac{1}{b_p^2 \tau_n} \tag{5-9}$$

where τ_n is the time needed for a unit ledge to nucleate on the top of the base ledge. Using steady-state assumption and combining with equation (5-2), it yields

$$\tau_n = \left(\frac{b}{b_p}\right)^2 \tau \tag{5-10}$$

This newly unit ledge then passes over on the top of base ledge with a distance of b_p. The required time, $\tau_{\circ}$, can be deduced from steady-state assumptions

$$\tau_{\circ} = \frac{b_p}{b}\tau \tag{5-11}$$

The condition presented in equation (5-5) leads to $\tau_n >> \tau > \tau_{\circ}$. It means that most of time is spent on the stage of α ledge nucleation, which reasonably leads the τ_w to be considered as the summation of the required time to reach h^*

$$\tau_w = \frac{h^* - a}{a}\tau_n \tag{5-12}$$

Because of $h^* >> a$, it can be further simplified

$$\tau_w = \frac{h^*}{a}\tau_n = \frac{h^*}{a}\left(\frac{b}{b_p}\right)^2 \tau \tag{5-13}$$

τ_f can be rationalized as follows. Describing the motion of a superledge of height h as resulting from the motion of successive unit ledges of height a allows to express the effective mobility of a ledge with height *h*, M_h, in terms of *M* the unit ledge mobility

$$M_h = \frac{a}{h}M \tag{5-14}$$

In order to simplify the system, the superledge presenting on α/γ interface are assumed to have the same height; therefore, the velocity of every superledge is the same. When unpinning occurs ($h = h^*$), it leads to

$$v^* = M_h \Delta G = \frac{a}{h^*} M \Delta G \tag{5-15}$$

Then the flight time necessary to merge two unpinned superledges can be obtained from

$$v^* \tau_f = \frac{l - b_p}{2} \tag{5-16}$$

where l is defined as the spacing of superledges. Using equations (5-4) and (5-15), τ_f, becomes

$$\tau_f = \frac{l - b_p}{2ab} h^* \tau \tag{5-17}$$

Compared τ_f to τ_w, it suggests that $\tau_w > \tau_f$ could be generally fulfilled for the cases of interests because of $b >> b_p$. Neglecting the flight time in the subsequent analysis, τ_λ becomes

$$\tau_\lambda = \left[(\lambda - h^*) + h^* \left(\frac{b}{b_p} \right)^2 \right] \frac{\tau}{a} \tag{5-18}$$

Combining equations (5-7) and (5-18), the net global velocity of the ferrite/austenite interface $v_{\alpha\gamma}$ can be obtained as

$$v_{\alpha\gamma} = \frac{v_{\alpha\gamma}^o}{\left(1 - \frac{h^*}{\lambda}\right) + \frac{h^*}{\lambda}\left(\frac{b}{b_p}\right)^2} \tag{5-19}$$

$v_{\alpha\gamma}$ now has been successfully expressed in terms of λ, b_p, and h^* and shows that $v_{\alpha\gamma}$ is independent of superledge spacing. Equation (5-19) also reveals the effect of carbide precipitation on the overall interface velocity. Compared it to equation (5-7), it shows that the overall interface velocity is slowed down by carbide

precipitation.

We have now to derive equations to estimate the features of interests, λ, b_p, and h^*.

The ledge is pinned by carbides, when the transformation driving force, ΔG is smaller than the pinning force, ΔG_{ZP} exerted by carbides. Then:

$$\Delta G_{ZP} \geq \Delta G \tag{5-20}$$

The pinning pressure is considered is a function of *h:* indeed the precipitates exert their pinning force at the root of the super ledge and this force is to be distributed on the whole height of the ledge. In that case:

$$\Delta G_{ZP} = \Delta G_{ZP}^{o} \frac{R}{h} \tag{5-21}$$

Here ΔG_{ZP}° is the nominal pinning pressure depending on b_p and carbide radius, *R*, via

$$\Delta G_{ZP}^{o} = \frac{\pi \sigma_{\circ} R}{b_p^2} \tag{5-22}$$

where $\sigma_{\circ}$ is the α/γ interfacial energy. Note that this expression differs from the classical Zener pinning one because the precipitates are by construction lying of the interface while in the case of Zener they are randomly sampled by the interface.

To go further, we have to estimate in a simple way the characteristics of the precipitation. Representing a particle row with a slab of precipitate of thickness, δ,

and assuming a parabolic growth, we have

$$\delta = \frac{c_p^\circ}{c_p}\sqrt{Dt} \tag{5-23}$$

where c_p° is the nominal solute concentration of carbide forming element, c_p is the solute concentration of precipitate, and D is the boundary diffusivity of carbide-forming element. Therefore, the particle radius can be obtained from

$$\delta b_p^2 = \frac{4\pi}{3}R^3 \tag{5-24}$$

From which

$$R = \left(\frac{3c_p^\circ b_p^2}{4\pi c_p}\right)^{1/3}(Dt)^{1/6} \tag{5-25}$$

Setting $1/\lambda b_p^2$ as the number of precipitates per unit volume, each precipitate having a volume of $\frac{4}{3}\pi R_{unpin}^3$. The resulting volume fraction, f_p, is therefore given by

$$f_p = \frac{1}{\lambda b_p^2}\frac{4\pi}{3}R_{unpin}^3 \tag{5-26}$$

Assuming that all alloying elements are partitioned to precipitates, we obtain

$$f_p = \frac{V_p}{V_{Fe}}c_p^\circ \tag{5-27}$$

where V_p and V_{Fe} are the molar volume of precipitation and iron matrix, respectively. Then, the radius of precipitates at the moment of unpinning can be expressed as

$$R_{unpin} = \left(\frac{3Vc_p^{\circ}\lambda b_p^2}{4\pi} \right)^{1/3} \tag{5-28}$$

where $V = V_p / V_{Fe}$.

The ledge height is growing at a constant rate. At time *t*, the ledge height h is given by equation (5-13) which can be rewritten:

$$h = a\left(\frac{b_p}{b} \right)^2 \frac{t}{\tau} \tag{5-29}$$

Replacing equation (5-29) and into equation (5-21), the pinning force per unit surface ΔG_{ZP} as a function of time is:

$$\Delta G_{ZP} = \frac{\pi^{1/3}\sigma_o b^2 \tau}{atb_p^{8/3}} \left(\frac{3Vc_p^{\circ}\lambda}{4} \right)^{2/3} \tag{5-30}$$

At the time $t = t^*$ which the superledge reaches its critical height and unpins from carbides, the driving force of transformation is equal to the pinning force due to carbides. Then:

$$\Delta G_{ZP} = \Delta G \tag{5-31}$$

The time t^* for ledge to reach its critical height, h^*, can be written by rearranging equation (5-29)

$$t = t^* = \frac{h^*}{a}\left(\frac{b}{b_p}\right)^2 \tau \tag{5-32}$$

And h^* is expressed as

$$h^* = \frac{\pi^{1/3}\sigma_o}{b_p^{2/3}\Delta G}\left(\frac{3Vc_p^{\circ}\lambda}{4}\right)^{2/3} \tag{5-33}$$

The only unknown in the equation is the sheet spacing. To derive the equation for λ, the nucleation conditions for the precipitates have to be analyzed. For sake of simplicity, one may assume that a sufficient nucleation rate for the formation of a new sheet of particles is attained in the limit where the solute concentration approaches some critical value, e.g. c_{crit}. Then, one may approximate λ as the diffusion distance during the time τ_λ, then:

$$\lambda = \frac{c_{crit}}{c_p^{\circ}}\sqrt{D\tau_\lambda} \tag{5-34}$$

By replacing equation (5-34) into equation (5-18) and using equations (5-5) and (5-33), the expression of sheet spacing now can be further simplified as

$$h^* = \frac{\pi^{1/3}\sigma_o}{b_p^{2/3}\Delta G}\left(\frac{3Vc_p^{\circ}\lambda}{4}\right)^{2/3} \tag{5-35}$$

Subsequently, the interface velocity becomes:

$$v_{\alpha\gamma} = \frac{\lambda}{h^*}\left(\frac{b_p}{b}\right)^2 v_{\alpha\gamma}^o = \frac{c_{crit}^{1/2}b_p^2}{c_p^{\circ}}\left(\frac{D}{\pi}\right)^{1/4}\left(\frac{aJ_B\Delta G}{\sigma_{\circ}}\right)^{3/4}\left(\frac{4}{3V}\right)^{1/2} \tag{5-36}$$

Setting in as a first approximation, $c_{crit} = c_p^{\circ}$, the final forms of equations providing sheet spacing and overall interface velocity can be written as:

$$\lambda = \frac{\pi^{1/4}c_p^{\circ 1/2}}{b_p^2}\left(\frac{D\sigma_o}{aJ_B\Delta G}\right)^{3/4}\left(\frac{3V}{4}\right)^{1/2} \tag{5-37}$$

$$v_{\alpha\gamma} = \frac{b_p^2}{c_p^{\circ 1/2}}\left(\frac{D}{\pi}\right)^{1/4}\left(\frac{aJ_B\Delta G}{\sigma_{\circ}}\right)^{3/4}\left(\frac{4}{3V}\right)^{1/2} \tag{5-38}$$

The particle spacing, b_p, is considered as the result from α and carbide nucleation competition. At the critical concentration under steady-state assumption, the particle nucleation rate, J_p, is obtained from equation (5-2)

$$J_B b^2 = J_P b_p^2 \tag{5-39}$$

With equations (5-1) and (5-4), b can be expressed as

$$b = \left(\frac{M\Delta G}{J_B} \right)^{1/3} \tag{5-40}$$

such that the particle spacing in one sheet of IP is given by

$$b_p^2 = \frac{J_B^{1/3} (M\Delta G)^{2/3}}{J_p} \tag{5-41}$$

The remaining quantities to be determined to have a closed form model are the nucleation rate for the precipitates and for the ledges in the ferrite/austenite interface. Now, we have successfully derived the equations for the characteristic features of interphase precipitation. Table 5-2 summarizes the most important equations in the present thesis.

Table 5-2 A summary of the equations used in the calculations

Descriptions	Equations
Ferrite ledge nucleation rate	$J_B = N_\circ^\alpha \exp(-\frac{Q^\alpha}{RT}) \exp(-\frac{\Delta G_\alpha^*}{kT})$
Carbide nucleation rate	$J_p = N_p^\circ Z \beta^* \exp(-\frac{\Delta G_p^*}{kT})$
Ledge velocity	$v = M \Delta G$
Sheet spacing	$\lambda = \frac{\pi^{1/4} c_p^{\circ 1/2}}{b_p^2} \left(\frac{D\sigma_o}{aJ_B \Delta G} \right)^{3/4} \left(\frac{3V}{4} \right)^{1/2}$
Overall interface velocity	$v_{\alpha\gamma} = \frac{b_p^2}{c_p^{\circ 1/2}} \left(\frac{D}{\pi} \right)^{1/4} \left(\frac{aJ_B \Delta G}{\sigma_\circ} \right)^{3/4} \left(\frac{4}{3V} \right)^{1/2}$
Particle spacing	$b_p^2 = \frac{J_B^{1/3} (M\Delta G)^{2/3}}{J_p}$

5.3 Parameters used for calculations

For the predictions of characteristics of IP, nucleation rates, J_B and J_p, for ledge formation and carbide precipitation, the intrinsic mobility, *M,* of the α/γ interface and the boundary diffusion coefficient of alloying element, *D* have to be determined.

These parameters that play a key role on the evolution of IP characteristics are described in this section. A number of considerations are proposed in order to get few adjustable parameters.

5.3.1 The ferrite and carbide nucleation rates

It has been shown that the features of interests of IP described by equations (5-37), (5-38), and (5-41) are related by carbide and α ledge nucleation rates, J_p, J_B, and driving force for $\gamma \rightarrow \alpha$ transformation, ΔG. The value of ΔG can be calculated by using a thermodynamic database such as TCFE6 of Thermo-Calc.

The classical nucleation theory is used to determine J_p and J_B. The α ledge nucleation rate can be expressed as [93].

$$J_B = N_{\circ}^{\alpha} \exp(-\frac{Q^{\alpha}}{RT}) \exp(-\frac{\Delta G_{\alpha}^{*}}{kT}) \tag{5-42}$$

where $N_{\circ}^{\alpha}$ is the number of α ledge nucleation site on the α/γ interface, which is usually considered as a fitting parameter, Q^{α} is the activation energy for α

nucleation. ΔG_{α}^{*} is the maximum of Gibbs energy associated with the formation of a nuclei. By considering a 2D α ledge nucleation model, the nucleation energy can be written as

$$\Delta G_{\alpha}^{*} = \frac{7\sigma^{2}}{4a\Delta G} \tag{5-43}$$

The carbide nucleation rate, J_p, can be determined by a similar way and can be given by [94]

$$J_{p} = N_{\circ}^{p} Z \beta^{*} \exp(-\frac{\Delta G_{p}^{*}}{kT}) \tag{5-44}$$

where $N_{\circ}^{p}$ is the number of carbide nucleation site on the phase boundary, Z is the Zeldovitch factor, β^{*} is the adsorption frequency, and ΔG_{p}^{*} is the maximum energy change associated with carbide nucleation [93].

5.3.2 The diffusion mechanism of solute atom

In the existing models, the solute diffusivity is an important parameter in the calculations. Volume and boundary diffusion were considered separately in different models. Lagneborg and Zajac [13] had compared the sheet spacing calculated from different diffusion mechanisms and suggested that boundary diffusion of vanadium

rather than the bulk one leads to reasonable predictions. The sheet spacing predicted by volume diffusion consideration, generally, would result in an extremely small value [13]. For IP, the carbides mainly precipitate on the α/γ interface, indicating the α/γ phase boundary basically acts as the preferred nucleation site for carbides. We therefore suggest using boundary diffusivity of solute in the present model. The boundary diffusivity of carbide-forming elements, such as Nb and V, are available in several studies, which could be used directly in the present model [11, 57]. For example, the boundary diffusivity of vanadium is given by [11]

$$D_V = 11646.6 \exp\left(-\frac{272400}{RT}\right) \tag{5-45}$$

5.3.3 The interface mobility, *M*

It has been well-recognized that interface mobility is a function of steel composition and transformation temperatures. In Fe-C binary system, the mobility of α/γ interface can be written as [95]

$$M = M_{\circ} \exp(-\frac{Q}{RT}) \tag{5-46}$$

where $M_{\circ}$ is the pre-exponential factor and Q is the activation energy. For multi-component alloyed steels, the interactions between different atom species must to be involved in defining *M*. For sake of simplicity, equation (5-46) is applied in the

following calculations.

Looking through the above rate equations, one can identify two parameters that must be considered as adjustable, $N_{\circ}^{p}$ and $N_{\circ}^{\alpha}$. All the remaining parameters in equations (5-37), (5-38), and (5-41) are either known for a given alloy composition and temperature or can be reasonably estimated from the literature. The required parameters for the calculations are listed in Table 5-3.

Table 5-3 The parameters used in the calculations

Symbols	Magnitudes	Descriptions	Units
M_o	58×10^{-3}	pre-exponential factor of mobility [95]	$mmol / Js$
Q_M	140	energy barrier for mobility [95]	kJ/mol
Q_B	140	energy barrier for ferrite nucleation [95]	kJ/mol
σ_o	0.5	ferrite/austenite interfacial energy [96]	J/m^2
a	0.286	lattice parameter of ferrite	nm
V_p	10.81	molar volume of VC	cm^3/mol
V_{Fe}	7.10	molar volume of ferrite	cm^3/mol
V	1.52	The ratio of V_{VC}/V_{α}	dimensionless
ω	0.01	geometric factor of ferrite nucleation [96]	dimensionless

5.4 Applications of the model and discussions

In this paper, we assume that $c_{crit} = c_p^{\circ}$. This assumption suppose that the carbon rejected from the α goes directly into precipitate. In other words, the solute enrichment in austenite is supposed to be weak and a steady-state transformation condition can be applied. In that specific case, interphase precipitates nucleate at a constant critical level. This assumption is particularly valid when the carbon and micro-alloyed concentrations are reasonable comparable. Then, it permits to have reasonably long transformation periods where a steady-state condition can be

approximately maintained.

5.4.1 Prediction of the sheet spacing

In the following sections, the main goal is to highlight the availabilities of the developed model for predicting the microstructural characteristic of IP.

The sheet spacing of IP is a representative microstructural characteristic and has been well-presented among literatures [52, 60, 74, 92]. The calculated sheet spacing is compared successfully with the measured ones in Figure 5-3. The latter are taken from published data in the literature (see references in the insert into Figure 5-3) and concerns with a large range of temperature (from 630°C to 720°C) and composition (from 0.05wt%C to 0.44wt%C).

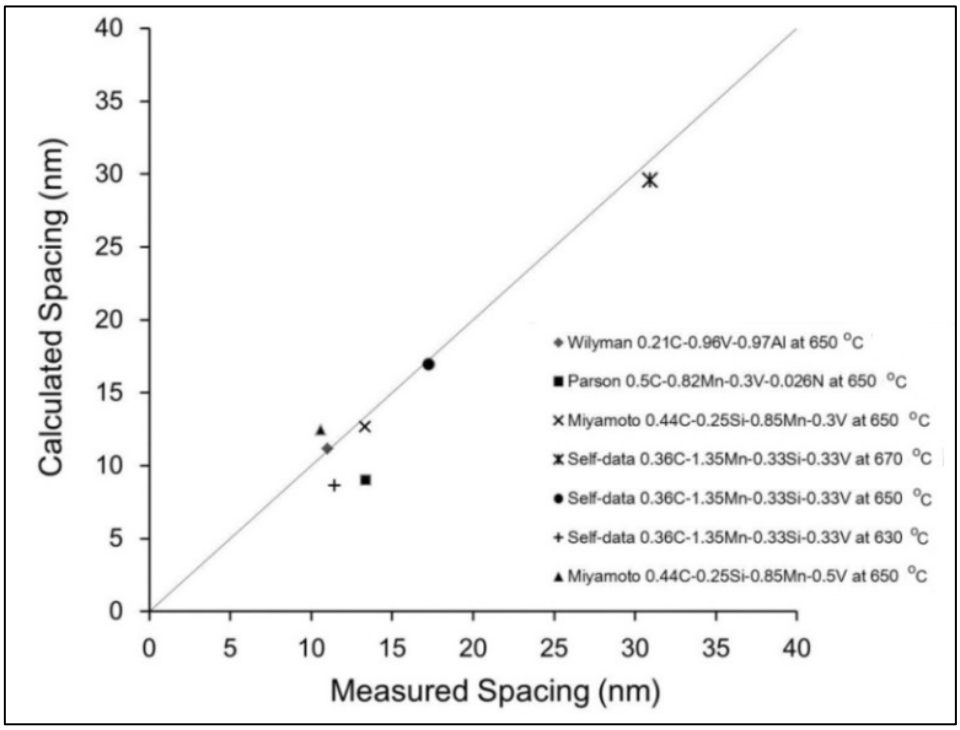

Figure 5-3 Coupling with experimental data to the calculated sheet spacing showing that good agreements with the sheet spacing measured at lower transformation temperatures (< 700 °C). The experimental data is cited from Wilyman [92], Parson [52], and Miyamoto [74]

For a given composition, the developed model predicts very well the evolution of the sheet spacing as a function of temperature. For example, the comparison with data from [52, 60, 74, 92] shows that the sheet spacing increases with temperature (see Figure 5-3). We learn from our model that it is mainly due to a decrease of both the ledge nucleation rate J_B and driving force ΔG for transformation with temperature and to a concomitant increase of solute diffusivity with temperature. Furthermore, results of calculations show clearly that temperature is one of the process parameters that influence strongly the evolution of sheet spacing. This shows clearly one of the interests of the developed approach.

5.4.2 Prediction of the particle spacing and the interface velocity

Compared to the sheet spacing, the particle spacing and the interface velocity are somehow difficult to be quantitatively measured or determined. Especially for particle spacing, it is not common for such a prediction in the existing models [9]. It is promising to note that as the transformation temperature and the composition of steel are given, the particle spacing and the interface velocity could be also calculated by equations (5-38) and (5-41), respectively. Here, the composition studied by Parsons and Edmonds [52] has been used (0.5wt%C, 0.82wt%Mn, 0.026wt%N, 0.3wt%V) for calculations. The results are given in Figure 5-4 and in Figure 5-5 and show that the particle spacing decreases with increasing the transformation temperature while the interface velocity shows an opposite tendency.

Equation (5-41) shows that the obtained particle spacing is related to J_B, J_p, M and ΔG, which all decreases with increasing the transformation temperature while the mobility M show an opposite tendency.

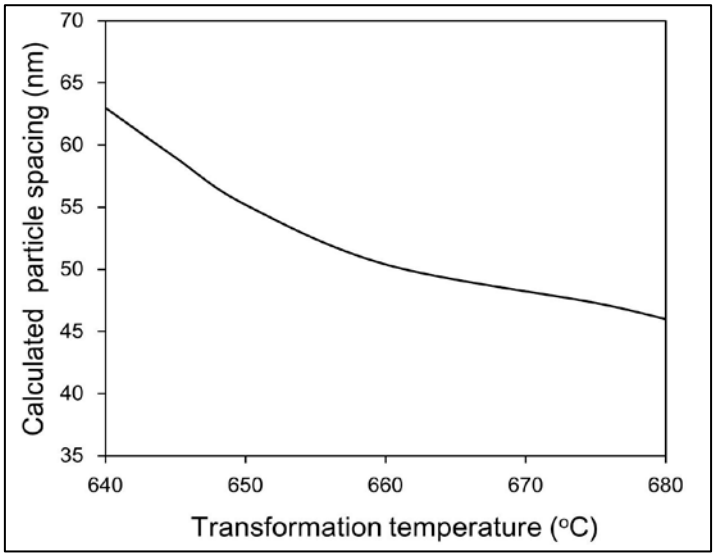

Figure 5-4 The calculated particle spacing. The composition studied by Parsons and Edmonds [52] has been used (0.5 wt%C, 0.82wt%Mn, 0.3wt%V, 0.026wt%) .

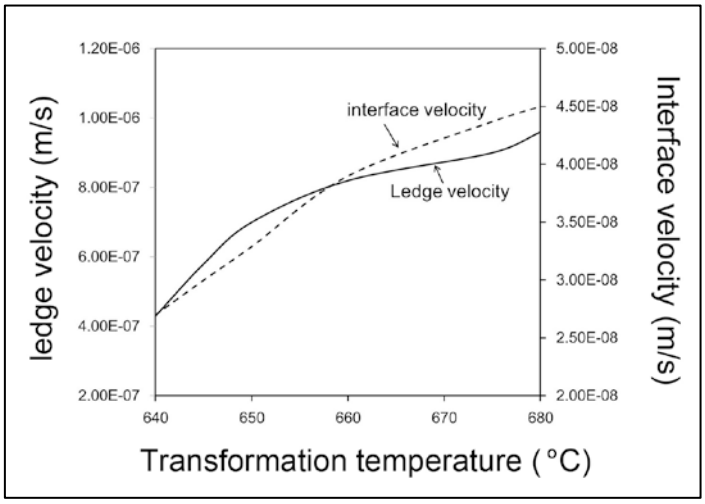

Figure 5-5 The calculated interface velocity from superledge model and ledge velocity; The composition studied by Parsons and Edmonds [52] has been used (0.5 wt%C, 0.82wt%Mn, 0.3wt%V, 0.026wt%).

The nucleation rate J_p being at the denominator (see equation (5-41)), the obtained evolution can be explained by the decrease of both ledge nucleation rate J_B and driving force for transformation ΔG with increasing temperature. As a consequence, such an evolution results from the coupling between ferrite formation and interphase precipitation and depends on both kinetics and thermodynamic effects.

On the contrary, the increasing velocity with transformation temperature is mainly resulted from the higher ferrite growth rate at the higher transformation temperature.

Both the interface velocity and ledge velocity are compared in Figure 5-5. It is worth noting that ledge velocity is one order of magnitude higher than the interface velocity. This show clearly how IP can interact with migrating interface and how it can slow down it.

Although the results shown in Figure 5-4 and Figure 5-5 are based on the theoretical calculations and need additional experimental data to be compared with, the present model has shown the capability to be a new approach to integrate all the features of interests on interphase precipitation such as the sheet spacing, the particle spacing and the interface velocity.

5.4.3 The effects of C and V contents on sheet spacing of IP

The composition dependence of the sheet spacing can be addressed as well by

the present model. Figure 5-6 shows the calculated dependence of sheet spacing on C and on V. It indicates that the sheet spacing increases with increasing either C or V content. Figure 5-6 is also used to compare the results of Lagneborg and Zajac [13]. The dependence of sheet spacing on C content calculated by the present model is consistent with that predicted by Lagneborg and Zajac (Figure 12 in ref. [13]). On the contrary, it is interesting to note that in the work of Lagneborg and Zajac the superledge height increases with V content, which is consistent with our calculation showing in Figure 5-6, but the consequence on the resulting sheet spacing reveals an opposite feature (Figure 13 in ref. [13]). This contradiction, however, is not well-addressed in their work. Further experimental work is in progress to investigate these points.

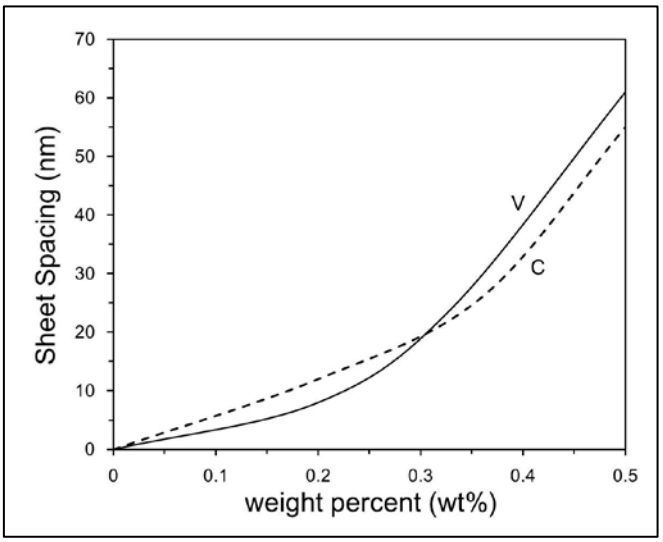

Figure 5-6 The calculated sheet spacing changing with C and V contents

5.5 Conclusion

A new model describing the carbides periodically precipitating on a migrating

α/γ interface has been proposed. The present model follows the main two features of interphase precipitation: (a) the interphase precipitation is accomplished by ledge mechanism of $\gamma \rightarrow \alpha$ transformation, and (b) the precipitation on interface is actually a multi-interaction of precipitation and transformation kinetics. The features of interests, the sheet spacing, the particle spacing, and the overall interface velocity, are now expressed in terms of α ledge and carbide nucleation rates and the driving force for $\gamma \rightarrow \alpha$ transformation. As the transformation temperature and the composition of steel are given, the characteristics of interphase precipitation could be predicted.

The calculated sheet spacing of IP is compared successfully with measured data from literature. The particle spacing and interface velocity are calculated as well. The proposed superledge model consequently could be used to predict the precipitation kinetic (the sheet spacing and the particle spacing) in combination with the transformation kinetic (the interface velocity). In addition, the dependence of sheet spacing on C and V contents is calculated and discussed with the results of Lagneborg and Zajac. The variation of sheet spacing with C calculated by superledge model is consistent with their work, but a contradiction is observed as the V content is changed. Future work is in progress to clarify this issue.

List of symbols

v	ferrite ledge velocity
v^*	ferrite ledge velocity at unpinning
$v^{\circ}_{\alpha\gamma}$	overall interface velocity without the presence of carbides on the interface
$v_{\alpha\gamma}$	overall interface velocity with carbide precipitation on the interface
M	ledge mobility of the unit ledge with a height of a
M_h	ledge mobility of the ledge with a height of h
$M_{\circ}$	pre-exponential factor of ledge mobility
Q	activation energy for interface advancement
Q^{α}	activation energy for ferrite ledge nucleation
Δg_p	driving force for carbide nucleation
ΔG	austenite-to-ferrite transformation driving force
ΔG^*_{α}	maximum of Gibbs energy associated with the formation of a ferrite nuclei
ΔG^*_p	maximum of Gibbs energy associated with the formation of a carbide nuclei
ΔG_{ZP}	carbide pinning force
ΔG°_{ZP}	carbide nominal pinning force
$\sigma_{\circ}$	ferrite/austenite interface energy
σ_p	ferrite/carbide interface energy
γ	interfacial energy associated carbide precipitating on ferrite/austenite interface
N°_{α}	number of ferrite nucleation site on the ferrite/austenite interface

N_p°	number of carbide nucleation site on the ferrite/austenite interface
ω	geometric factor for heterogeneous nucleation
c_c^γ	carbon concentration in austenite
c_c^α	equilibrium carbon concentration in ferrite
c_p	solute concentration of carbide
c_p°	nominal solute concentration
c_c°	nominal carbon concentration
D	boundary solute diffusion coefficient
f_α	volume fraction of ferrite
f_γ	volume fraction of austenite
f_p	volume fraction of carbide
V_p	molar volume of carbide
V_{Fe}	molar volume of ferrite
J_B	ferrite ledge nucleation rate
J_T	ledge nucleation rate on the top of base ledge
J_p	carbide nucleation rate
K_p	solubility product of carbide in austenite
R	carbide radius
R_{unpin}	carbide radius at superledge unpinning
a	unit ledge height (ferrite lattice parameter)
b	ledge spacing

b_p	inter-particle spacing in one sheet of interphase precipitation
d_γ	half of prior austenite grain size
l	superledge spacing
λ	sheet spacing of interphase precipitation
h	ledge height
h^*	the critical height of superledge for unpinning
t^*	time for ledge to reach its critical height for unpinning from carbides
τ	characteristic time for steady-state ledge-wise growth
τ_n	time for a unit ledge to nucleate on the top of the base ledge
$\tau_\circ$	time for created unit ledge to spread over a distance of b_p on the top of base ledge
τ_λ	characteristic time for overall interface to advance in a distance of λ
τ_w	waiting time to build a superledge to unpin from carbides
τ_f	time for unpinned superledge to merge neighboring superledges
τ_p	carbide incubation time

Chapter 6

The Feature evolutions of interphase precipitation with the progression of austenite-to-ferrite transformation

6.1 Introduction

The models reviewed and discussed previously have shown good agreements with experimental results and the temperature dependence of sheet spacing are correctly accounted for. It is worth noticing that the existing models did not consider the effect of carbon enrichment in austenite on the characteristics features of interphase precipitation. This is because the analyzed materials in the proposed models were low carbon and low alloyed steels, the carbon enrichment in austenite would not affect greatly kinetics of austenite-to-ferrite transformation. It is expected that this would affect both the kinetics of austenite-to-ferrite transformation and the precipitation state. Furthermore, the transition from interphase precipitation to carbide fiber would be affected. To our knowledge, the existing models do not consider these two points.

Because the increased demands for medium carbon steels for automobile components and steel bars for construction uses [1, 4, 47, 52, 97], it is worthy to understand the mechanisms of their microstructure formation. The superledge model described in Chapter 5 was modified, and the evolutions of the characteristic features of interphase precipitation are clearly revealed. In order to account for γ composition evolution, the results were discussed in terms of transformation driving force, ferrite and carbide nucleation rates. Finally, the conditions were established for the transition of interphase precipitation to carbide fibers.

6.2 Experiments

Heat treatments were carried on dilatometer in order to have relevant experimental data to be compared with the results of the model. Steel-C was machined into the dilatometer samples, which is a cylinder with 3 mm in diameter and 6 mm in length, respectively, prepared from the quarter diameter position beneath the surface of the steel bars. In order to reduce element segregation, the machined samples were sealed in quartz tubes filled under argon atmosphere, and then homogenized at 1200 ^{o}C for 3 days, after that, they were water quenched to the room temperature for dilatometer experiments. The homogenized samples were re-heated to 1200 ^{o}C for 3 min and subsequently cooled at a rate of 20 ^{o}C/s to 670 ^{o}C, 650 ^{o}C, and 630 ^{o}C for 1 h, respectively, and quenched to room temperature 100 ^{o}C/s. The transformed microstructure of each sample is presented in Figure 6-1.

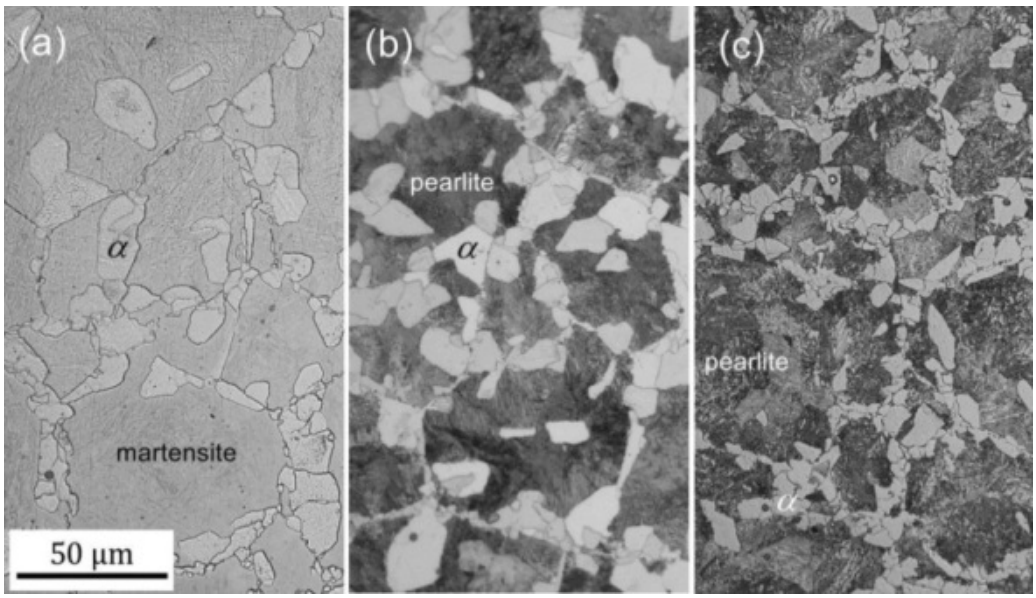

Figure 6-1 The optical micrographs taken from samples isothermally transformed at (a) 670 ^{o}C; (b) 650 ^{o}C, and (c) 630 ^{o}C for 1h.

Samples for transmission electron microscopy (TEM) were sliced from the transformed samples and then electro-chemical polished by using 5% perchloric acid.

They were then examined by using an FEI Tecnai G^2 20 TEM and an F30 field-emission-gun TEM equipped with an energy dispersive X-ray spectrometer (EDX) operating at accelerating voltages of 200 kV and 300 kV, respectively. The sheet spacing of the interphase-precipitated carbide is measured directly. The particle spacing in the sheet of carbide is, however, measured indirectly by estimating the thickness of the thin foils [98, 99].

6.3 Modeling

a. Summary of the superledge model for interphase precipitation

The physical procedure is that the α/γ interface moves by ledge nucleation and growth. Carbides precipitate at ledges and pin them until the ledge is high enough to overcome Zener pinning; the free interface then jumps from the pinning precipitates up to the positions where re-nucleation of carbide can occur. Compared to other studies [100], the carbide is proposed to have great effects on pinning the interface and superledge development. The detailed descriptions of superledge model have been presented elsewhere (see Chapter 5). The original expressions of the particle spacing in one sheet, b_p, overall interface velocity $v_{\alpha\gamma}$, sheet spacing λ, are summarized as follows.

$$b_p^2 = \frac{J_B^{1/3}\left(M\Delta G\right)^{2/3}}{J_p} \tag{6-1}$$

$$\lambda = \frac{\pi^{1/4} c_{crit}^{3/2}}{c_p^{\circ} b_p^2} \left(\frac{D\sigma_o}{aJ_B \Delta G} \right)^{3/4} \left(\frac{3V}{4} \right)^{1/2} \tag{6-2}$$

$$v_{\alpha\gamma} = \frac{c_{crit}^{1/2} b_p^2}{c_p^{\circ}} \left(\frac{D}{\pi} \right)^{1/4} \left(\frac{aJ_B \Delta G}{\sigma_{\circ}} \right)^{3/4} \left(\frac{4}{3V} \right)^{1/2} \tag{6-3}$$

where J_B and J_p are the α and carbide nucleation rates, respectively, M is the interface mobility, ΔG is the transformation driving force, D is the solute boundary diffusivity, $\sigma_{\circ}$ is the α/γ interface energy, c_p° is the nominal solute concentration, c_{crit} is the solute content in γ when the superledge unpins from carbides, and V is the ratio of carbide molar volume to that for α.

In order to calculate the evolution of features of IP, the carbon and solute contents in γ have to be considered in detail. In the case of IP, carbon and solute are consumed by the formations of α and carbide. The carbon and solute concentrations at the interface directly influence the driving forces of α and carbide nucleation at a given transformation temperature. An approximation of $c_{crit} = c_p^{\circ}$ can be given in the case that the carbon enrichment is neglected, and the equations can be simplified. In medium-carbon or high-carbon alloyed steels, the magnitude of c_{crit} is expected to decrease because of carbides precipitation. The difference between c_{crit} and c_p° would become larger and finally deviate greatly from the approximation. Accordingly, equations (6-2) and (6-3) without the approximation are more suitable to calculate the

evolutions of features of IP for concentrated alloys, and to account more accurately for the evolution of γ composition.

b. The mass balance of carbon and solute

In order to include the evolution of carbon and solute in γ in the calculations, the mass balance of carbon and solute are individually calculated because they directly affect the ferrite nucleation energy and the driving force for transformation, as shown in Figure 6-2. At each iteration, the mass balance is used to evaluate the carbon and solute concentrations in γ after each row of carbide is formed [94].

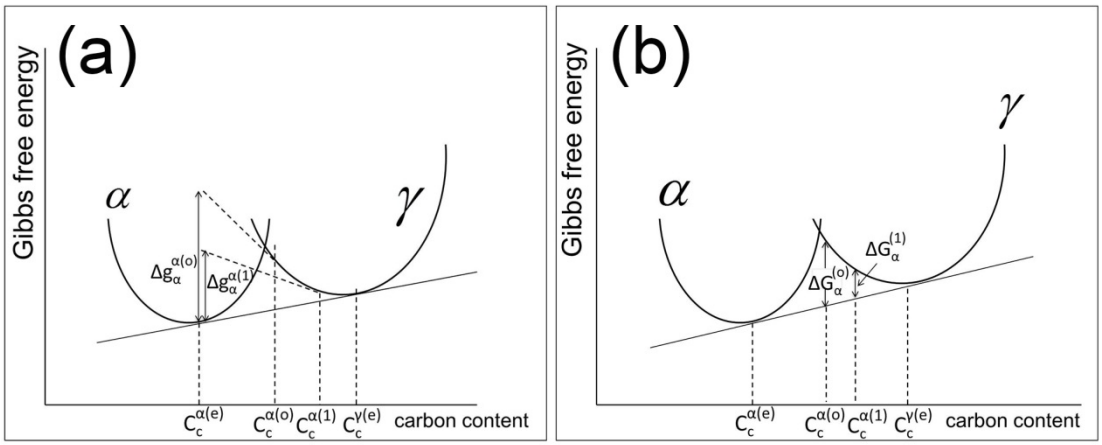

Figure 6-2 Schematically illustrations showing the decreasing in (a) α nucleation energy, and (b) transformation driving force for transformation with the progressive of γ→α transformation

At each time-step, *t*, the following mass balance equation is used to evaluate the carbon and solute concentrations in γ after each row of carbide is formed:

$$c_{\gamma}^{t+dt} = \frac{c_c^{\circ} - c_c^{\alpha} f_{\alpha}^{t} - c_c^{p} f_p^{t}}{(1 - f_{\alpha}^{t} - f_p^{t})} \tag{6-4}$$

where c_c° is the nominal carbon content, c_c^{p} is the carbon content in precipitate, and c_c^{α} is the carbon content in α. For sake of simplicity, a pseudo-binary assumption is supposed for c_c^{α}. Then, the latter is constant at a given temperature and is equal to the equilibrium concentration given the tie-line passing through the nominal composition.

At the initial stage, γ transforms to α from prior γ grain boundary and grows into γ without any precipitation reaction, as shown in Figure 2(b). It is reasonable to assume such a condition for IP to start with. Lagneborg and Zajac [14] have shown that IP could not be directly developed at the initial stage of $\gamma \rightarrow \alpha$ transformation because the driving force is relatively large, leaving a precipitation free zone between the first row of carbide and prior γ grain boundary.

The evolution of both α and precipitate fractions are the unknowns in equation (7). The increase of α volume fraction, df_{α}^{t}, is calculated from the overall interface velocity (equation (3)) by considering that:

$$df_{\alpha}^{t} = \frac{v_{\alpha\gamma}}{d_{\gamma}} dt \qquad (6\text{-}5)$$

where d_{γ} is half of prior γ grain size.

Classically, the time evolution of mean radius shows a plateau corresponding to a stasis period during which the size histogram evolves at a constant mean radius [38]. Indeed, during this long period of time, the increase of mean radius due to growth is compensated by the nucleation of new ones with smaller radius. For the sake of simplicity, we will position into this context and the mean radius will be considered as a constant and equal to the measured one during the nucleation-growth step. Therefore, the increase of volume fraction of precipitates can be simplified and the following relation is obtained in the case of spherical particles:

$$df_p^t = \frac{4}{3}\pi R^3 \left(\frac{dN}{dt}\right) dt = \frac{4}{3}\pi R^3 J_p dt \tag{6-6}$$

where N is the number of carbides per unit volume which is associated with carbide nucleation rate, J_p, and R is the mean radius.

By integrating equations (6-5) and (6-6), the mass balance equation can be solved at each time-step. Figure 6-3 illustrates the mass balance calculations and Figure 6-4 shows the iteration procedures in calculations.

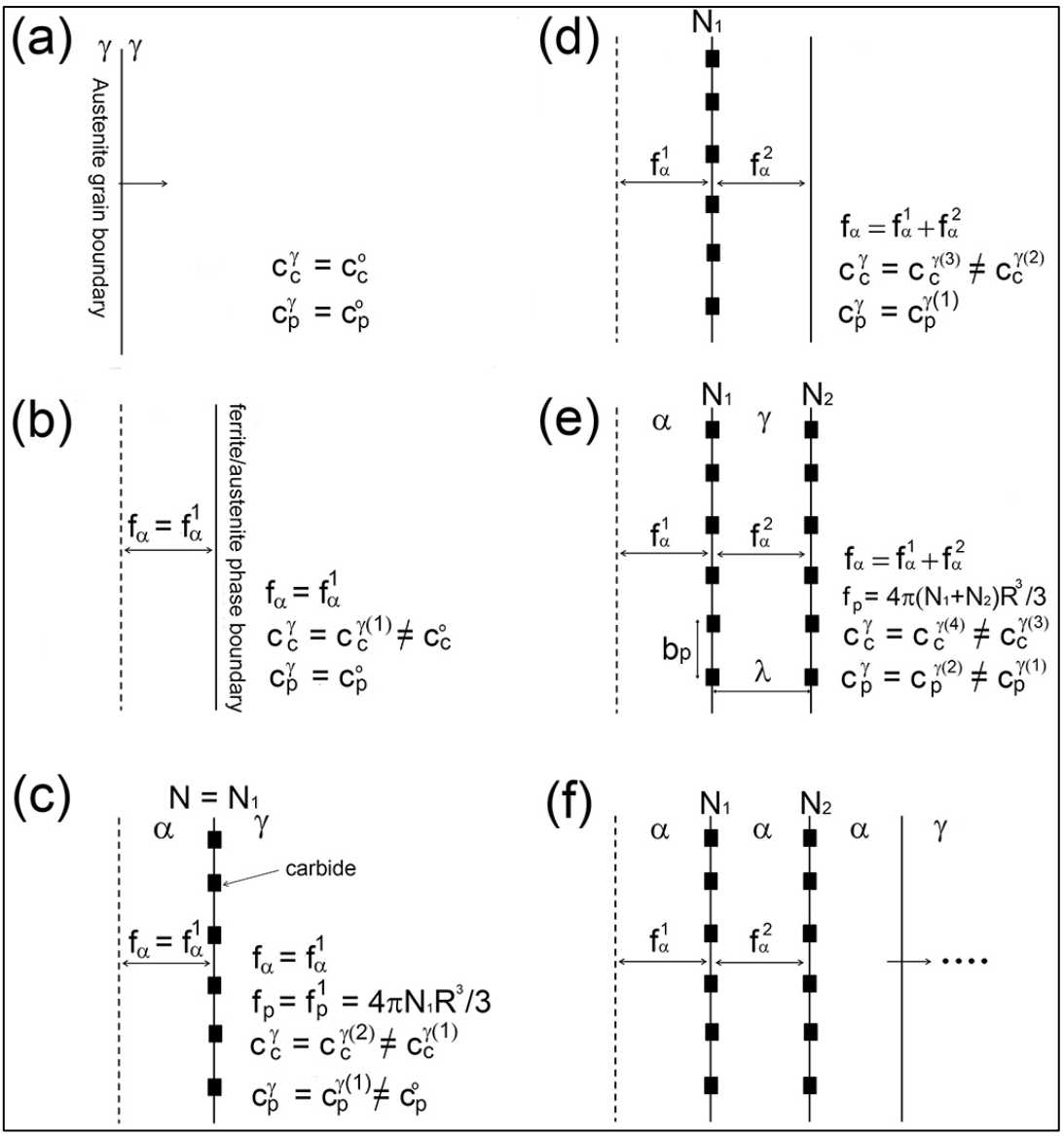

Figure 6-3 Schematic illustrations showing the proposed sequence of interphase precipitation accompanied with composition changes. (a) initial structure consisted of austenite only; (b) ferrite grows into austenite without carbide precipitation; (c) the first row of carbides forms on the ferrite/austenite interface; (d) ferrite advances again in a distance of sheet spacing of interphase precipitation; (e) The second row of carbides forms, and (f) continuously ferrite and carbide alternatively grows and precipitates, respectively.

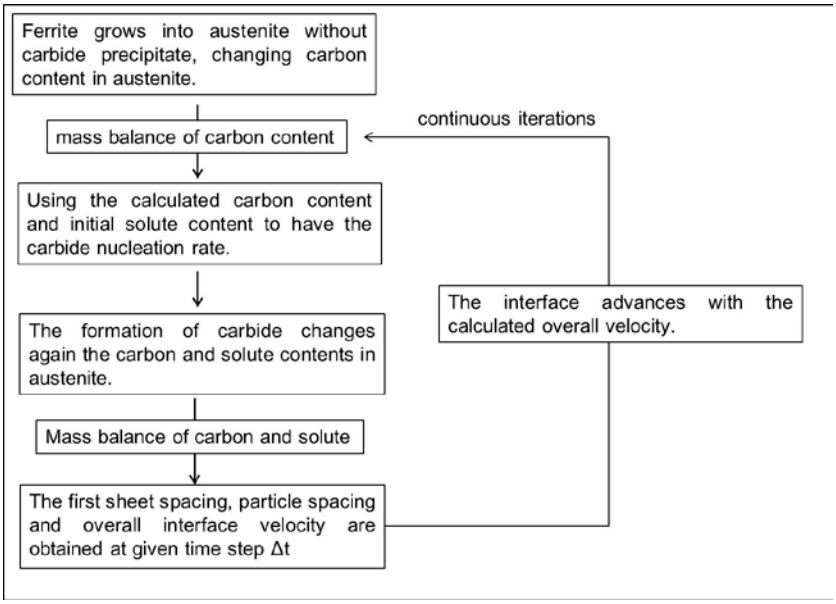

Figure 6-4 The flow chart of iteration procedures

6.4 Results

a. Microstructures of the interphase-precipitated carbide and the fibrous carbide

The microstructural features of IP are revealed by TEM. The quantitative measurements of microstructure are summarized in Table 6-1, showing that the sheet spacing and carbide size decrease with decreasing the transformation temperature but the particle spacing at every transformation temperature is approximately the same.

Table 6-1 The features of interphase precipitation measured by TEM

		Transformation Temperature		
Features	unit	670 ^{o}C	650 ^{o}C	630 ^{o}C
sheet spacing	nm	34.1 ± 4.7	19.3 ± 2.1	12.3 ± 1.1
particle spacing	nm	42.6 ± 3.8	41.4 ± 1.0	40.2 ± 5.6
particle size	nm	6.8 ± 0.2	4.2 ± 0.1	3.2 ± 0.1

Figure 6-5 gives representative structure of IP at different transformation temperatures and representative corresponding high-resolution TEM images for carbide size determinations.

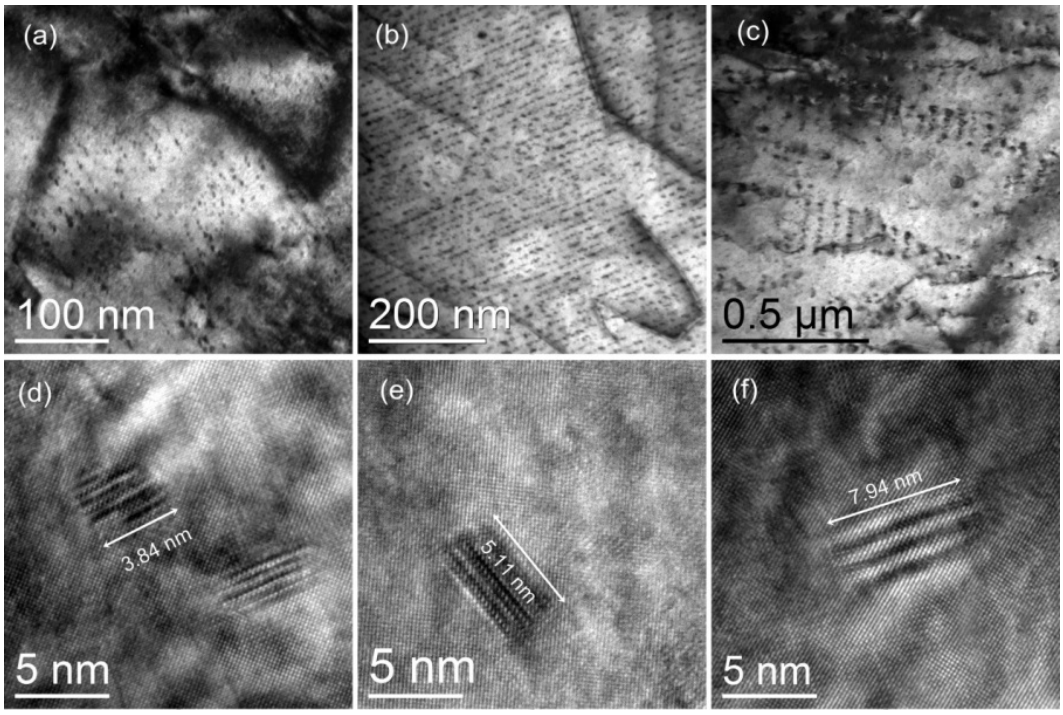

Figure 6-5 TEM micrographs of interphase precipitation and corresponding HRTEM lattice images taken on the samples transformed isothermally at: (a, d) 630 ^{o}C, (b, e) 650 ^{o}C, and (c, f) 670 ^{o}C.

The fibrous precipitates are also observed in some ferrite grains of the steel studied, as shown in Figure 6-6. Direct TEM evidences have indicated that the nucleation sites for fibrous carbides and for interphase-precipitated carbides are different [101], and the former precipitate mode is favored by both a slowing down of the ferrite/austenite interface [5] and an incoherent interface [2]

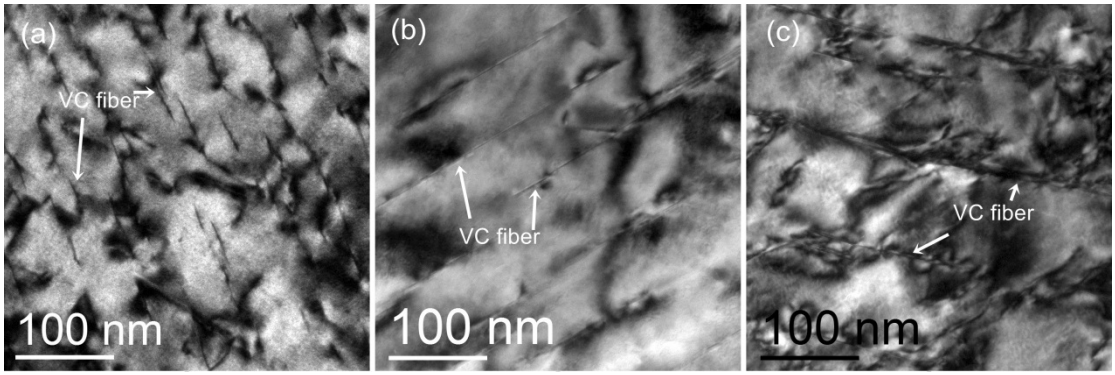

Figure 6-6 The TEM micrographs of typical carbide fiber microstructure isothermally transformed at (a) 630 ^{o}C, (b) 650 ^{o}C, and (c) 670 ^{o}C

As far as the crystallographic aspect is concerned, a semi-coherent α/γ interface following Kurdjurmov-Sachs orientation relationships was accounted to be the interface for ledge mechanism operation of IP. However, Yen [8] and Okamoto [13] and Miyamoto [27] have shown that the ledged interface of IP does not have to $\{1\ \ 1\ \ 0\}_\alpha$ but actually be close to be $\{2\ \ 1\ \ 1\}_\alpha$, $\{1\ \ 1\ \ 1\}_\alpha$, and $\{2\ \ 1\ \ 0\}_\alpha$. Their powerful TEM and EBSD evidences indicate that the operation of ledge mechanism of $\gamma \rightarrow \alpha$ transformation do not have to be associated with a semi-coherent interface. Therefore, according to the present study, it would be suggested that the kinetics of ferrite/austenite interface is the key factor to determine the development of fibrous carbide.

b. Modeling results

Figure 6-7 shows the calculated evolutions of particle spacing and sheet spacing with time, i.e. with progressing of $\gamma \rightarrow \alpha$ transformation. The sheet spacing decreases as transformation proceeds; however, the particle spacing demonstrates an opposite trend. These features are easy to be interpreted by normal metallurgical recognitions. By the use of mass balance consideration, the available solute content (vanadium) for further precipitation becomes less after the formation of each row of carbide, leading to a wider particle spacing. On the other hand, the sheet spacing is related to the interface velocity. During the transformation, the interface velocity decreases with because of the lowering driving force for transformation (see Figure 6-2(b)), the sheet spacing becomes finer at the later stage of transformation.

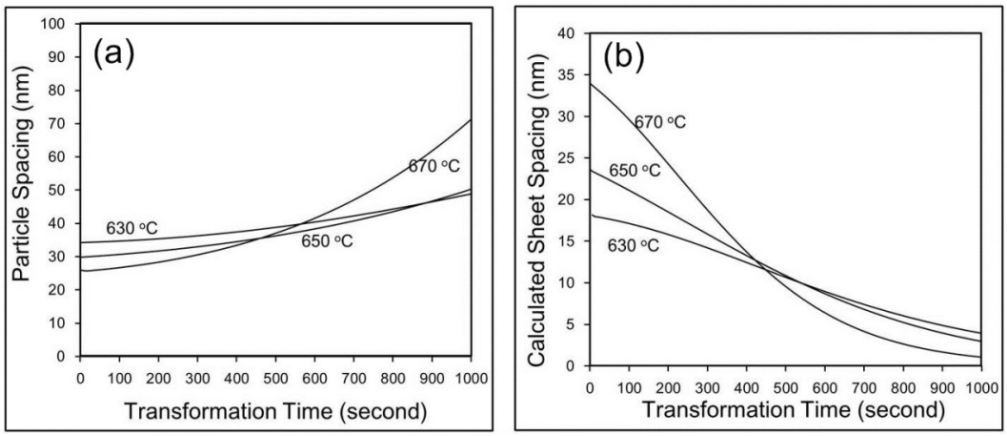

Figure 6-7 The calculated evolutions of (a) particle spacing and (b) sheet spacing with time at different transformation temperatures, showing that the sheet spacing becomes finer but particle spacing exhibit an opposite tendency as transformation proceeds.

6.6 Discussions

a. The effect of carbide precipitation on the overall interface velocity

The overall interface velocity is also calculated and additional samples were isothermally transformed at 650 ^{o}C for 30s, 90s, 180s, and 600s respectively to show the availability of the calculated results, as shown in Figure 6-8. The α thickness transformed at different time step was measured from individual micrograph, which is presented in Figure 6-8(b). Each data point was measured at least 10 ferrite grains. It shows that the α thickness calculated by our approach is consistent with that measured from optical micrographs.

The interface velocity of the case of interface precipitation is a function of α nucleation rate, transformation driving force, and particle spacing (see equation (6-3)). The latter increases with time (See Figure 6-7(a)) whereas the former two ones are known to decrease with time during ferrite transformation. However, we have to keep in mind that all these parameters are tightly related (equations (6-1) to (6-3)). The overall interface velocity thus results from the combination of these various aspects. That is why, we have decided to plot the evolution of $\upsilon_{\alpha\gamma}/\upsilon_{\circ}$, where $\upsilon_{\circ}$ is the

velocity for the ferrite/austenite interface migrating without the carbides on the interface in order to show the contribution of interphase precipitation on interface velocity. As shown in Figure 6-9, the ratio of $\upsilon_{\alpha\gamma} / \upsilon_{\circ}$ is found to decrease with the progressive of transformation and smaller than one and in the order of 10^{-2}, indicating that IP has a strong slowing impact on interface velocity. It is not surprising because carbides precipitated can have a non-negligible effect on pinning the ferrite/austenite interface.

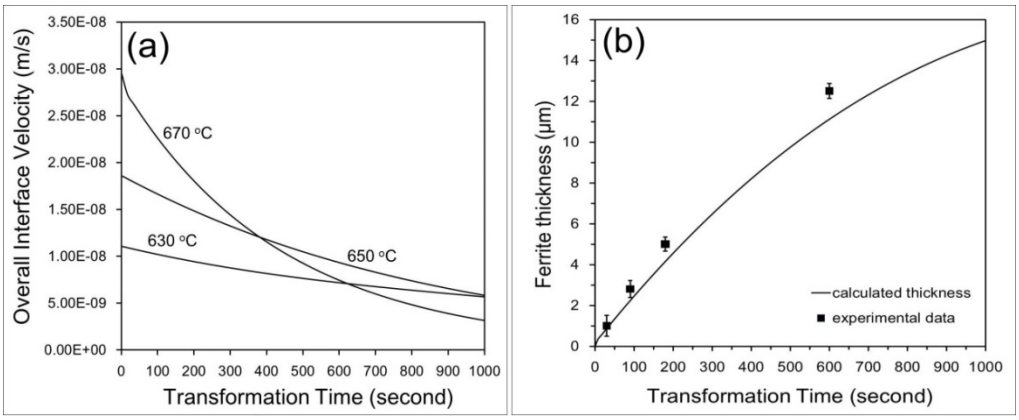

Figure 6-8 (a) the calculated evolutions of overall interface velocity with time, and (b) the calculated evolution of ferrite thickening isothermally at 650 °C showing a good agreement with experimental data.

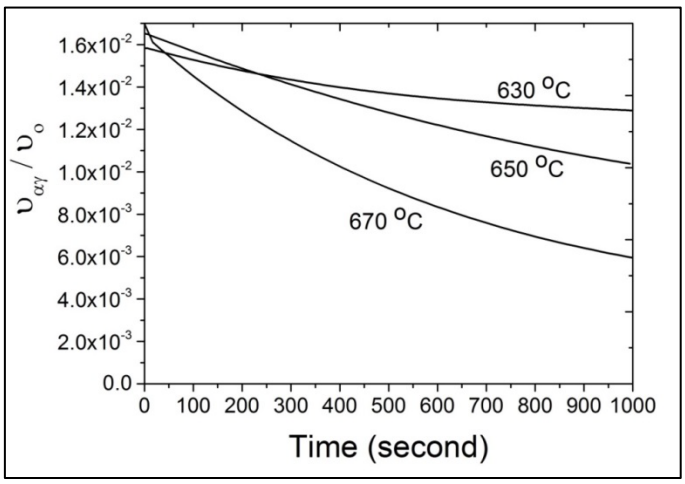

Figure 6-9 The ratio of $\upsilon_{\alpha\gamma} / \upsilon_{\circ}$ at different transformation temperatures with the progressive of austenite-to-ferrite transformation of the steel studied

It is interesting to see that the present results show the sheet spacing becomes finer as the transformation proceeds. This feature is consistent with the observation of Murakami [16] but contradicted with the results of Lagneborg and Zajac [11]. It can be shown that the interface velocity and sheet spacing can be simply related to the diffusion coefficient by combining equation (6-2) and (6-3):

$$v_{\alpha\gamma} = \left(\frac{c_{crit}}{c_p^{\circ}} \right)^2 \frac{D}{\lambda} \tag{6-12}$$

This relation clearly shows that for a given temperature, a slower interface velocity is associated with a wider sheet spacing when the approximation $c_{crit} = c_p^{\circ}$ is fulfilled. In that specific case, we have:

$$v_{\alpha\gamma} = \frac{D}{\lambda} \tag{6-13}$$

The results of Lagneborg and Zajac [11] reveal a similar tendency where the sheet spacing increases during the thickening of ferrite growth. However, as the carbon content increases, the effect of carbon enrichment in γ on the interface velocity is no longer neglected. The c_{crit} would be reduced with increasing $\gamma \rightarrow \alpha$ transformation because of carbide periodically precipitated on the interface. Finally c_{crit} deviates from $c_{\circ}$ in great extents at the later stage of transformation. Therefore, it is more reasonable to use equation (6-12) instead of equation (6-13). The magnitude of $\left(c_{crit} / c_p^{\circ} \right)^2$ then becomes smaller while decreasing c_{crit} during the progressive of

$\gamma \rightarrow \alpha$ transformation. In that case, the interface velocity decreases with time and the calculated evolution of α thickness is in very good agreement with that one measured (see Figure 6-8) and consistent with the TEM observations of Murakami [16].

As far as the role of interface velocity is concerned, a simple intuitive interface explanation for the formation of fibrous carbide can be proposed, as shown in Figure 6-10. The carbide nucleated at the ledge can grow along the side of ledge by a fast diffusion path. If the carbide growth exceeds the ledge growth, the unpinning even will never occur and fibrous carbide would be produced. This will of course be promoted by lower driving force for $\gamma \rightarrow \alpha$ transformation. A rational consequence is that the fibrous carbide will appear preferably in the later stage of the transformation [48]. According to Figure 6-10, the development of carbide fiber occurs when the pinning carbide grows along the pinned superledge. The particle spacing of interphase-precipitated carbides and the distance between carbide fibers are measured by TEM and shown in Figure 6-11. Compared to the particle spacing of IP, the carbide distance of carbide fiber is generally larger than that of interphase-precipitated carbides, implying that the fibrous carbide occurs at the later stage of austenite-to-ferrite transformation. A region showing the transition is given in Figure 6-12.

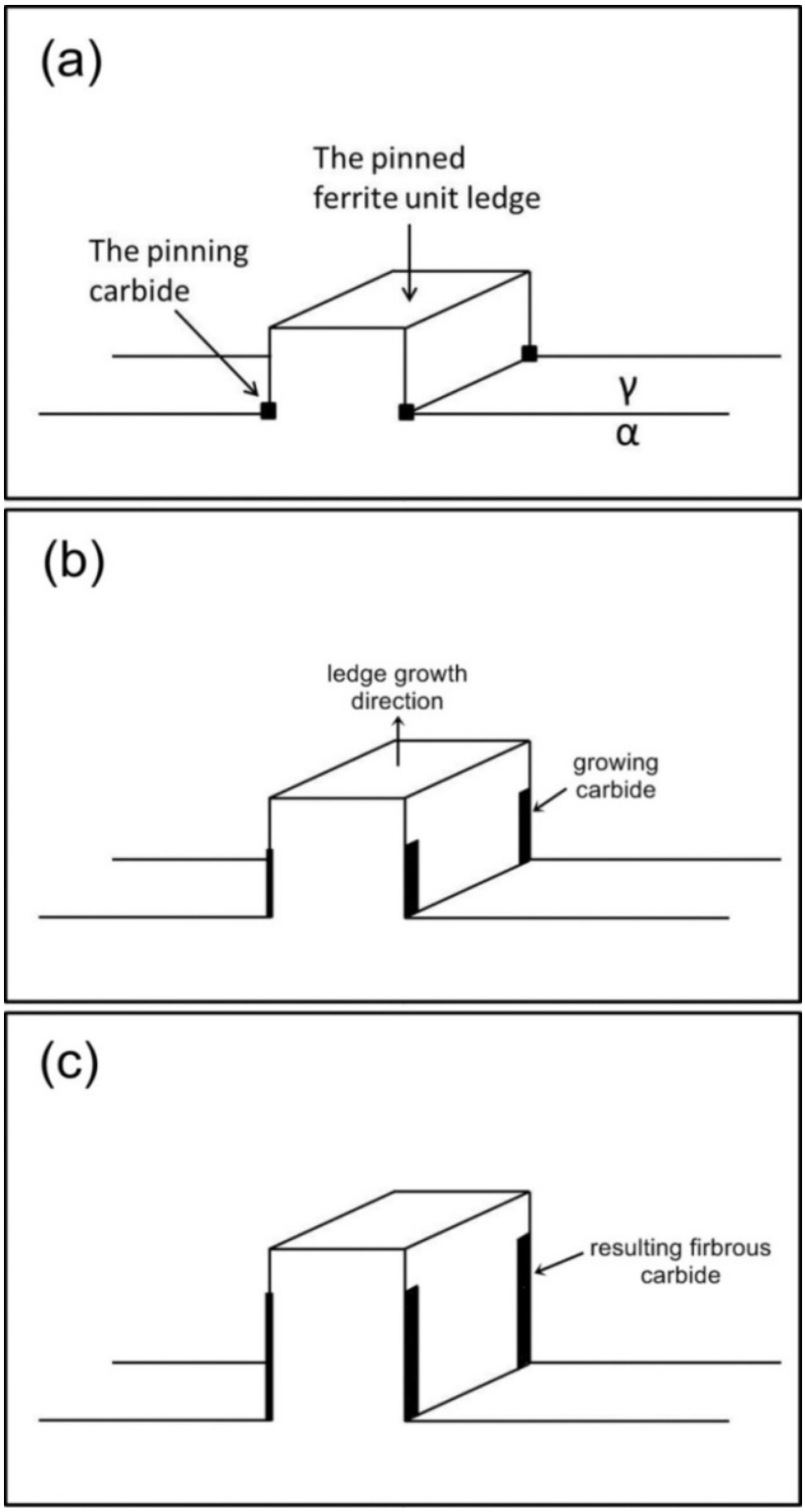

Figure 6-10 The proposed model for the formation of carbide fiber. (a) a unit ledge is pinned by carbides; (b) the growth of carbide exceeds that of ferrite, growing along the side of ledge, and (c) the ledge never unpins from pinning carbides, resulting in carbide fibers.

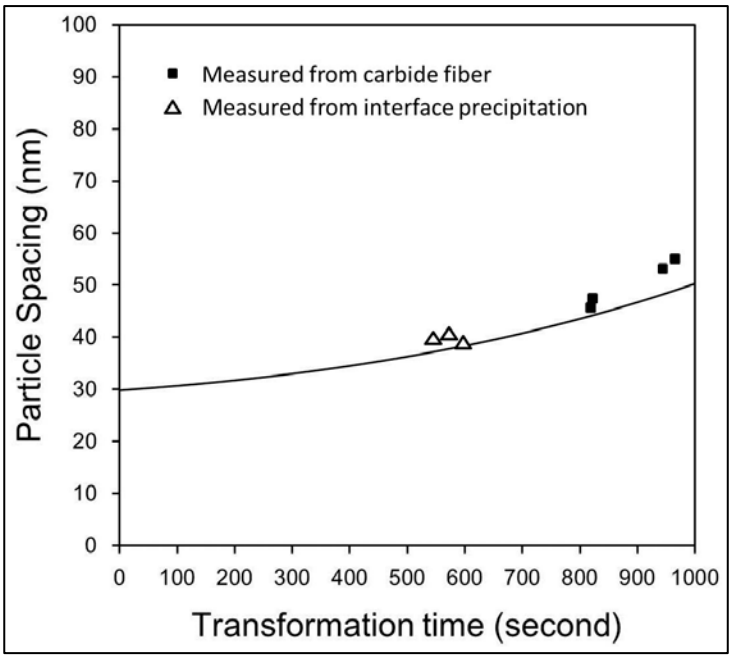

Figure 6-11 A comparison of measured particle spacing of different carbide aggregates measured at the samples isothermally transformed at 650 ^{o}C for 1h. The particle spacing of interphase precipitation and carbide fiber show distinctive two groups, indicating that the carbide fiber develops at the later stage of austenite-to-ferrite transformation.

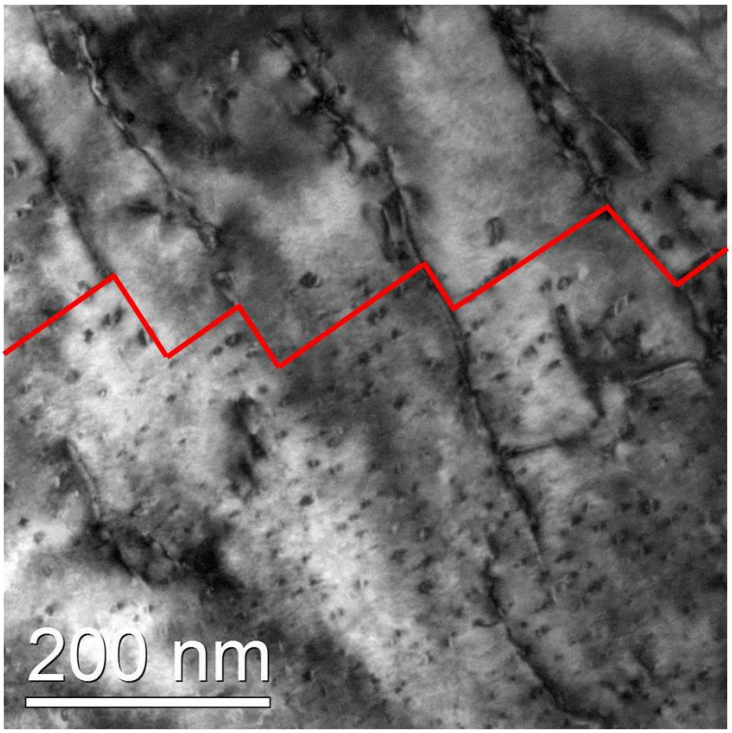

Figure 6-12 TEM micrograph showing the transition of interphase precipitation to fibrous carbide; the previous ledged interface can be well-illustrated.

b. The minimum sheet spacing of interphase precipitation at a given transformation temperature

For the austenite-to-ferrite transformation accomplished by ledge mechanism, Bhadeshia [51] proposed that there is a minimum ledge height for ledge mechanism of $\gamma \rightarrow \alpha$ transformation, $h_{\min}$, which is determined by α/γ interfacial energy, $\sigma_{\circ}$, and the free-energy change of formation α nucleus unit volume, ΔG_{α}^{m}

$$h_{\min} = \frac{\sigma_{\circ}}{\Delta G_{\alpha}^{m}} \tag{6-14}$$

In his work, the sheet spacing of interphase precipitation was used to support this proposition because ledge mechanism has been well-recognized for IP and the results show that the measured sheet spacing of IP was found to be greater than $h_{\min}$ in most cases. In superledge model, the sheet spacing is proposed to result from the combined interaction between α and carbide nucleation rates, transformation driving force, and particle spacing. It has been shown in Figure 6-7(b) that the sheet spacing becomes finer with time. However, the carbon enrichment in γ normally makes the α nucleation more difficult, which means the ΔG_{α}^{m} decreases with time (see Figure 6-2(a)). It is suggested to use equation (6-14) to define the minimum sheet spacing of interphase precipitation that can be observed as the transformation temperature is given.

The predicted sheet spacing by either equations (6-2) and (6-14) are shown in Figure 6-13. The experimental data are found to be within the range of feature predicted by superledge model, exhibiting good agreements with calculated results. The results presented above are very promising because it accounts for the evolution of features of IP with time.

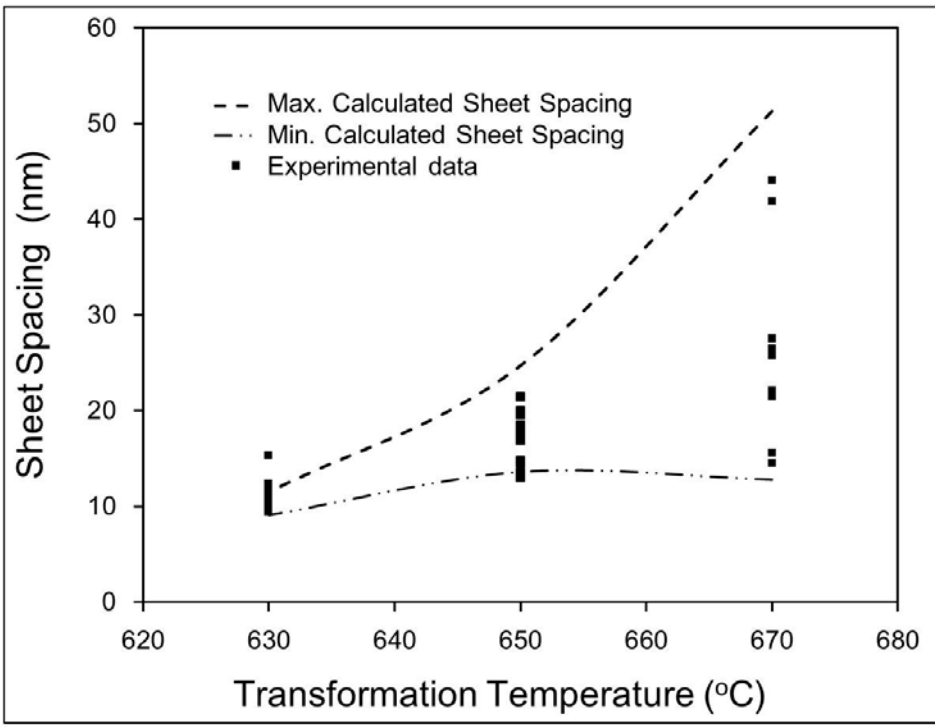

Figure 6-13 The boundary of the predicted sheet spacing coupled with experimental data (the solid points) measured at different transformation temperatures

6.7 Conclusions

The evolution of features of IP with progressive $\gamma \rightarrow \alpha$ transformation has been analyzed using a superledge model coupled with a mass balance approach to γ composition evolution. The work of Murakami is incorporated and discussed with the

present model. The main perspectives are highlighted as follows:

- The characteristic features of IP, the sheet spacing and particle spacing, evaluated by this approach are given by a range, instead of a discrete value and the experimental data exhibits good agreements with the calculated results. It is suggested that the variation in the characteristic feature of interphase precipitation becomes significant as the carbon and solute contents increase.
- The present superledge model enables us to predict the kinetics of austenite-to-ferrite transformation. The calculated overall interface velocity decreases as the transformation temperature is lowered, which is consistent with the metallurgical understandings. The thickening of ferrite from the present calculations is in agreement with the results obtained from dilatometer measurements.
- The present model takes the carbide pinning into consideration. It is noticed that the magnitude of interface velocity is considerably reduced because of carbide precipitating on the interface.
- The conditions for the development of carbide fiber are reviewed and clarified by the calculated results. It is suggested that a wider particle spacing combined with carbide growth along the superledge would favor the formation of fibrous carbide.

Chapter 7

The effect of the interphase-precipitated carbide on the strengthening contribution to ferrite

7.1 Introduction and context of the study

The control of microstructure in physical metallurgy is very important because it directly affects the mechanical properties. In order to characterize the mechanical properties, tensile test has been commonly used because it provides an efficient way to access to macroscopic quantities needed by engineer, such as the yield strength, tensile strength, Young's modulus…etc., of material. The elasto-plastic behavior of material can be also obtained by reading the generated stress-strain curve after each test. However, because the specimen of tensile test is usually in a millimeter scale , the generated stress-strain curve is actually a combination of all the strengthening contributions, for example, grain boundary strengthening, precipitation hardening, solid solution strengthening, and the effect of the second allotropic phase…etc. As a consequence, it is difficult to separate each strengthening contribution specifically by this approach. In order to study mechanical properties at a local level in direct relation with the intragranular microstructure, which in the dimensions of micro-meter and nano-meter, contact mechanics techniques, and more specifically nanoindentation have been proposed in this study.

The technique of contact mechanics has been widely used to estimate the strength of material [102-104]. Compared to the tensile tests, it gives an efficient way to reveal some of the mechanical properties of material by testing the specimen in a

smaller scale. The results depend on the type of indenter used during the indentation process. Vickers [105], Spherical, Conical, and Berkovich are commonly used in contact mechanics. One procedure to estimate the strength of material is to simply measure the diagonal length on the specimen after indentation, which is generally used in Vickers hardness tests [106]. This procedure inevitably leads to errors as the size of sample decreases. For the small-scaled indentation, nanoindentation has been developed to solve this problem.

The method of nanoindentation to determine mechanical properties of material had been discussed elsewhere [107-109] and been introduced by Oliver and Pharr since 1992 [110]. The principal goal of nanoindentation test is to extract elastic modulus and hardness of the specimen from experimental depth-penetrating curve. During the test, the indenter moves down to the surface of the material and the force and the depth of penetration beneath the specimen surface are recorded and presented. The main outputs of the depth-penetrating curve are:

a. The maximum load, $P_{\max}$

b. The maximum penetration depth, $h_{\max}$

c. The Stiffness, S

d. The residual penetration depth as the indenter is removed, h_r

Figure 7-1 illustrated these four quantities in a typical depth-penetrating curve. The output depends on the type of indenter, the yield stress, the strain hardening properties, and the elastic modulus of the materials. The depth of penetration together with the known geometry of the indenter provides an indirect measure of the area of contact at

full load, from which the hardness can be estimated by the mean contact force dividing by the projected contact area.

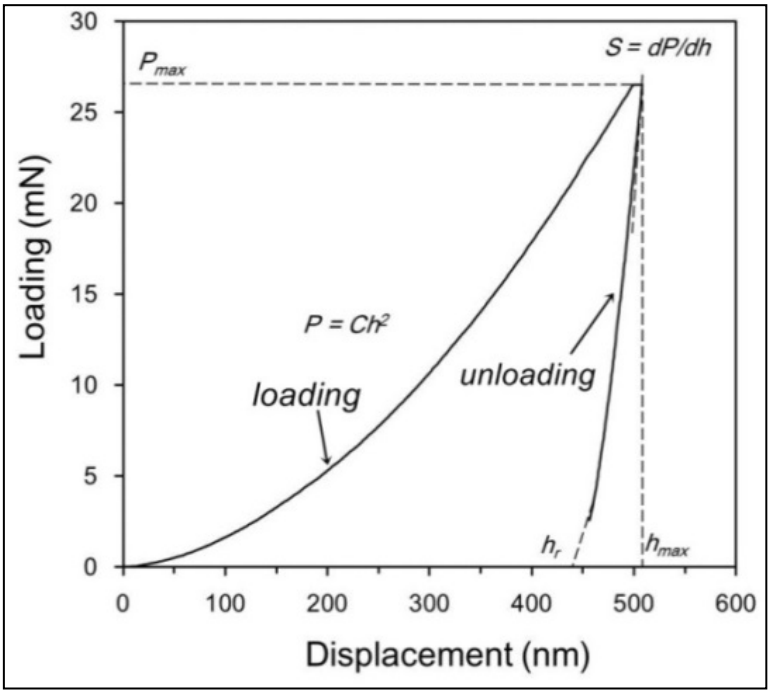

Figure 7-1 A schematically illustration showing the main quantities presented in the depth-penetrating curve

The elastic moduli of materials are determined from the slope of the unloading curve, which is formally called the indentation modulus of the specimen. The results also further provide information on the elastic modulus, on the hardness, on the strain hardening. Recent works have shown that some information can be obtained concerning cracking, plasticity induced phase transformation, and energy absorption [111-113]. All the above information requires a specific analysis of the depth indentation versus applied force curve.

Since the depth measured during the indentation includes both plastic and elastic displacement, the elastic contribution must be subtracted from the data to obtain

hardness. It is worth highlighting that when load is removed from the indenter, the material attempts to regain its original shape, but plastic deformation in the specimen after indentation results in a permanent deformation. These descriptions are presented in Figure 7-2. An analysis of the initial portion of this elastic unloading response gives an estimate of the elastic modulus. The portion of elastic and plastic deformation consequently determines the shape of depth-penetrating curve after each indentation. For a purely elastic case, the unloading curve is identical to the loading curve. For a plastically deformable material, the unloading curve will be a straight line and the initial slope gives access to the elastic indentation modulus.

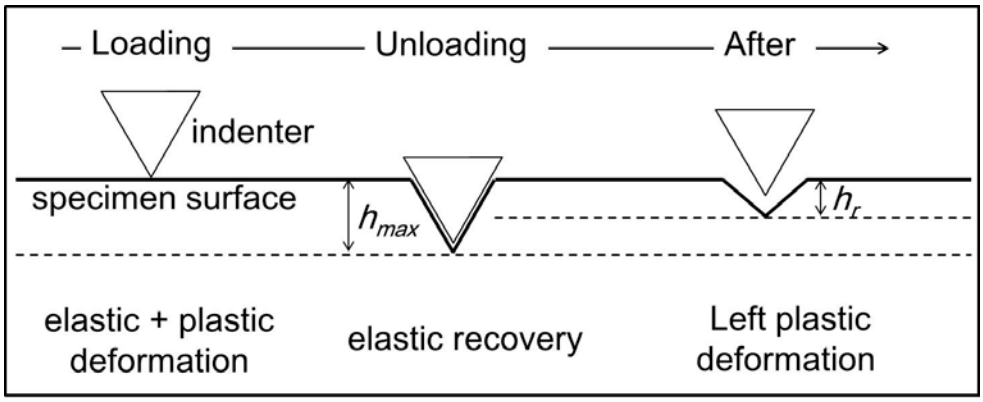

Figure 7-2 The ideal condition of the deformation and recovery of specimen during the indentation test.

The instrumented nanoindentation can provide more detailed and rich information regarding the mechanical behavior compared to the conventional Vickers hardness. As the indentations made by a nanoindentation instrument are very small, the price to pay to use this technique is that specimens must have a smoothly polished surface [102], around 1 μm roughness. .

Dao *et al.* [108] have presented a series of dimensionless functions to process the raw data from nanoindentation in order to obtain the Young's modules, *E*, the

representative stress, σ_r (which is related to the yield strength in a non-trivial manner) representative strain (known as to relate to the type of indenter), ε_r, and strain hardening exponent, *n*. The relations between this "apparent quantities, and the standardised tensile test results, depend of the indenter geometry. Bucaille *et al.* [104] then proposed another approach to improve the precision in the analysis of strain hardening by using two different indenters. In the present work, we have decided to use Bucaille's approach rather than Dao's one because it has been shown elsewhere that the former approach is capable of providing more reasonable predictions [104].

7.2 The conversion of the depth-penetrating curve into mechanical properties

7.2.1 Bucaille's approach

For metallic materials, Dao *et al.* had proposed several dimensionless equations to process the raw data of nanoindentation. These equations provide an efficient way to obtain Young's modulus, strain hardening exponent, yield strength of material. The general procedures to have these quantities are described as follows. The detailed derivations and discussions of these equations can be found in [104, 108].

The first step is to estimate the reduced Young's modulus, E^*, by considering that

$$\frac{F_{\max}}{E^*} = 0.268536\left(0.9952495 - \frac{h_r}{h_m}\right)^{1.1142735} \tag{7-1}$$

where $F_{\max}$, h_r, and h_m are given from the individual load-penetration curve shown in Figure 7-1. The obtained reduced modulus, E^*, then is introduced in equation 7-2

$$\frac{1}{E^*\sqrt{A_m}}\frac{dF_{\max}}{dh}\bigg|_{h_m} = c^* \tag{7-2}$$

A_m, is directly measured during the test, and the other term in the r.h.s of eq.2 is obtained by derivation of the loading curve. c^* stands for the elasto-plastic deformation prior to the unloading. It is depending on the geometry of the indenter and on the extent of deformation. Table 7-1 gives the values of c^* for different deformations and a variety of indenter shapes.

Table 7-1 List of c^* given in Dao's study [108]

	Small deformation linear elastic solution	Large deformation elasto-plastic solution
Conical	1.128	1.1957
Berkovich	1.167	1.2370
Vickers	1.142	1.2105

The reduced modulus obtained from equation (7-1) allows to determine the Young's modulus of material, E as shown in eq.7-3 By giving the Young's modulus, E_i, and Poisson's ratio, ν_i, of indenter material (diamond), the value of E can be determined from

$$\frac{1}{E^*} = \frac{1-\nu^2}{E} + \frac{1-\nu_i^2}{E_i} \tag{7-3}$$

From the curvature C of the loading curve, one can get the representative stress via eq.

7-4

$$\frac{C}{\sigma_{0.033}} = -1.131\left[\ln\left(\frac{E^*}{\sigma_{0.033}}\right)\right]^3 + 13.635\left[\ln\left(\frac{E^*}{\sigma_{0.033}}\right)\right]^2 - 30.594\left[\ln\left(\frac{E^*}{\sigma_{0.033}}\right)\right] + 29.267 \tag{7-4}$$

Here $\sigma_{0.033}$ is the representative stress associated with Berkovich indenter, for a representative strain of 0.033.. Either Dao or Bucaille follow the same procedures presented above to determine E^*, A_m, E, and $\sigma_{0.033}$, but they did not use the same method to determine strain hardening exponent.

It has been shown that the equation (7-4) actually varies with the choice of representative strain (which is somehow arbitrary and may be different from 0.033). The variation of representative strain with different indenter geometries are summarized in Table 7-2. A general relation of the representative strain with the half tip-angle of the indenter was subsequently proposed as

$$\varepsilon_r = 0.105\cot\theta \tag{7-5}$$

Table 7-2 The representative strains associated with different included angle [104]

Inclined angle of indenter	Representative strain
70.3	0.033
60	0.0537
50	0.082
42.3	0.126

This finding motivated them to consider another way to determine the strain hardening exponent. By extending Dao's approach, Bucaille *et al.* proposed additional three dimensionless equations based on different representative strain

$$\frac{C}{\sigma_{0.0537}} = 0.06463\left[\ln\left(\frac{E^*}{\sigma_{0.0537}}\right)\right]^3 - 2.2102\left[\ln\left(\frac{E^*}{\sigma_{0.0537}}\right)\right]^2 + 21.589\left[\ln\left(\frac{E^*}{\sigma_{0.0537}}\right)\right] - 28.5741$$

$$\frac{C}{\sigma_{0.082}} = 0.02937\left[\ln\left(\frac{E^*}{\sigma_{0.082}}\right)\right]^3 - 0.9324\left[\ln\left(\frac{E^*}{\sigma_{0.082}}\right)\right]^2 + 8.4034\left[\ln\left(\frac{E^*}{\sigma_{0.082}}\right)\right] - 7.532$$

$$\frac{C}{\sigma_{0.126}} = 0.02842\left[\ln\left(\frac{E^*}{\sigma_{0.126}}\right)\right]^3 - 0.648\left[\ln\left(\frac{E^*}{\sigma_{0.126}}\right)\right]^2 + 4.9036\left[\ln\left(\frac{E^*}{\sigma_{0.126}}\right)\right] - 3.806$$

(7-6)

and a general form is given by

$$\frac{C_\theta}{\sigma_{r\theta}} = \tan^2\theta\left\{0.02552\left[\ln\left(\frac{E^*}{\sigma_{r\theta}}\right)\right]^3 - 0.72526\left[\ln\left(\frac{E^*}{\sigma_{r\theta}}\right)\right]^2 + 6.34493\left[\ln\left(\frac{E^*}{\sigma_{r\theta}}\right)\right] - 6.47458\right\}$$

(7-7)

In Bucaille's approach, the same specimen is indented by two different indenters of different shapes (one of them has to be Berkovich indenter). Then, the yield strength and strain hardening exponent are obtained s by solving

$$\begin{cases} \sigma_{0.033} = \sigma_y \left(1 + \varepsilon_{0.033} \dfrac{E}{\sigma_y}\right)^n \\ \sigma_{r\theta} = \sigma_y \left(1 + \varepsilon_{r\theta} \dfrac{E}{\sigma_y}\right)^n \end{cases} \tag{7-8}$$

The calculated flow strength and strain hardening exponent can be used further to describe the elasto-plastic behavior of material, which can be described by using the following relation (Ludwig's law).:

$$\sigma = \begin{cases} E\varepsilon, \sigma \le \sigma_y \\ K\varepsilon^n, \sigma > \sigma_y \end{cases} \quad , \quad K = E^n \sigma_y^{1-n} \tag{7-9}$$

7.2.2 The reliability of the processed data

It has to notice that the above procedures to process the raw data of nanoindentation are all based on idealized assumptions: perfect geometry of the indenter, absence of friction between the indenter and the tested material. In addition the validity of the results for hardness and modulus is very sensitive to thermal drifts and mechanical vibration. In addition, intrinsic problems with the indentation test have to be considered, such as pile-up and sink-in phenomena. Additional corrections are required to account for irregularities in the shape of the indenter, deflection of the loading frame, and pile-up and sink-in of material around the indenter. These corrections are described in detail in [104], we have applied all of them to our analysis. Figure 7-3 clearly gives the example showing how the pile-up and sink-in of specimen after indentation affects the penetrating height. The under- or over-estimation of the h_{max} are definitely expected to make the measured mechanical

properties to deviate from the actual values.

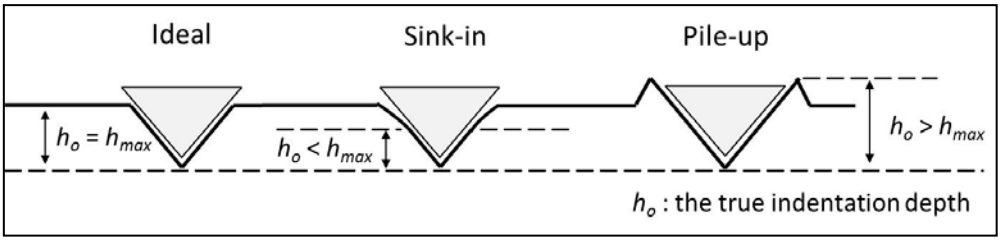

Figure 7-3 The illustration of sink-in and pile-up phenomena showing on the surface of specimen during indentation.

7.3 Methodology: Measurement of the Orowan contribution of interphase precipitation

The as-received material was taken as a reference to explain the way to determine the Orowan contribution of interphase precipitation because the precipitation hardening is the key strengthening mechanism in the present work. The microstructure parameters of the as-received material are summarized in Table 3-2. The initial microstructure state is composed by a mixture of ferrite and pearlite. It is worth noting that the major contribution of interphase precipitation to global strengthening comes from ferrite so that the contribution of precipitates into pearlite can be neglected. Consequently, all the strengthening contributions specifically to ferrite are considered and the local measurements in ferrite were then carried out by nanoindentation.

7.3.1. Orowan contribution

When we use the stress-strain curve of as-received material, it should be noted that the obtained curve represents actually the elasto-plastic behavior of ferrite together with pearlite. On the contrary, the results of nanoindentation reflect the

mechanical properties specifically for ferrite. In order to make a link between the macroscopic stress-strain curve incorporating a composite microstructure, and the local mechanics of nanoindentation, which focusses of ferrite hardened by precipitation, we implement the classical mean field approach [114]. By assuming the microscopic deformations in each phase are both uniform in ferrite and pearlite, respectively, the macroscopic deformation E of the heterogeneous media is the mean of the microscopic deformations. The flow stress is viewed as the average value of the local stresses of ferrite and pearlite, respectively. Both mean values are weighted with the respective fractions of the phases, i.e., the fraction of pearlite F and ferrite $(1 - F)$ [114].

$$\begin{aligned} dE &= (1-F)d\varepsilon_\alpha + Fd\varepsilon_p \\ \sum(E) &= (1-F)\sigma_\alpha(\varepsilon_\alpha) + F\sigma_p(\varepsilon_p) \end{aligned} \tag{7-10}$$

And then, the localization law can close the system. We have chosen the iso-work expression [114] which mimics in a simple way the fact that a softer phase bears a larger strain. This can be written as

$$\sigma_\alpha(\varepsilon_\alpha)d\varepsilon_\alpha = \sigma_p(\varepsilon_p)d\varepsilon_p \tag{7-11}$$

We are focusing on phenomena that occur on ferrite. The yield strength of ferrite containing precipitates results from the sum of different strengthening mechanisms, which can be formulated as [63] :

$$\Delta\sigma_y = \Delta\sigma_\circ + \Delta\sigma_{ss} + \Delta\sigma_{GB} + \sqrt{\Delta\sigma_{Dis.}^2 + \Delta\sigma_{Orowan}^2} \tag{7-12}$$

The terms in the square root are known precipitation hardening, $\Delta\sigma_{pp}$, representing the interaction of carbides with dislocations. Therefore, the Orowan contribution can be rewritten:

$$\Delta\sigma_{Orowan} = \sqrt{\left(\Delta\sigma_y - \Delta\sigma_\circ - \Delta\sigma_{ss} - \Delta\sigma_{GB}\right)^2 - \Delta\sigma_{Dis.}^2} \tag{7-13}$$

where $\Delta\sigma_y$ is the yield strength of ferrite with precipitates (measured experimentally by nanoindentation), $\Delta\sigma_\circ$ is the friction stress of ferrite, $\Delta\sigma_{ss}$ is the increment in strength by solid solution strengthening, $\Delta\sigma_{GB}$ is the increased strength by grain boundary strengthening and $\Delta\sigma_{Dis.}$ is the increased strength by dislocation strengthening.

In order to determine the Orowan contribution, we measure from nanoindentation $\Delta\sigma_y$, and the others contributions $\Delta\sigma_\circ$, $\Delta\sigma_{ss}$, $\Delta\sigma_{GB}$ and $\Delta\sigma_{Dis.}$ of the as-received material are evaluated from eq. (7-12). as follow [63]:

$\Delta\sigma_\circ$ = 54 MPa

$\Delta\sigma_{GB} = 17.4D^{-1/2} =$ 101.3 MPa

$\Delta\sigma_{ss} == 15.4\left[2.1(wt\%Mn) + 5.4(wt\%Si) + 23.4(wt\%C) + 23(wt\%N)\right] = 78.3$ MPa

The dislocation strengthening is determined by the following equation [64].

$$\Delta\sigma_{Dis.} = \zeta MGb\sqrt{\rho} \quad = 62 \text{ MPa} \tag{7-14}$$

where ζ is a Geometric constant and ρ is the dislocation density, which are set to be 0.435 and $5\times10^{13}\,\text{m}^{-2}$ (measured by TEM) [14]

7.3.2. Determination of $\Delta\sigma_y$ and main results

By following Bucaille's work, the two indenters, Berkovich and Cubic-Corner, are used to obtain the strain hardening exponent. It is worth noticing that in order to process the raw data of nanoindentation, the curvature of the loading curve is required. The equations have been proposed to estimate precisely these quantities. In the present analysis, it assumes that the loading and the penetration depth follows the relation

$$P = Ch^m \tag{7-15}$$

Generally, m is commonly suggested to be 2. It is expected that if we plot the loading P against h^m, a straight line would be obtained and the slope represents the value. Therefore, m is now a fitting parameter. Using the recorded P and h, it is found that a straight line is presented when m is equal to 1.95, which is close to the proposed magnitude.

The results are shown in Figure 7-4. It can be seen that the calculated representative stresses fall into two groups, contributed from ferrite and pearlite, respectively. The representative stress and strain are then calculated by equations 7-4

and 7-10; the results are given in Table 7-3.

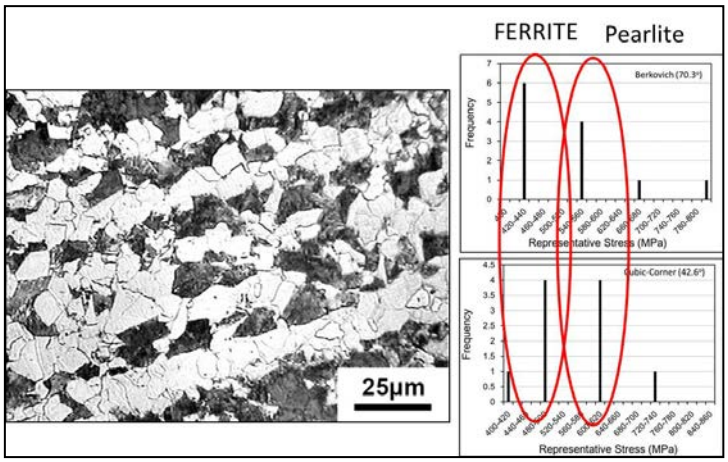

Figure 7-4 The microstructure of the as-received hot-drawn steel bar and the representative stress obtained by nano-indentation by using two different indenters.

Table 7-3 Mechanical properties of ferrite from nano-indentation of the as-received materials

Representative stress (MPa)		Yield strength (MPa)	Strain hardening exponent
Berkovich	Cubic-Corner	$\Delta\sigma_y^{nano}$	n
420	490	371	0.07

Using the results presented in Table 7-3, the stress-strain curve can be plotted and then compared to that obtained from the tensile test of the as-received material, as shown in Figure 7-5. Clearly, the yield strength measured by nanoindentation presents a great difference from that measured by tensile test. It has been highlighted previously that the yield stress obtained from the tensile test is actually a macroscopic indicator incorporating a level of microstructure consisting of ferrite with pearlite. However, the yield strength measured from nanoindentation test can be responsible specifically for one single ferrite grain only by the virtue of small indenter, as shown in the insert of Figure 7-5. Because the small size of indenter is (2 μm), small enough to fit inside a single grain of ferrite (22 μm), the grain boundary hardening can be

neglected at this level. As a consequence, the measurements by nanoindentation include the strengthening contributions from $\Delta\sigma_{\circ}$, $\Delta\sigma_{ss}$, and $\sqrt{\Delta\sigma_{Dis.}^2 + \Delta\sigma_{Orowan}^2}$. By the use of the magnitude estimated from equation (7-14), the values of the different contributions are able to separately defined, as shown in Figure 7-6.

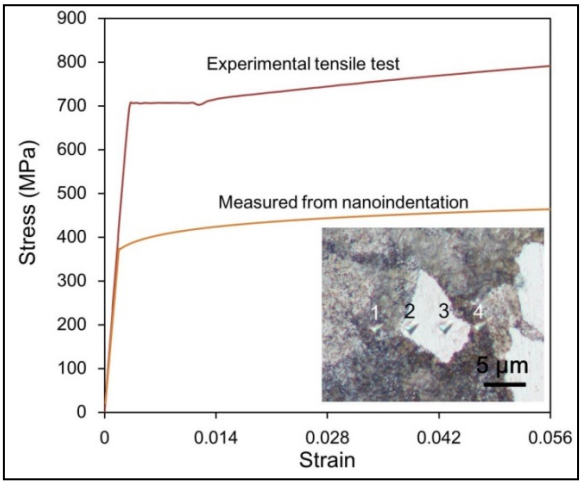

Figure 7-5 The measured stress-strain curves of tensile test and nanoindentation; an insert is given to demonstrate the size of indenter.

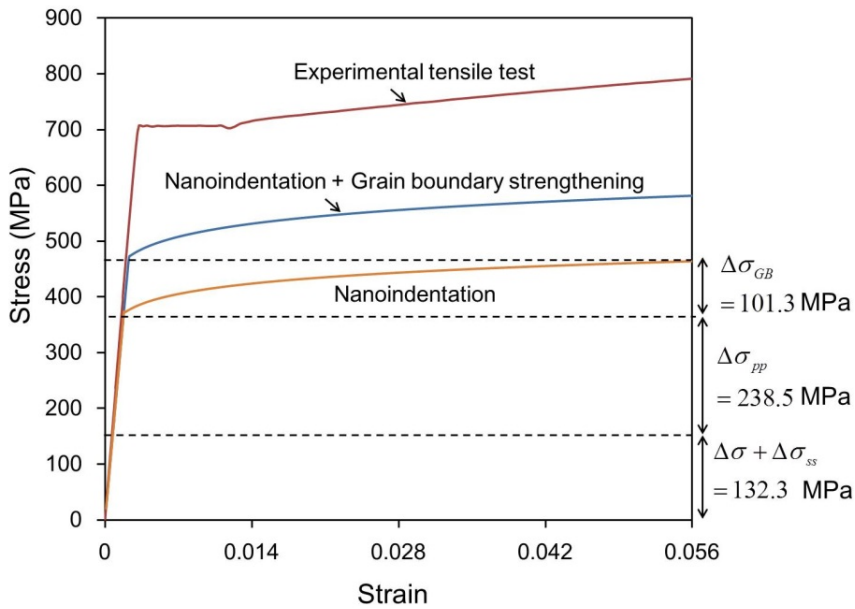

Figure 7-6 The different strengthening contributions according to the results of nanoindentation and to that estimated by equation 7-14, where $\Delta\sigma_{pp} = \sqrt{\Delta\sigma_{Orowan}^2 + \Delta\sigma_{Dis.}^2}$

7.4 Prediction of the Orowan contribution of ferrite strengthened by the interphase-precipitated carbides for different heating paths

By the use of the as-received materials, we have shown that the Orowan contribution can be extracted by nanoindentation, which is valuable to examine the precipitation hardening contribution in micro-alloyed steels. In order to examine how the interphase-precipitated carbide influences the strength of ferrite, specimens were isothermally transformed at three transformation temperatures to vary the carbide distribution. The heat treatments are presented in Figure 7-5.

The specimens are actually as the same as the ones studied in chapter 6. The phases showing in these specimens are:

a. Transformed at 670 ^{o}C: ferrite and martensite
b. Transformed at 650 ^{o}C: ferrite and pearlite
c. Transformed at 630 ^{o}C: ferrite and pearlite

The precipitation hardening depends obviously on the precipitate size, on the sheet spacing and on the inter-precipitate distance in a given sheet. These features have been studied thoroughly in chapter 6, both from an experimental viewpoint and from a modeling viewpoint. The sheet spacing is mainly controlled by the driving force for γ/α transformation, whereas the two other parameters reflect mainly the driving force for precipitation. It is in principle possible to vary these various parameters independently so that the evaluation of the hardening potential may be very relevant.

The depth-penetrating curves obtained by using two different indenters are shown in Figure 7-6, indicating the shape of curve varies with different precipitate states.

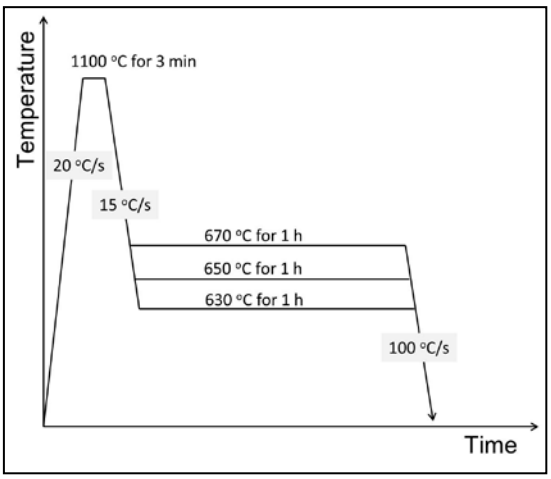

Figure 7-5 The heat treatments of the specimens

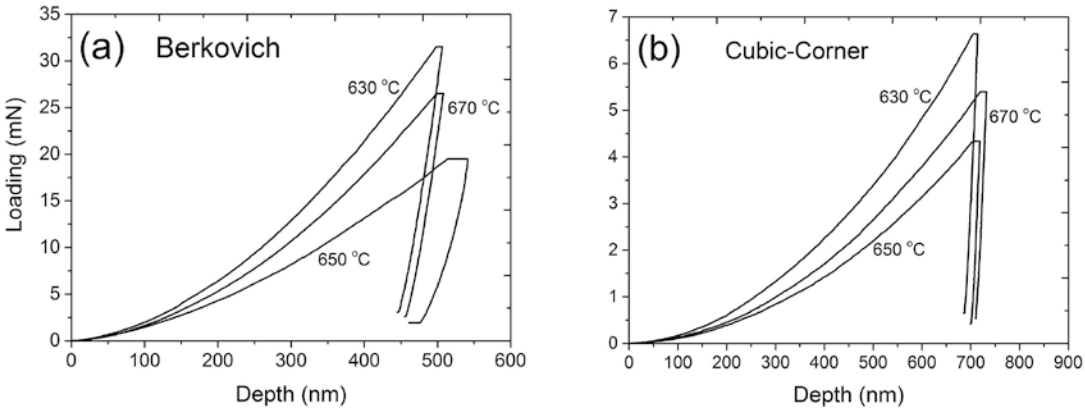

Figure 7-6 The obtained typical depth-penetrating curves of the steel studied by using (a) Berkovich indenter, and (b) Cubic-Corner indenter.

7.4.1 Calculation of the Orowan contribution

The strengthening mechanism of the interphase-precipitated carbides had been studied initially by Batte [66]. For the ferrite strengthened by the interphase-precipitated carbides, the yield strength is mainly determined by the sheet

spacing, the particle spacing, and the carbide mean radius. It has shown that the total yield strength is mainly contributed by the effects of precipitation hardening and grain boundary strengthening, and the Orowan strengthening can be exclusively extracted by nanoindentation. In the following section, the Orowan strengthening of ferrite containing the interphase-precipitated carbide are discussed according to the results of nanoindentation and theoretical calculations.

$\Delta\sigma_{Orowan}$ is expressed as the Orowan equation by considering the obstacle spacing on the slip plane [70]:

$$\Delta\sigma_{Orowan} = \kappa M_T G \frac{b}{L} \tag{7-16}$$

where κ is a correction factor ranged from 0.7-1.1 [72], L is defined as the square root of the mean slip area per carbide particle [70, 72], b is the Burger's factor, M_T is the Taylor factor, and G is the shear modulus. For the carbides arranging in the manner of interphase precipitation, the sheet spacing and the particle spacing of the interphase-precipitated carbides are used to determine the magnitude of L [66], which can be written as

$$L = \sqrt{r_1 r_2} \tag{7-19}$$

where r_1 is the mean linear inter-particle spacing along the intersection between the slip plane and the sheet plane of interphase precipitation, and r_2 is the mean projected value of the perpendicular sheet spacing. The magnitudes of r_1 and r_2 can be estimated by the measured particle spacing, b_p, sheet spacing, λ, carbide aspect ratio, p,

and carbide size, d which are expressed as [14]:

$$r_1 = \frac{b_p^2}{d} + \frac{\pi d}{4} - \frac{d}{p \sin\theta} \tag{7-20}$$

$$r_2 = \frac{\lambda - d\sin\theta}{\sin\varphi} \tag{7-21}$$

The measured particle spacing, b_p, sheet spacing, λ, carbide aspect ratio, p, and carbide size, d are measured by TEM (see Table 6-1). θ is the angle between carbide broad plane normal and the sheet plane normal, and φ is the angle between sheet plane normal and the slip plane normal. The geometric orientations of the sheet plane, carbide platelets, and the slip plane are illustrated in Figure 7-7.

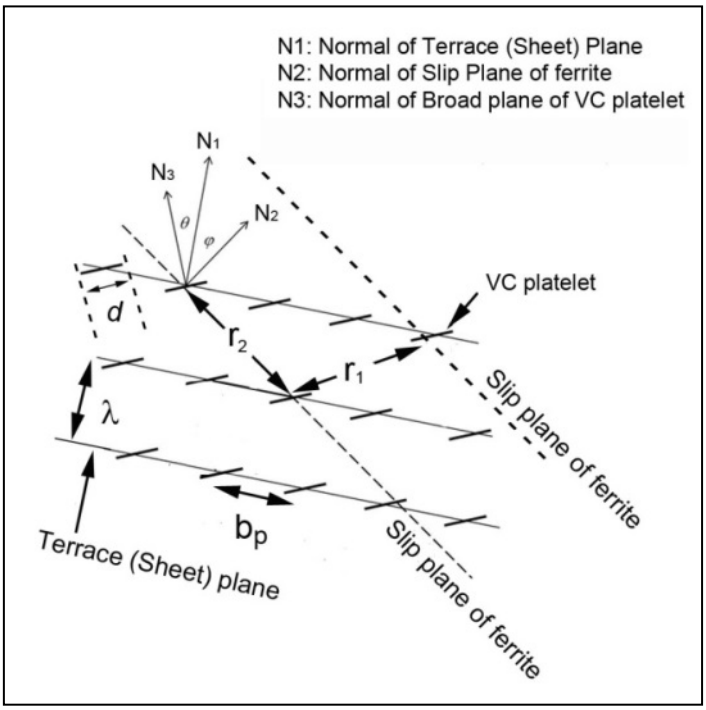

Figure 7-7 Schematic illustration of the geometric orientation of the sheet plane, carbide platelet, and the slip plane.

For the geometric factors $sin\theta$ and $sin\varphi$, they have been determined as 0.61 and 0.33,

respectively [14] but they can be indeed considered in this study as fitting parameters. Using the measured characteristic features of the interphase-precipitated carbides (Table 6-1 The features of interphase precipitation measured by TEM), the Orowan strengthening contributing to the yield strength by these carbides, $\Delta\sigma_{Orowan}$, is estimated. The fitting parameters κ and $sin\theta$ and $sin\varphi$ used in the calculations are 0.8, 0.2, and 0.2, respectively.

7.4.2 Comparison between the calculated Orowan contribution and the measured one by nanoindentation

It has been noted that the strength we obtained by nanoindentation does not include grain boundary contribution. Each strengthening contribution to the global ferrite strength is then summarized in Table 7-4. The precipitation hardening extracted from the results of nanoindentation, $\Delta\sigma_{pp}^{nano}$ is indicated. The comparison of the theoretical Orowan strengthening, $\Delta\sigma_{Orowan}^{theorectical}$, to that measured by nanoindentation, $\Delta\sigma_{Orowan}^{nano}$ is shown in Table 7-4.

Table 7-4 The strengthening contribution to the global strength of ferrite in the steel studied

Temperature (°C)	Strengthening contribution (MPa)							
	$\Delta\sigma_y$	$\Delta\sigma_\circ$	$\Delta\sigma_{ss}$	$\Delta\sigma_{GB}$	$\Delta\sigma_{pp}^{nano}$	$\Delta\sigma_{Dis.}$	$\Delta\sigma_{Orowan}^{nano}$	$\Delta\sigma_{Orowan}^{theorectic}$
630 °C	627.7	54.0	78.3	212.4	283.2	62.0	276.1 ± 20.6	302.1
650 °C	444.4	54.0	78.3	131.7	180.4	62.0	170.4 ± 18.1	216.9
670 °C	469.5	54.0	78.3	106.2	231.7	62.0	222.5 ± 17.3	224.5

With the aid of Bucaille approach, the strain hardening exponent of ferrite can also be determined, as shown in Table 7-5. In normal ferritic steel, the magnitude of *n* is approximately 0.1 [104]. The estimated *n* of the steel studied is larger than this value, showing the interphase-precipitated carbides increase the plasticity of ferrite. With the global strength of ferrite given in Table 7-4, the determined *n* can further help us to calculate the stress-strain curve for ferrite at the different transformation temperature by eq. (7-9), as shown in Figure 7-8.

Table 7-5 The estimated strain hardening exponent at different transformation temperature

Transformation temperature (^{o}C)	670 ^{o}C	650 ^{o}C	630 ^{o}C
Strain hardening exponent, *n*	0.18	0.17	0.2

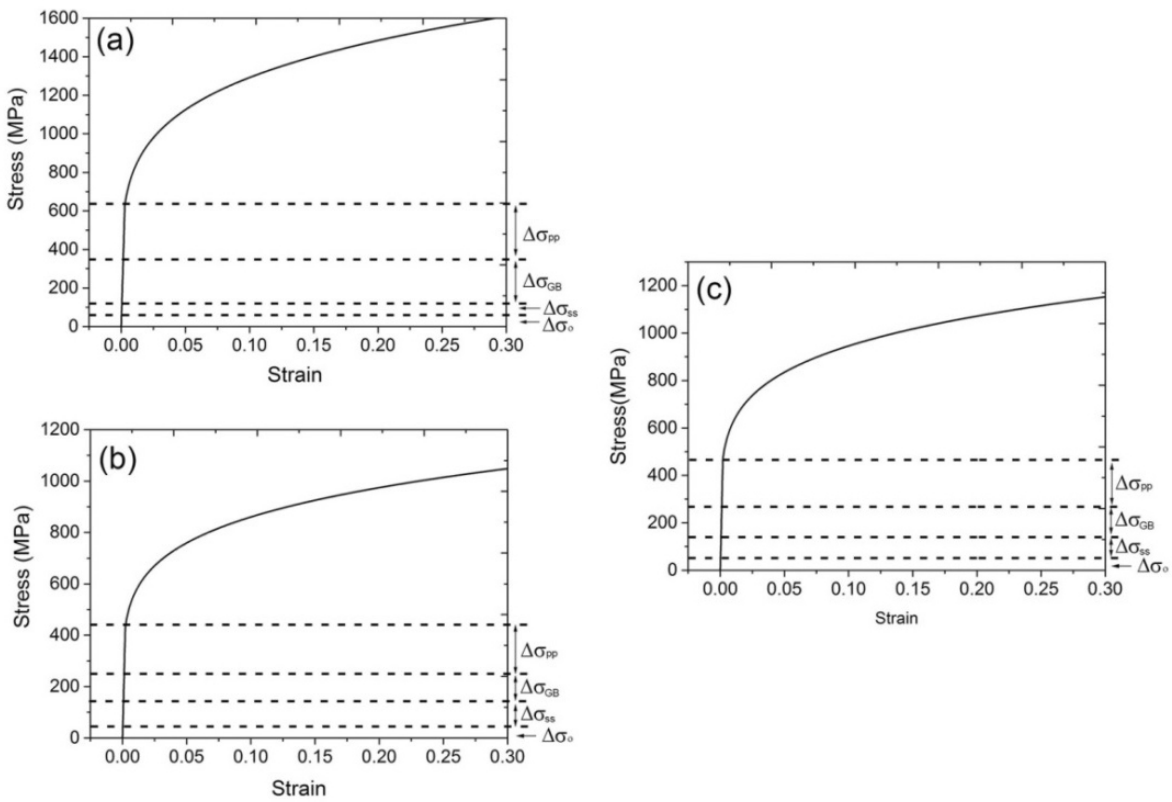

Figure 7-8 The calculated stress-strain curve for ferrite transformed at (a) 630 ^{o}C, (b) 650 ^{o}C, and (c) 670 ^{o}C; the strengthening contributions to the global strength of ferrite are indicated

7.5 Discussion

7.5.1 The complex influence of heat treatment temperatures

For the ferrite containing the interphase-precipitated carbides, its strength was reported to have an inverse relationship with the sheet spacing [15, 66]. A higher transformation temperature leads to a wider sheet spacing [2]. Therefore, the strength of ferrite at 670 ^{o}C is expected to be the lowest one among the heat treated steels studied. However, the measured strength shows that the yield strength of the ferrite formed at 670 ^{o}C is higher than that at 650 ^{o}C, indicating that sheet spacing is not the only controlling parameter. In precipitation-hardened steels, the carbide distribution (sheet spacing and particle spacing) and its size both are known to have strong influences on the yield strength [19, 67]. In Figure 6-1 and Table 6-1, we have shown experimentally and theoretically that the particle spacings at the three transformation temperatures are approximately the same but with different sheet spacing and different particle size. For the results of steel transformed at 670 ^{o}C and 650 ^{o}C, we can evaluate experimentally the influences of the two latter microstructural parameters.

It is known that the sheet spacing and the carbide radius both increase with increasing the transformation temperature but the relative contributions of each evolution to the $\Delta\sigma_{Orowan}$ are opposite. By increasing the sheet spacing, the $\Delta\sigma_{Orowan}$ tends to decrease, whereas by increasing carbide size $\Delta\sigma_{Orowan}$ tends to increase. It seems that the effect of carbide size dominates: an increase in temperature from 650 ^{o}C to 670 ^{o}C leads to increase in yield stress. Conversely, as the transformation temperature decreases from 650 ^{o}C to 630 ^{o}C, the carbide radii remain approximately

the same (~ 3-4 nm), the total yield strength becomes solely dependent on the sheet spacing, and it increases.

Another interesting feature can be seen by taking the carbide volume fraction into our considerations, which can be determined by the measured sheet spacing, particle spacing, and carbide radius:

$$f_v = \frac{4}{3}\pi N R^3 = \frac{4}{3}\pi \frac{1}{\lambda b_p^2} R^3 \tag{7-27}$$

The temperature-dependences of microstructural parameters and the theoretical Orowan strengthening are given in Figure 7-9.

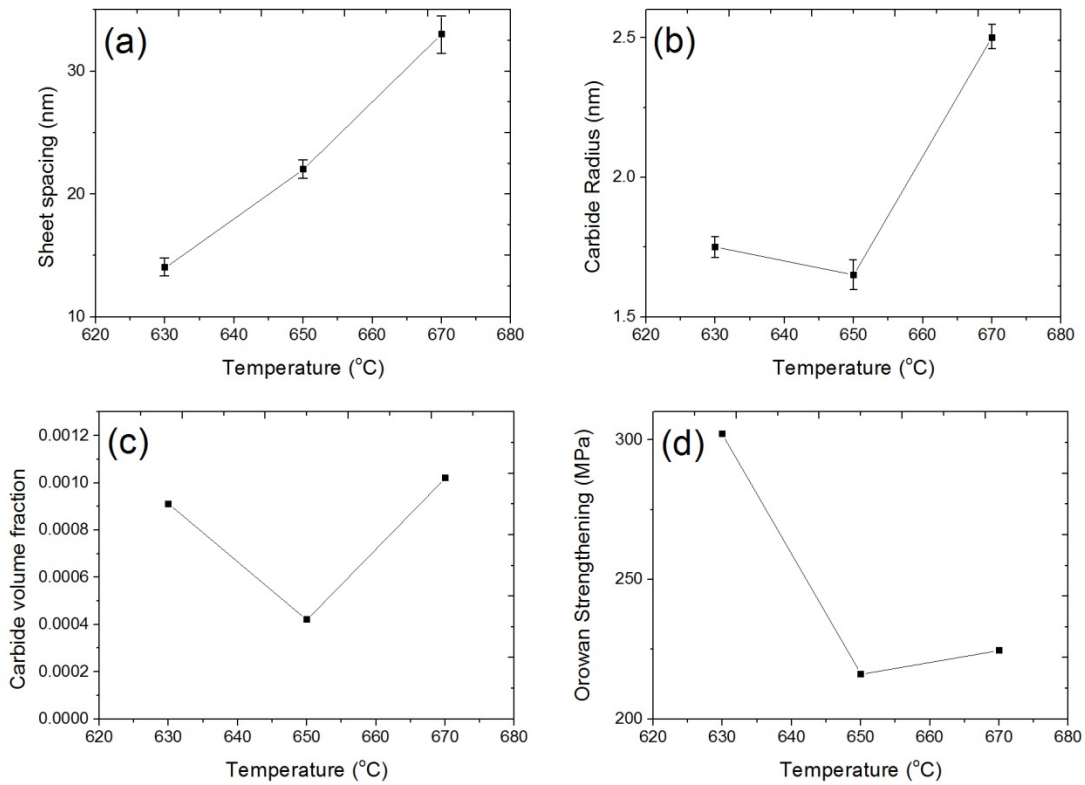

Figure 7-9 The temperature-dependence of (a) sheet spacing, (b) carbide radius, (c) carbide volume fraction, and (d) theoretical Orowan strengthening with transformation temperatures.

It is noticed that the similar carbide volume fraction in ferrite at 630 ^{o}C and 670 ^{o}C is approximately the same (~ 0.1%) but results in significant difference in Orowan strengthening contribution. These results indicate the importance of the carbide distributions (the sheet spacing and the particle spacing) and the carbide radius on the resulted strengthening effects, which are associated with the features of austenite-to-ferrite transformation kinetics (TTT diagram) and with carbide nucleation and growth (PTT diagram).

In principal, the experimental TTT diagram is known in the absence of carbide precipitation. The interplay between the precipitation and phase transformation is two folds: via the pinning of the interface and via the modification of austenite-to-ferrite transformation driving force via carbon pumping. A comprehensive model of interphase precipitation would take into account this latter coupling. It is beyond the purpose of the present thesis. The PTT and TTT diagrams would have to be established experimentally, which is a substantial amount of additional work.

The following section is about to deal with understanding of the evolution of Orowan strengthening with the microstructural features of interphase precipitation.

7.5.2 The optimization of arrangement of the interphase-precipitated carbides under a fixed carbide volume fraction condition

The Figure 7-9(c) has shown that even though the carbide volume fraction is the same, the Orowan strengthening contribution might still be varied greatly by the nature of carbide arrangement. According to eq. 7-24, the $\Delta\sigma_{Orowan}^{IP}$ is described in terms of three precipitation microstructural parameters: the sheet spacing (λ), the

particle spacing (b_p), and the carbide radius (R). The carbide volume fraction is given by eq. (7-27)

If f_v is fixed, the r.h.s. of eq. (7-27) could have different combinations of λ, b_p, and R. The Orowan strengthening contribution consequently changes with different precipitation microstructural parameters. The idea here is to understand whether there is a combination of precipitate state (λ, b_p, and R) leading to the highest or the lowest $\Delta\sigma_{Orowan}^{IP}$ under a fixed f_v condition.

To have such a figure, the f_v used for the calculation is set to be 6.7×10^{-3}. λ and R are the variables; b_p is then imposed since f_v is given.

$$b_p = \sqrt{4\pi R^3/3\lambda f_v} \tag{7-28}$$

The variation of the $\Delta\sigma_{Orowan}^{IP}$ with the λ and R is shown in Figure 7-10. Figure 7-10(b) is a projection of Figure 7-10(a) and the contour represents constant carbide radius. Along the contour in Figure 7-10(b), there exists a sheet spacing making the Orowan strengthening to be a minimum. As this sheet spacing is determined, the particle spacing can be obtained from eq. (7-28). Taking carbide radius as 5 nm as an example, the lowest Orowan strengthening is about 243.0 MPa, and the sheet spacing and particle spacing are 22 nm and 60 nm, respectively.

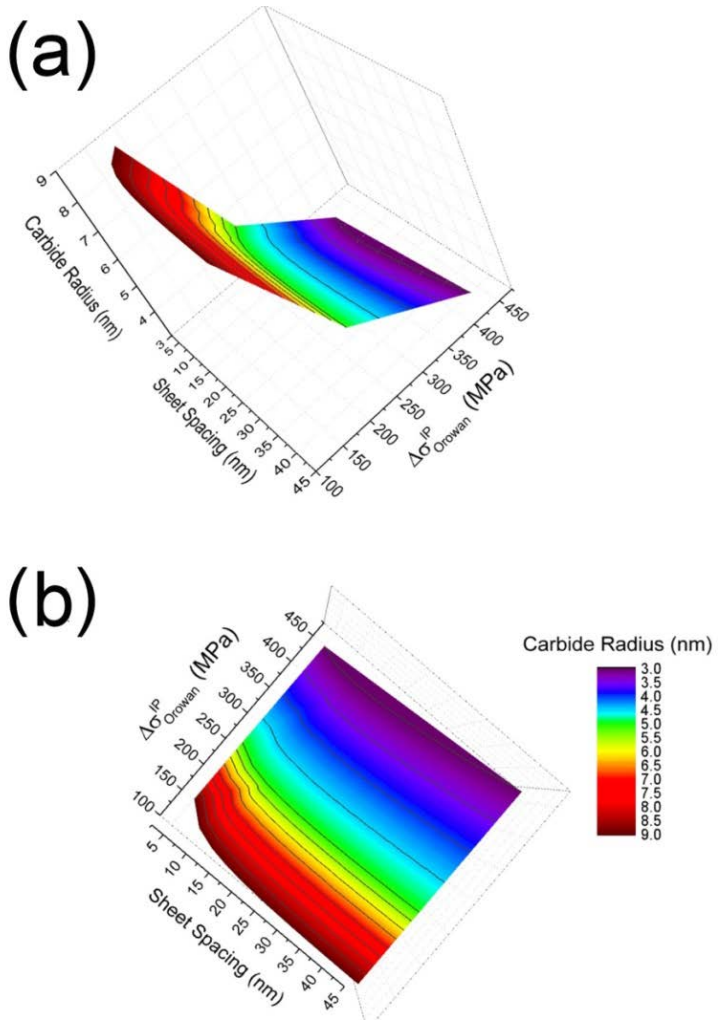

Figure 7-10 The evolution of Orowan strengthening with the sheet spacing and carbide radius. The carbide volume fraction is given as 0.0067.

7.5.3 Effects of Carbide distribution on Orowan strengthening: Comparison of the contribution of the random array carbides with the interphase-precipitated carbides.

The distinctive feature of the interphase-precipitated carbide is the periodically carbide nucleation associated with the progressive of austenite-to-ferrite transformation, resulting in a sheeted structure in the ferrite matrix. It is interesting to compare the contributed Orowan strengthening of interphase precipitated carbides, $\Delta\sigma^{IP}_{Orowan}$, to that of carbides in random array, $\Delta\sigma^{Random}_{Orowan}$. For the

interphase-precipitates, the obstacle spacing, L, given in eq. (7-19) has to be considered. When the carbides are randomly distributed in the matrix, L can be written as a function of carbide volume fraction, f_v, and the carbide radius, R:

$$L_{Random} = 2R\sqrt{\frac{\pi}{6f_v}} \tag{7-29}$$

Because of $f_v = 4\pi NR^3/3$, the $\Delta\sigma_{Orowan}^{Random}$ can subsequently be expressed as

$$\Delta\sigma_{Orowan}^{Rand} = \kappa M_T Gb\sqrt{2NR} \tag{7-30}$$

where N is the number of particle per unit volume. From eqs. 7-16 to 7-21, the $\Delta\sigma_{Orowan}^{IP}$ can be written as

$$\sigma_{Orowan}^{IP} = \frac{\kappa M_T Gb}{\sqrt{\left(\frac{b_p^2}{2R} + \frac{\pi R}{2} - \frac{2R}{p\sin\theta}\right)\left(\frac{\lambda - 2R\sin\theta}{\sin\varphi}\right)}} \tag{7-31}$$

Taking into account that $N = 1/\lambda b_p^2$, we could have the ratio of $\Delta\sigma_{Orowan}^{IP}/\Delta\sigma_{Orowan}^{Random}$ in the form of:

$$\left(\frac{\Delta\sigma_{Orowan}^{IP}}{\Delta\sigma_{Orowan}^{Rand}}\right) = \sqrt{\frac{\lambda b_p^2}{2R\left(\frac{b_p^2}{2R} + \frac{\pi R}{2} - \frac{2R}{p\sin\theta}\right)\left(\frac{\lambda - 2R\sin\theta}{\sin\varphi}\right)}} \tag{7-32}$$

According to eq. (7-32), the variation of $\Delta\sigma_{Orowan}^{IP}/\Delta\sigma_{Orowan}^{Random}$ with different combination of λ(or b_p) and R can be presented for a given b_p (or λ), as shown in Figure 7-11

eq. (7-32) can also be re-written in terms of f_v and a normalized parameter of precipitate state, λ/R:

$$\left(\frac{\Delta\sigma_{Orowan}^{IP}}{\Delta\sigma_{Orowan}^{Rand}}\right)=\sqrt{\frac{\sin\varphi}{\left(\frac{R}{\lambda}+\frac{3f_V}{4\pi}\left[1-\frac{4}{\pi}\frac{1}{p\sin\theta}\right]\right)\left(\frac{\lambda}{R}-2\sin\theta\right)}} \tag{7-33}$$

The variation of $\Delta\sigma_{Orowan}^{IP}/\Delta\sigma_{Orowan}^{Random}$ can subsequently be visualized in a different way, as shown in Figure 7-12. With a larger carbide radius (Figure 7-11(c)) or with a smaller ratio of λ/R (Figure 7-12(c)), the interphase-precipitated carbides could contribute a higher $\Delta\sigma_{Orowan}$, leading the ratio $\Delta\sigma_{Orowan}^{IP}/\Delta\sigma_{Orowan}^{Random}$ to be greater than one. It is interesting to note that the carbides arranging in random array generally lead to a higher $\Delta\sigma_{Orowan}$ than the interphase-precipitated carbides. At first sight, this result is surprising. In the past decades, the interphase precipitation was proposed to be a desire carbide distribution to give a significant strengthening effect on ferrite strength [15, 18, 66], but quantitative analysis was never made to compare $\Delta\sigma_{Orowan}^{IP}$ and $\Delta\sigma_{Orowan}^{Random}$. Indeed, interphase precipitation allows us to obtain a very fine microstructure with very small distances. Usual bulk precipitation would lead to a less refined microstructure. That's why interphase precipitation is reputed to be desirable. If one were able to obtain the same number of particles with similar sizes in a randomly distributed way, the resulting hardening would be better.

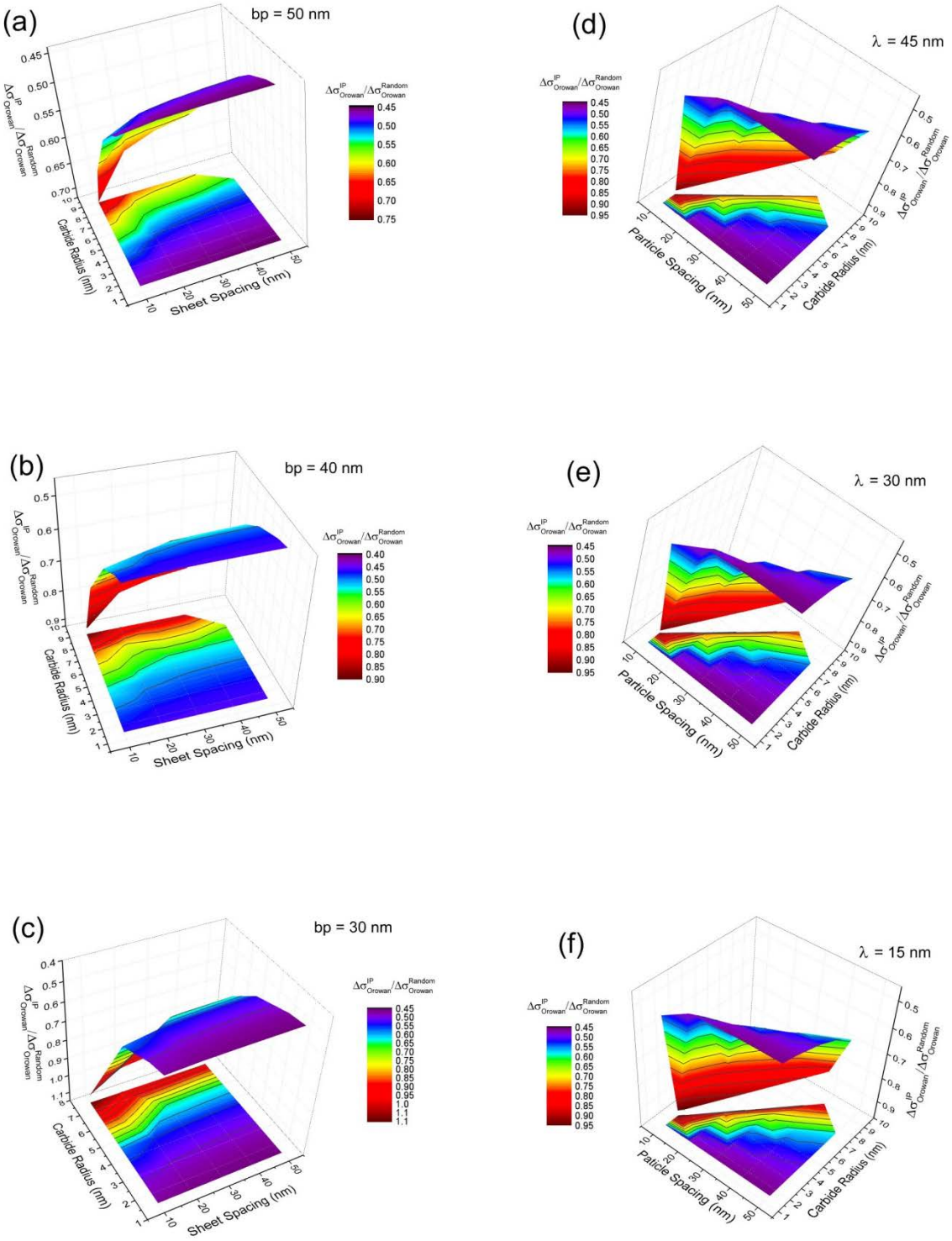

Figure 7-11 The variation of the ratio of Orowan strengthening for interphase-precipitated carbide to that for random array carbide with carbide radius. (a-c) the particle spacing is fixed, and (d-f) the sheet spacing is fixed.

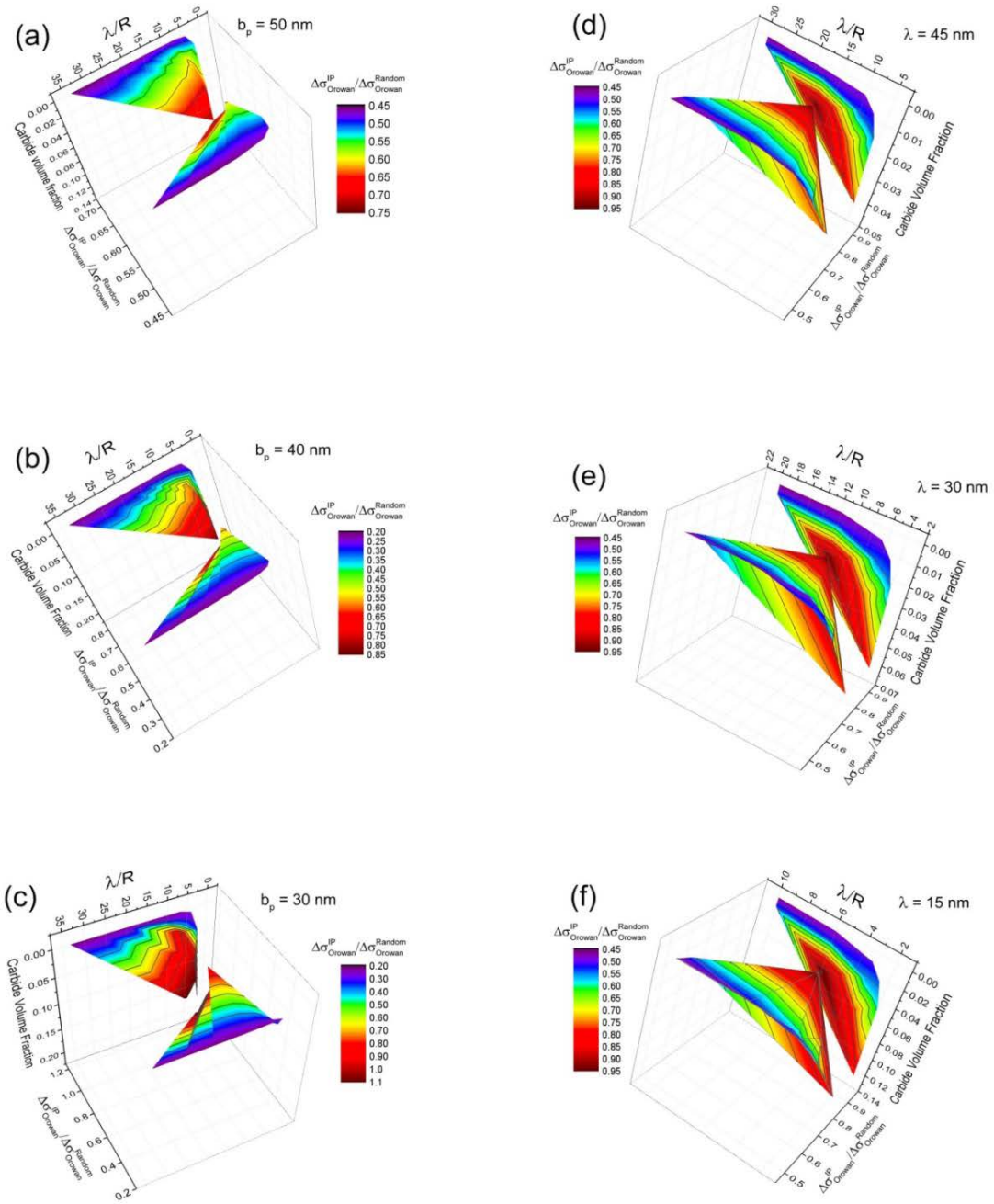

Figure 7-12 The ratio varying with the carbide volume fraction, f_v and a normalized precipitate state parameter, λ/R. (a-c) the particle spacing is fixed, and (e-f) the sheet spacing is fixed.

7.6 Conclusions

The ferrite strengthened by the interphase-precipitated carbides is examined by nanoindentation. By the virtue of small indenter, the local mechanical properties of

ferrite phase can obtained. The measured strength results from the ferrite friction stress, the solid solution strengthening, and the precipitation hardening. With Dao's and Bucaille's dimensionless equations, the estimated yield strength and strain hardening exponent enable us to have the stress-strain curve of material. The present approach shows that the Orowan strengthening of the interphase-precipitated carbides can be extracted and is in good agreement with the theoretical values.

The measured strengths are studied in connection with the microstructure. We have shown that for the ferrite transformed at 650 ^{o}C and 670 ^{o}C, the particle spacing did not change greatly but the sheet spacing and the carbide radius increase with increasing the temperature. The measured higher strength of ferrite at 670 ^{o}C demonstrates the contribution of carbide radius to the Orowan strengthening. The theoretical strength and the measured one are in agreement with each other.

The measured microstructural parameters are used to determine the variation of carbide volume fraction with the transformation temperature. It shows that the carbide volume fractions of ferrite transformed at 670 ^{o}C and 630 ^{o}C are the same but result in significant difference in Orowan strengthening. A 3D mapping is then developed to see the effect of carbide arrangement of interphase precipitation on the Orowan strengthening contributions. It shows that at a fixed carbide volume fraction, there is a combination of microstructural parameters leading the Orowan strengthening to be a minimum.

Finally, the interphase-precipitated carbides is then compared to that of the random array carbides, showing that the latter precipitate mode generally leads to a better strengthening contribution. The results indicate that if one were able to obtain the same number of particles with similar sizes in a randomly distributed way, the resulting hardening would be better.

Chapter 8

General Conclusions and Perspectives

The present thesis investigates the interphase precipitation in a medium-carbon vanadium-alloyed steel. The microstructure of the interphase-precipitated carbide is examined by TEM and the conditions for the developments of the fibrous carbide are discussed. A model is then developed to predict the characteristic features of the interphase-precipitated carbide, and the observed microstructure is incorporated with this model. The ferrite strengthened by the interphase-precipitated carbide at different transformation temperatures is examined by nanoindentation. The general conclusions of these works are summarized as follows:

a. The attractive mechanical properties of UHSB are mainly attributed from the interphase-precipitated carbide, the refined ferrite grain size, and the finer pearlite spacing. The contributed strengths of the interphase-precipitated carbide and the refined grain size are estimated to be approximately 300 MPa and 200 MPa, respectively.
b. The higher transformation temperature, the incoherent ferrite/austenite interface, and the slower transformation rate were considered to be the conditions for carbide fiber development. However, the present EBSD examination on the ferrite containing carbide fiber show that the coherency of ferrite/austenite interface would not be the factor determining carbide morphologies. It is proposed that the appearance of carbide is actually an issue of thermodynamic and kinetic of austenite-to-ferrite transformation and carbide nucleation.
c. A semi-analytical model, the superledge model, is then proposed to describe the

formation of interphase-precipitated carbide associated with the ledge mechanism of austenite-to-ferrite transformation.

d. The proposed superledge model examines the sheet spacing of the interphase-precipitated carbide in the sample transformed at a lower transformation temperature (< 700 ^{o}C) and the predictions are in good agreements with the experimental data. As the transformation temperature increases, vanadium acquires sufficient thermal energy to diffuse, which means that the diffusion path would not be limited to be along the ferrite/austenite interface. The volume diffusion of solute is considered.

e. The evolutions of the characteristic features of interphase precipitation are firstly revealed by considering the mass balance of carbon and vanadium with the progressive of austenite-to-ferrite transformation. It is found that the sheet spacing becomes finer as the transformation proceeds, exhibiting the same tendency observed in Murakami's work. The particle spacing and the overall interface velocity evolve in an opposite trend with the progressive of transformation, which is consistent with the metallurgical understandings. The characteristic features of interphase precipitation now are predicted as a range, providing a new approach to describe the interphase precipitation.

f. A model of the formation mechanism of carbide fiber is proposed, based on the present superledge model. The driving force for the austenite-to-ferrite transformation is expected to decrease in the progressive of transformation.The development of carbide fiber occurs when the superledge is unable to unpin from the pinning carbides anymore. Based on this proposition, the particle spacing is equal to the spacing of carbide fiber. The spacing of carbide fiber are measured to be greater than that of interphase precipitation. This result indicates the carbide

nucleation rate and the driving force of austenite-to-ferrite transformation control the occurrence of carbide fiber. In addition, it also shows that the carbide fiber occurs at the later stage of austenite-to-ferrite transformation, which is in agreement with previous proposition.

g. The ferrite strengthened by the interphase-precipitated carbides is examined by nanoindentation. It is noted that the measured strength does not consider the grain boundary strengthening by the virtue of small indenter. The yield strength and the strain hardening exponent can be estimated, which are in agreement with the experimental data. The yield strength of the sample transformed at 670 ^{o}C is found to be larger than that at 650 ^{o}C, showing that the carbide size at the higher transformation temperature provides a significant strengthening effect.

h. The contribution of the arrangement of interphase-precipitated carbides to the Orowan strengthening is discussed. With a large carbide radius (> 9 nm) and a finer sheet (or particle) spacing (< 10 nm), the interphase precipitation is able to give a higher Orowan strengthening than the carbides distributing in a random array.

i. A 3D mapping of the precipitate states (sheet spacing, particle spacing, and carbide radius) is presented to show the evolution of Orowan strength with different combination of characteristics of the interphase-precipitated carbides. With a constant carbide volume fraction condition, it shows that the Orowan strength would pass through a minimum, indicating the *worst* arrangement of interphase-precipitated carbides. The 3D mapping for the steel studied is then established at the different transformation temperatures. With the measured carbide radius, the sheet spacing and the particle spacing are considered as variables. According to these figures, the Orowan strengthening with different

precipitate states can be predicted and is found to be consistent with the results of nanoindentation.

From here, the future works can be seen in four directions:

a. Obtaining and modeling the completed TTT and PTT diagrams for the system, and compare it with the prediction of the comprehensive model (i.e. treating more accurately the partition of carbon). This could be naturally extended to the interphase precipitation into pearlite.
b. Follow a route of alloying design, exploring the influence of vanadium content and comparing with the prediction of the model.
c. A systematic investigation of mechanical properties beyond the yield stress: this would require testing on sheets and analyzing more in detail work hardening and formability.
d. The strengthening effect of fibrous carbide on the global strength of ferrite can be studied.

References

[1] H. Aoyama, Design of Modern Highrise Reinforced Concrete Structures, Imperial College Press, 2001.

[2] R.W.K. Honeycombe, Metallurgical Transactions a-Physical Metallurgy and Materials Science, 7 (1976) 915-936.

[3] D.V. Edmonds, Journal of the Iron and Steel Institute, 210 (1972) 363-&.

[4] G.L. Dunlop, C.J. Carlsson, G. Frimodig, Metallurgical Transactions a-Physical Metallurgy and Materials Science, 9 (1978) 261-266.

[5] F.A. Khalid, D.V. Edmonds, Mater. Sci. Technol., 9 (1993) 384-396.

[6] G. Fourlaris, A.J. Baker, G.D. Papadimitriou, Acta Metallurgica Et Materialia, 43 (1995) 3733-3742.

[7] F.B. Pickering, B. Garbarz, Mater. Sci. Technol., 5 (1989) 227-237.

[8] D. Raynor, J.A. Whiteman, Honeycom.Rw, Journal of the Iron and Steel Institute, 204 (1966) 349-&.

[9] J. Todd, P. Li, S. Copley, Metallurgical and Materials Transactions A, 19 (1988) 2133-2138.

[10] P.R. Rios, Journal of Materials Science, 30 (1995) 1872-1878.

[11] R. Okamoto, J. Agren, Acta Materialia, 58 (2010) 4791-4803.

[12] P. Li, J.A. Todd, Metallurgical Transactions a-Physical Metallurgy and Materials Science, 19 (1988) 2139-2151.

[13] R. Lagneborg, S. Zajac, Metall. Mater. Trans. A-Phys. Metall. Mater. Sci., 32 (2001) 39-50.

[14] H.-W. Yen, P.-Y. Chen, C.-Y. Huang, J.-R. Yang, Acta Materialia, 59 (2011) 6264-6274.

[15] D.V. Edmonds, Metallurgical Transactions, 4 (1973) 2527-2533.

[16] S. Shanmugam, M. Tanniru, R.D.K. Misra, D. Panda, S. Jansto, Mater. Sci. Technol., 21 (2005) 883-892.

[17] J.A. Todd, P. Li, Metallurgical Transactions a-Physical Metallurgy and Materials Science, 17 (1986) 1191-1202.

[18] R.M. Brito, H.J. Kestenbach, Journal of Materials Science, 16 (1981) 1257-1263.

[19] H.J. Kestenbach, J. Gallego, Scripta Materialia, 44 (2001) 791-796.

[20] M.D.C. Sobral, P.R. Mei, H.J. Kestenbach, Journal of Nanoscience and Nanotechnology, 10 (2010) 1235-1240.

[21] M. Hillert, The role of interface in phase transformations, The mechanism of phase transformation in crystalline solid, 1968.

[22] S.A. Hackney, G.J. Shiflet, Scripta Metallurgica, 19 (1985) 757-762.

[23] G. Baro, H. Gleiter, Acta Metallurgica, 22 (1974) 141-143.

[24] R.C. Ecob, B. Ralph, Acta Metallurgica, 29 (1981) 1037-1046.

[25] T.B. Massalski, W.A. Soffa, D.E. Laughlin, Metall. Mater. Trans. A-Phys. Metall. Mater. Sci., 37A (2006) 825-831.

[26] K.C. Russell, Adv. Colloid Interface Sci., 13 (1980) 205-318.

[27] A.T.B. Davenport, F. G.; Honeycombe, R. W. K., Metal Science, 2 (1968) 104-106.

[28] R.M. Smith, Dunne, D.P., Mater. Forum, 11 (1988) 166.

[29] A.T. Davenport, R.W.K. Honeycome, Proceedings of the Royal Society of London Series a-Mathematical and Physical Sciences, 322 (1971) 191-&.

[30] C. Atkinson, Proceedings of the Royal Society of London Series a-Mathematical Physical and Engineering Sciences, 378 (1981) 351-368.

[31] C. Atkinson, Proceedings of the Royal Society of London Series a-Mathematical Physical and Engineering Sciences, 384 (1982) 107-133.

[32] M. Enomoto, Acta Metallurgica, 35 (1987) 935-945.

[33] M. Enomoto, Acta Metallurgica, 35 (1987) 947-956.

[34] R.A. Ricks, P.R. Howell, Acta Metallurgica, 31 (1983) 853-861.

[35] R.A. Ricks, P.R. Howell, Journal of Materials Science, 18 (1983) 3393-3398.

[36] J.H. Beatty, G.J. Shiflet, MTA, 19 (1988) 1617-1620.

[37] A.D. Batte, Honeycom.Rw, Journal of the Iron and Steel Institute, 211 (1973) 284-289.

[38] J.H. Woodhead, (1979).

[39] H. Bhadeshia, Progress in Materials Science, 29 (1985) 321-386.

[40] B.G. Baker, and Nutting, J. , Precipitation Processes in Steels, Iron and Steel Institute, London, 1959.

[41] T. Epicier, D. Acevedo, M. Perez, Philosophical Magazine, 88 (2007) 31-45.

[42] F.G. Berry, Davenport, A.T., and Honeycombe, R.W.K., The Isothermal Decomposition of Alloy Austenite, The mechanism of phase transformation in crystalline solid, 1968, pp. 228.

[43] A. Barbacki, R.W.K. Honeycombe, Metallography, 9 (1976) 277-291.

[44] J.V. Bee, P.R. Howell, R.W.K. Honeycombe, Metallurgical Transactions a-Physical Metallurgy and Materials Science, 10 (1979) 1207-1212.

[45] K.H. Campbell, R. W. K., Metal Science, 8 (1974) 197-203.

[46] D.V. Edmonds, Honeycom.Rw, Journal of the Iron and Steel Institute, 211 (1973) 209-216.

[47] G. Fourlaris, Effect of vanadium alloying on the precipitation reactions during pearlite formation in medium and high carbon steels, in: J.M.G.I.L.B. RodriguezIbabe (Ed.) Proceedings of the International Conference on Microalloying in Steels, 1998, pp. 427-434.

[48] D.S. Zhou, G.J. Shiflet, Metallurgical Transactions a-Physical Metallurgy and Materials Science, 22 (1991) 1349-1365.

[49] B. Izotov, The Physics of Metals and Metallography, 111 (2011) 592-597.

[50] N. Iwasa, N. Sakata, J. Takahashi, D. Raabe, Y. Takemoto, T. Senuma, Tetsu to Hagane-Journal of the Iron and Steel Institute of Japan, 98 (2012) 434-441.

[51] G. Miyamoto, Behrang, P., Furuhara, T., Interphase Boundary Precipitation of VC Accompanying Ferrite and Pearlite Transformation in Medium Carbon Steels, in: Y. Brechet, Clouet, E., Deschamps, A., Finel, A., Soisson, F. (Ed.) Solid-Solide Phase Transformations in Inorganic Materials, Trans Tech Publications, France, 2011, pp. 420.

[52] S.A. Parsons, D.V. Edmonds, Mater. Sci. Technol., 3 (1987) 894-904.

[53] D.S. Zhou, G.J. Shiflet, Metallurgical Transactions a-Physical Metallurgy and Materials Science, 23 (1992) 1259-1269.

[54] R.F. Mehl, W.C. Hagel, Progress in Metal Physics, 6 (1956) 74-&.

[55] M. Hillert, Decomposition of Austenite by Diffusional Processes, 1962, pp. 197.

[56] H. Bhadeshia, Phys. Status Solidi A-Appl. Res., 69 (1982) 745-750.

[57] W. Liu, Metallurgical and Materials Transactions A, 24 (1993) 2195-2207.

[58] C. Zener, Journal of Applied Physics, 20 (1949) 950-953.

[59] P.R. Rios, Journal of Materials Science Letters, 10 (1991) 981-983.

[60] N. Balliger, R. Honeycombe, Metallurgical and Materials Transactions A, 11 (1980) 421-429.

[61] T. Obara, G.J. Shiflet, H.I. Aaronson, Metallurgical Transactions a-Physical Metallurgy and Materials Science, 14 (1983) 1159-1167.

[62] R.W.K. Honeycombe, Metal Science, 14 (1980) 201-214.

[63] T. Gladman, The Physical Metallurgy of Microalloyed Steels, Maney, 2002.

[64] J.R. Yang, H.D.B.K. Bhadeshia, Welding Journal, 69 (1990) S305.

[65] H.-H. Kuo, M. Umemoto, K. Sugita, G. Miyamoto, T. Furuhara, ISIJ International, 52 (2012) 669-678.

[66] A.D. Batte, Honeycombe, R.W.K., Metal Science, 7 (1973) 160-168.

[67] T. Gladman, Mater. Sci. Technol., 15 (1999) 30-36.

[68] R.K. Ham, Strength of Metals and Alloys, Tokyo, Japan, 1968.

[69] A. Kelly, M.E. Fine, Acta Metallurgica, 5 (1957) 365-367.

[70] E. Orowan, Precipitation hardening, Pergamon Press, Oxford, 1968.

[71] M. Ashby, Oxide dispersion strengthening, Gordon and Breach, New York, 1958.

[72] U.F. Kocks, Acta Metallurgica, 14 (1966) 1629-&.

[73] U.F. Kocks, Argon A.S., Ashby M.F., Progress in Materials Science, 19 (1975) 289-291.

[74] G. Miyamoto, Hori, R., Poorganji, B., and Furuhara, T. , ISIJ Internatioal, 51 (2011) 1733.

[75] Kobe Steel Industrial Report

[76] Y. Funakawa, T. Shiozaki, K. Tomita, T. Yamamoto, E. Maeda, Isij International, 44 (2004) 1945-1951.

[77] A.R. Marder, B.L. Bramfitt, Metallurgical Transactions a-Physical Metallurgy and Materials Science, 7 (1976) 365-372.

[78] V.I. Izotov, V.A. Pozdnyakov, E.V. Luk'yanenko, O.Y. Usanova, G.A. Filippov, Physics of Metals and Metallography, 103 (2007) 519-529.

[79] K.K. Ray, D. Mondal, Acta Metallurgica Et Materialia, 39 (1991) 2201-2208.

[80] O.P. Modi, N. Deshmukh, D.P. Mondal, A.K. Jha, A.H. Yegneswaran, H.K. Khaira, Materials Characterization, 46 (2001) 347-352.

[81] Y.A. Bagaryastski, Dokl. Akad Nauk. S.S.S.R., 73 (1950) 1161.

[82] W. Pitsch, Acta Metallurgica, 10 (1962) 79-80.

[83] R.J. Dippenaar, R.W.K. Honeycombe, Proceedings of the Royal Society of London. Series A, Mathematical and Physical Sciences, 333 (1973) 455-467.

[84] Y. Ohmori, Isij International, 41 (2001) 554-565.

[85] J.W. Cahn, Acta Metallurgica, 8 (1960) 554-562.

[86] N.C. Law, S.A. Parsons, P.R. Howell, D.V. Edmonds, Mater. Sci. Technol., 3 (1987) 642-648.

[87] H. Kitahara, R. Ueji, N. Tsuji, Y. Minamino, Acta Materialia, 54 (2006) 1279-1288.

[88] H. Kitahara, R. Ueji, M. Ueda, N. Tsuji, Y. Minamino, Materials Characterization, 54 (2005) 378-386.

[89] T. Furuhara, T. Shinyoshi, G. Miyamoto, J. Yamaguchi, N. Sugita, N. Kimura, N. Takemura, T. Maki, ISIJ International, 43 (2003) 2028-2037.

[90] G. Miyamoto, T. Shinyoshi, J. Yamaguchi, T. Furuhara, T. Maki, R. Uemori, Scripta Materialia, 48 (2003) 371-377.

[91] R. Okamoto, A. Borgenstam, J. Agren, Acta Materialia, 58 (2010) 4783-4790.

[92] P.R. Wilyman, R.W.K. Honeycombe, Metal Science, 16 (1982) 295-303.

[93] J.L. H. Aaronson, Lectures of the theory of phase transformations, TMS, Penssylvania, 1999.

[94] M. Gouné, J. Drillet, P. Maugis, Computational Materials Science, 55 (2012) 127-135.

[95] E. Gamsjäger, M. Militzer, F. Fazeli, J. Svoboda, F.D. Fischer, Computational Materials Science, 37 (2006) 94-100.

[96] F. Perrard, A. Deschamps, P. Maugis, Acta Materialia, 55 (2007) 1255-1266.

[97] S.W. Thompson, G. Krauss, Metallurgical Transactions a-Physical Metallurgy and Materials Science, 20 (1989) 2279-2288.

[98] K. Iakoubovskii, K. Mitsuishi, Y. Nakayama, K. Furuya, Microscopy Research and Technique, 71 (2008) 626-631.

[99] T. Malis, S.C. Cheng, R.F. Egerton, Journal of Electron Microscopy Technique, 8 (1988) 193-200.

[100] T. Murakami, H. Hatano, G. Miyamoto, T. Furuhara, ISIJ International, 52 (2012) 616-625.

[101] M.-Y. Chen, H.-W. Yen, J.-R. Yang, Scripta Materialia, 68 (2013) 829-832.

[102] A.C. Fischer-Cripps, Introduction to Contact Mechanics, Springer New York, 2011, pp. 77-104.

[103] S. Berbenni, V. Favier, X. Lemoine, M. Berveiller, Materials Science and Engineering: A, 372 (2004) 128-136.

[104] J.L. Bucaille, S. Stauss, E. Felder, J. Michler, Acta Materialia, 51 (2003) 1663-1678.

[105] R.M. Douthwaite, N.J. Petch, Acta Metallurgica, 18 (1970) 211-216.

[106] E.J. Pavlina, C.J. Van Tyne, Journal of Materials Engineering and Performance, 17 (2008) 888-893.

[107] Y.-T. Cheng, C.-M. Cheng, Surface and Coatings Technology, 133–134 (2000) 417-424.

[108] M. Dao, N. Chollacoop, K.J. Van Vliet, T.A. Venkatesh, S. Suresh, Acta Materialia, 49 (2001) 3899-3918.

[109] M.F. Doerner, W.D. Nix, J. Mater. Res., 1 (1986) 601-609.

[110] W.C. Oliver, G.M. Pharr, J. Mater. Res., 19 (2004) 3-20.

[111] Y. Choi, W. Yong Choo, D. Kwon, Scripta Materialia, 45 (2001) 1401-1406.

[112] Q. Furnémont, M. Kempf, P.J. Jacques, M. Göken, F. Delannay, Materials Science and Engineering: A, 328 (2002) 26-32.

[113] X.F. Wang, X.P. Yang, Z.D. Guo, Y.C. Zhou, H.W. Song, Nanoindentation Characterization of Mechanical Properties of Ferrite and Austenite in Duplex Stainless Steel, in: Y.W. Chang, N.J. Kim, C.S. Lee (Eds.) Advanced Materials and Processing, Trans Tech Publications Ltd, Stafa-Zurich, 2007, pp. 1165-+.

[114] S. Allain, O. Bouaziz, Materials Science and Engineering: A, 496 (2008) 329-336.

Titre: Etude de la Précipitation interphase dans le systèm Fe-V-C : La Microstructure et La Modélisation

Abstract

The present thesis gives an overview of carbide aggregates (interphase precipitation and carbide fiber) in vanadium-alloyed steels, covering the aspects of microstructure, modeling, and mechanical properties. The microstructural features of different carbide aggregates by the use of microscopies, and the transition of carbide morphologies is discussed. A new model considering the ledge mechanism as well as austenite decomposition is subsequently proposed according to the observed microstructure. The sheet spacing, particle spacing, and interface velocity, can be calculated and show good agreements with experimental data. Finally, the effect of interphase-precipitated carbide distribution (sheet spacing, particle spacing, and carbide radius) on Orowan strengthening contribution is examined by nano-indentation. By the virtue of small indenter, the mechanical properties of single ferrite grain are able to be extracted.

Keyword: *carbide, ferrite, interphase precipitation, transformation, mechanical properties, nano-indentation.*

Résumé

Le travail présenté dans cette thèse est consacré à la précipitation interphase dans les aciers microalliés au vanadium. Il s'agit principalement de mieux comprendre l'évolution des microstructures et des propriétés mécaniques résultantes à partir d'une double approche expérimentale et de modélisation. Les analyses effectuées conjointement en Microscopie Electronique en Transmission et en nanoindentation ont permis de mieux cerner les relations qui existent entre les paramètres microstructuraux de la précipitation interphase (taille moyenne des carbures, distances moyenne entre carbures et entre feuillets, morphologie des carbures) et les modifications de propriétés mécaniques locales induites dans les aciers à très haute résistance. Par ailleurs, nous avons développé un modèle original qui couple les cinétiques de transformation de phases à celle de la précipitation interphase. Ce modèle permet de décrire l'évolution des paramètres microstructuraux et les résultats obtenus sont en très bon accord avec les résultats expérimentaux.

Mot-clés: *Carbures, ferrite, précipitation interphase, transformation de phases, propriétés mécaniques, nano-indentation*